UNIVERSIDAD MICHOACANA DE SAN NICOLÁS DE HIDALGO

INSTITUTO DE INVESTIGACIÓN EN METALURGIA Y MATERIALES

PROGRAMA DE DOCTORADO EN
CIENCIAS EN METALURGIA Y CIENCIAS DE LOS MATERIALES

DOCTORATE DEGREE PROGRAM IN
SCIENCES IN METALLURGY AND MATERIALS SCIENCES

MECHANICAL AND NONDESTRUCTIVE CHARACTERIZATION OF LOW TEMPERATURE EMBRITTLEMENT EFFECTS OF A 2507 SUPER DUPLEX STAINLESS STEEL

Tesis que para obtener el Grado de
Doctor en Ciencias en Metalurgia y Ciencias de los Materiales

Thesis submitted to obtain the degree of
Doctor in Sciences in Metallurgy and Materials Sciences

by:

M.C. GILDARDO GUTIÉRREZ VARGAS

Director de Tesis
Committee Chair

DR. ALBERTO RUIZ MARINES

Co-director de Tesis
Committee co-chair

DR. JIN-YEON KIM
Georgia Institute of Technology

Morelia, Michoacán; Febrero de 2019.

AGRADECIMIENTOS

Al Instituto de Investigaciones Metalúrgicas, por acogerme y permitirme forjarme en sus aulas y trabajar en tan prestigiada institución, donde pase maravillosos momentos adquiriendo el conocimiento necesario de sus profesores, heredándome con esto la gran riqueza del saber.

Este trabajo se realizó en la Universidad Michoacana de San Nicolás de Hidalgo con fondos de SENER-CONACYT México bajo el proyecto: CEMIE-Geo-P18. Este autor desea agradecer a la UMSNH y CONACYT-MÉXICO por su apoyo para la realización de mis estudios de doctorado y la estancia de investigación en el Instituto Tecnológico de Georgia.

Agradezco a Dios, por el don tan preciado de la vida, por cada día que me permite vivir, disfrutando de su admirable creación, inspirándome a amar, trabajar, soñar, conocer nuevos amigos y cultivarme para ser cada día mejor, así como tener la dicha de terminar este proyecto.

A mis padres Gregoria Vargas Avalos y J. Concepción Gutiérrez Sánchez, por su amor, ejemplo, esfuerzo, apoyo, buenos consejos e alientos, así como a mis hermanas y hermanos con quienes siempre conté en todo momento y son muy importantes en el desarrollo de mis metas.

A mis amigos, el Ing. Ricardo Martin Álvarez, Ing. Kevin Fuentes Corona, Ing. Vania Marisol Rodríguez Herrejón, Ing. Francisco Solorio González, Ing. María Remedios Cisneros Magaña, M.C. Fernando Vargas, M.C. José Antonio Rodríguez Torres, M.C. Víctor Sayil López Álvarez, M.C. Heriberto Granados, M.C. Lourdes Yareth Chávez Herrera, M.C. Saúl L. Hernández Trujillo, Dr. Víctor Hugo López Morelos y a Jorge Vázquez García por sus comentarios y sugerencias dadas, pero sobre todo por su amistad que me alentó para la culminación de este proyecto.

Al Dr. Alberto Ruiz Marines y al Dr. Jin-Yeon Kim por haberme permitido realizar mi trabajo de tesis bajo su dirección y brindarme su apoyo, confianza, amistad, conocimientos y asesorarme para llevar a cabo esta investigación.

Al Dr. Laurence J. Jacobs y al Instituto Tecnológico de Georgia, por recibirme con los brazos abiertos para realizar una parte experimental de mí proyecto en Georgia, por su apoyo, compresión y permitirme el uso del equipo de ultrasonido no lineal, durante mi estancia en el instituto tecnológico de Georgia.

Al Dr. Jorge González Sánchez del Centro de Investigación en Corrosión de la Universidad Autónoma de Campeche por el apoyo en la realización de las pruebas de corrosión.

CONTENTS

LIST OF TABLES i
LIST OF FIGURES ii
ABBREVIATIONS AND SYMBOLS v
RESUMEN viii
ABSTRACT ix
CHAPTER I. INTRODUCTION 1
JUSTIFICATION 3
OBJECTIVES 4
HYPOTHESIS 5
CHAPTER II. LITERATURE REVIEW 6
2.1. The stainless steels. 6
2.2. Classification of stainless steels. 7
2.2.1. Ferritic stainless steels. 9
2.2.2. Austenitic stainless steels. 10
2.2.3. Duplex stainless steels. 12
2.3. Chemical composition. 15
2.3.1. Influence of alloying elements. 16
2.3.1.1. Chromium (Cr). 16
2.3.1.2. Nickel (Ni). 18
2.3.1.3. Molybdenum (Mo). 19
2.3.1.4. Nitrogen (N). 19
2.3.1.5. Manganese (Mn). 20
2.3.1.6. Copper (Cu). 20
2.3.1.7. Carbon (C). 21
2.3.1.8. Tungsten (W). 22
2.3.1.9. Silicon (Si). 23
2.3.1.10. Other elements. 24
2.3.2. Microstructure of duplex stainless steels. 26
2.3.2.1. Ferrite promoting versus austenite promoting elements. 27
2.3.2.2. Effects of alloying elements on phase balance. 27
2.3.3. Metallurgy of duplex stainless steels. 28
2.3.3.1. Austenite-Ferrite phase balance. 29
2.3.3.2. Precipitation reactions. 31
2.3.4. Heat treatment of duplex stainless steels. 31
2.3.4.1. Temperatures above 1050 °C. 32
2.3.4.2. The 600-1050 °C nose. 33
2.3.4.3. The 300-600 °C nose. 34
2.3.5. Intermetallic precipitates and secondary phases. 35
2.3.5.1. Sigma phase (σ). 35
2.3.5.2. Chi phase (χ). 35
2.3.5.3. Secondary austenite (γ_2). 36
2.3.5.4. Laves phase. 36

2.3.5.5. Carbides. 36
2.3.5.6. Nitrides. 37
2.3.5.7. Cu-rich epsilon phase (ε). 37
2.3.5.8. Alpha prime (α′). 37
2.3.5.9. G phase. 38
2.3.6. Physical properties. 39
2.3.7. Mechanical properties. 39
2.3.7.1. Tensile characteristics. 40
2.3.7.2. Hardness. 41
2.3.7.3. Impact strength. 41
2.3.7.4. Fatigue. 42
2.3.8. Corrosion resistance. 44
2.3.8.1. General corrosion. 44
2.3.8.2. Sulfuric acid. 45
2.3.8.3. Hydrochloric acid. 45
2.3.8.4. Nitric acid. 46
2.3.8.5. Sodium hydroxide. 47
2.3.8.6. Phosphoric acid. 47
2.3.8.7. Organic acids. 48
2.3.9. Localized corrosion. 49
2.3.9.1. Pitting corrosion. 50
2.3.9.2. Crevice corrosion. 52
2.3.9.3. Stress corrosion cracking. 52
2.4. The 475 °C embrittlement. 53
2.5. Ultrasonic properties 59
2.5.1. Longitudinal and shear wave velocity. 59
2.5.2. Nonlinear ultrasound. 59
2.5.2.1. Nonlinear Rayleigh waves: nonlinearity parameter. 60
2.5.2.2 Acoustoelasticity. 61
2.5.3. Ultrasonic attenuation. 63
2.6. Electric conductivity measurements using alternating current potential drop (ACPD). 65
2.7. Thermoelectric conductivity measurements. 66
CHAPTER III. EXPERIMENTAL METHODOLOGY 67
3.1. Sample preparation. 67
3.2. Electric conductivity measurements on thermally embrittled 2507 SDSS. 67
3.3. Longitudinal and shear wave ultrasonic velocity measurements. 69
3.4. Ultrasonic attenuation measurements. 70
3.4.1 Ultrasonic C-scan imaging. 72
3.5. Nonlinear ultrasonic measurements. 73
3.5.1 Rayleigh wave measurement. 74
3.6. Thermoelectric measurements on thermally embrittled 2507 SDSS. 78
3.7. Microstructural characterization. 79
3.8. Mechanical characterization. 79

3.8.1 Charpy impact test. 80
3.8.2 Tension test. 80
3.8.3 Hardness measurements. 80
3.9. KJMA model applied to embrittled 2507 SDSS. 81
CHAPTER IV. RESULTS AND DISCUSSION 82
4.1. Microstructural characterization. 82
4.2. Effect of aging time on longitudinal and shear wave velocity. 84
4.3. Effect of aging time on Vickers microhardness. 86
4.4. Effect of aging time on impact energy. 87
4.5. Detection of localized conductivity using electric conductivity measurements. 89
4.5.1. Experimental results. 89
4.5.2. Determination of the resistance to localized corrosion. 90
4.5.3. Relation between microhardness CPT and electric conductivity. 95
4.6. Effect of aging time on ultrasonic attenuation. 96
4.6.1. Changes in signal amplitude. 96
4.7. Effect of embrittlement on hardness. 102
4.8. Effect of aging time on nonlinear ultrasonic parameter. 103
4.9. Effect of aging time on thermoelectric power. 106
4.10. Effect of aging on tensile properties. 107
4.11. Use of the KJMA model to fit experimental results. 109
4.12. Comparisons of NDE results. 110
CHAPTER V. CONCLUSIONS 112
5.1. Electric conductivity and corrosion susceptibility. 112
5.2. Application of nonlinear ultrasonic measurements. 112
5.3. Application of attenuation measurements. 113
5.4. Application of thermoelectric power and KJMA model. 113
5.5 Comments on NDE methods. 114
Recommendations and future work 115
References 116

LIST OF TABLES

Table 2.1. Classification of stainless steels by microstructure 8
Table 2.2. Chemical composition in wt. % of wrought duplex stainless steel grades 14
Table 2.3. Effects of different alloying additions and microstructure on the pitting and crevice resistance of DSSs 26
Table 2.4. Phases observed in duplex stainless steels.. 38
Table 2.5. Physical properties of 2507 super duplex stainless steel..... 39
Table 2.6. Minimum room temperature tensile properties and maximum hardness of wrought solution annealed stainless steels..... 40
Table 2.7. Influence of different alloying additions and microstructure on the pitting and crevice corrosion resistance of DSSs.. 50
Table 3.1. Chemical composition of 2507 SDSS in wt. %..... 67
Table 4.1. Fitting parameters from KJMA model for ultimate strength of aged samples at 748K... 109

LIST OF FIGURES

Figure 2.1. Protective oxide film in stainless steel and rust formation in steels 7
Figure 2.2. Cr and Ni composition for the different stainless steels. 8
Figure 2.3. Microstructure of a ferritic stainless steel (type 430) annealed strip. 10
Figure 2.4. Austenite microstructure showing equiaxed grains and characteristic annealing twins. Normal presence of small inclusions can be observed. 11
Figure 2.5. Wrought 2205 duplex microstructure, islands of austenite in a continuous matrix of ferrite 12
Figure 2.6. Corrosion rate profile with respect to Cr contents in intermittent water spray at room temperature 17
Figure 2.7. Effect of Nickel addition to stainless steels 18
Figure 2.8. Schematic summary of the effects of alloying elements on the anodic polarization curve 22
Figure 2.9. Schematic summary of the effects of alloying elements on the formation of various precipitates 23
Figure 2.10. Schaeffler diagram of 1949 28
Figure 2.11.Elevated temperature region of a pseudobinary phase diagram for duplex stainless steel compositions. Shaded region represents the range for commercial alloys 30
Figure 2.12. TTT diagrams of duplex stainless steels derived by optical metallography between 600 and 1050°C and hardness measurements between 300 and 600°C 33
Figure 2.13. TTT diagram of UNS S32750 (SAF 2507), showing the precipitation kinetics of intermetallic precipitates and secondary phases 34
Figure 2.14. Normalized Charpy energy versus temperature measured for several stainless steels 41
Figure 2.15. Time-temperature-transformation (TTT) diagram for SAF 2507 SDSS. The curve corresponds to 27J impact toughness indicating the rate of embrittlement at different temperature regions 42
Figure 2.16. Influence of pitting resistance equivalent number (PREN) to fatigue strength in NaCl solution versus in air 43
Figure 2.17. Sulphuric acid: 0.1 mm/yr isocorrosion curves: aerated: S32304, S31803, S32750, S31254, N08940 and carbon steel 45
Figure 2.18. Hydrochloric acid: stagnant: 0.1 mm/yr isocorrosion curves 46
Figure 2.19. Nitric acid: 0.1 mm/year isocorrosion curves 46
Figure 2.20. White liquors plus chlorides 47
Figure 2.21. Wet phosphoric acid (WPA): minimum temperature for a corrosion rate of 0.127 mm/year 48
Figure 2.22. Formic acid: 0.1 mm/yr. isocorrosion curves 49
Figure 2.23. Acetic (50%) plus formic acids (and water): boiling 49
Figure 2.24. CPTs in various NaCl concentration at +300 mV SCE, neutral pH 51
Figure 2.25. CPTs and CCTs in 6% ferric chloride solution, 24 hours 52
Figure 2.26. Stress corrosion cracking of practical experience and laboratory test data in neutral aerated (~8 ppm) aqueous NaCl environments. Testing time 1000 hours Load ≥ Rp at test temperature . 53
Figure 2.27. Phase diagram of the iron–chromium binary system 54
Figure 2.28. Needle like precipitates observed in the ferritic phase of DIN W Nr. 1.4462 grade DSS after aging treatment at 475 °C for 100 h 55
Figure 2.29. Modulated contrast observed in the ferritic phase of 2205 DSS aged at 475 °C for 2 h 56

Figure 2.30. Hardness of the Fe–45% Cr–5% Ni, Fe–45% Cr alloys and the ferrite phase in two CF3 stainless steels as a function of aging time at 400 °C 57
Figure 2.31.Variation of impact energy with time of aging at 475°C for the DINWNr.1.4462 grade DSS 58
Figure 3.1 (a) A picture of the deployable ACPD probe and (b) schematic diagram of ACPD measurements in the x direction. 68
Figure 3.2 Schematic representation of pulse-echo method to measure the shear wave velocity measurements.. 70
Figure 3.3. (a) Schematic representation of pulse-echo method for attenuation coefficient measurements, (b) Corresponding time domain RF signal, (c) Frequency domain signals and (d) total loss as function of frequency. 71
Figure 3.4. Experimental arrangement for c-scan imaging. 73
Figure 3.5. Experimental setup for nonlinear surface wave measurements. 74
Figure 3.6. (a) A typical time-domain signal and (b) its frequency spectrum that shows both fundamental and second harmonic amplitude. 75
Figure 3.7. Amplitudes of A1 (a), A2 (b), and A2/ (A1)2, (c) as a function of propagation distance. 76
Figure 3.8. (a) Experimental setup for acoustoelastic velocity measurement and (b) transducer-sample configuration for velocity measurements under cyclic loading. 77
Figure 3.9. Schematic diagram of the thermoelectric measurements using a two-tipped probe. 78
Figure 4.1. Microstructure of 2507 SDSS in a) the as-received condition and aged for: b) 10 min, c) 50 h and d) 100 h (Note that these diamonds are indentation marks from the microhardness test). 82
Figure 4.2. High magnification SEM micrograph of precipitated G-particles after aging for 300 h. 83
Figure 4.3. Transmission electron microscopy bright-field images showing: (a-b) complex dislocation tangle in the untreated specimen and specimen aged at 475 °C for 50 h and (c) aged for 300 h showing a mottled contrast in ferrite associated with spinodal decomposition. 84
Figure 4.4. Shear wave velocity measurements as function of aging time.. 85
Figure 4.5. Shear wave birefringence as function of holding time.. 85
Figure 4.6. Vickers microhardness maps of 475°C embrittled 2507 SDSS. (a) as-received condition and aged for (b) 50 h, (c)100 h and (d) 300 h. 86
Figure 4.7. Effect of holding time on Vickers microhardness of ferrite and austenite at 475°C. 87
Figure 4.8. Effect of holding time on impact properties of 2507 SDSS aged at 475 °C 87
Figure 4.9. Fracture surfaces of impact specimens for (a) as-received; and aged for (b) 10 h, (c) 100 h and (d) 300 h. 88
Figure 4.10. Electric conductivity as a function of the aging time for thermally embrittled 2507 SDSS at 475°C. 90
Figure 4.11. DL-EPR curves of 2507 SDSS untreated and isothermally aged at 475 °C (a) up to 50 h and (b) aged for 100 h and 300 h respectively. 91
Figure 4.12. Q_r /Q_a as function of holding time 92
Figure 4.13.SEM micrographs showing the surface characteristics 2507 SDSS after DL-EPR tests aged at 475 °C for: (a) 10h (b) 50 h, (c) 100 h and (d) 300 h respectively. 93
Figure 4.14.Typical curves of current density as function of temperature for 2507 SDSS after CPT test for as-received condition (AR) and aged for 1, 10, 50, 100 and 300 h respectively. 94
Figure 4.15. CPT values as a function of aging time. 95
Figure 4.16. Comparison of electric conductivity, microhardness of ferrite phase and CPT results. 96
Figure 4.17.Attenuation coefficient as function of ultrasonic frequency on 2507 SDSS for untreated condition (BM) and aged for 50, 100, 300, 500 and 1000 h. 97

Figure 4.18.Longitudinal attenuation coefficient as function of aging time for 2507 SDSS aged at 475 °C. 98
Figure 4.19.Optical micrographs at 1,000x of the 2507 SDSS microstructure in the rolling direction: (a) in the untreated condition and after aging for (b) 300h and (b) 500h. 99
Figure 4.20.Attenuation coefficient c-scans images on 2507 SDSS obtained at 5 MHz (left) and 20 MHz (right) for: (a and b) untreated condition and specimens aged for: 50 h (c and d), 100 h (e and f), 500 h (g and h) and 1000 h (i and j). 101
Figure 4.21.Hardness measurements as function of thermal exposure time. (a) Rockwell C hardness (b) Vickers microhardness. 102
Figure 4.22.Relative shear wave and longitudinal wave velocity as a function of uniaxial stress. 104
Figure 4.23.Normalized nonlinear parameters as function of thermal exposure time (a) from Rayleigh waves (β_R), (b) from acoustoelasticity (β_σ). 105
Figure 4.24. Changes of linear and nonlinear ultrasonic parameters and micro hardness as function of thermal exposure time. 106
Figure 4.25. Change on the TEP of 2507 SDSS as function of holding time. 107
Figure 4.26. UTS and yield strength as function of holding time for aged 2507 SDSS. 108
Figure 4.27. Percentage of area reduction as function of holding time for aged 2507 SDSS 108
Figure 4.28.Microhardness predicted from KJMA model fitted to the mean value of measured microhardness for alloy 2507 SDSS. 109
Figure 4.29.Ultimate strength predicted from KJMA model fitted to the mean value of measured ultimate strength for alloy 2507 SDSS. 110

ABBREVIATIONS AND SYMBOLS

Abbreviations

SDSS	Super duplex stainless steel
NDE	Nondestructive evaluation
TEP	Thermoelectric Power
ACPD	Alternating current potential drop
HRC	Hardness Rockwell C
HV	Microhardness Vickers
DL-EPR	Double loop electrochemical potentiokinetic reactivation
DOS	Degree of sensitization
OM	Optical microscopy
SEM	Scanning electron microscopy
TEM	Transmission electron microscopy
DSS	Duplex stainless steel
PRE	Pitting resistance equivalent
FSS	Ferritic stainless steel
BCC	Body center cubic
SCC	Stress-corrosion cracking
ASS	Austenitic stainless steel
AISI	American Iron & Steel Institute
PREN	Pitting Resistance Equivalence Number
FCC	Face center cubic
HAZ	Heat affected zone
DBTT	Ductile-to-brittle fracture transition temperature
CPT	Critical pitting temperature
MSS	Martensitic stainless steel
P-H	Precipitation-hardened
TTT	Time-temperature transformation (diagram)
ASTM	American Society for Testing and Materials
WPA	Wet phosphoric acid
SCE	Saturated calomel electrode
CCT	Critical crevice temperature
TOEC	Third-order elastic constants
FFT	Fast Fourier transform
J	Joule
AR	As-received condition
BM	Base metal
UTS	ultimate tensile strength
YS	yield stress
yr.	Year

Symbols

α	Ferrite phase
γ	Austenite phase
α'	Alpha prime phase
β_R	Nonlinear parameter
σ	Sigma phase
χ	Chi phase
ε	Epsilon phase
γ_2	Secondary austenite
δ	Ferrite phase
$R_{P0.2}$	Yield strength
Rm	Ultimate tensile
x_1	Propagation distance
u_1 and u_2	Out-of-plane displacement amplitudes fundamental and second-order harmonics
c_l, c_s, c_R	Longitudinal, shear and Rayleigh wave velocities
ω	Fundamental angular frequency
A_1, A_2	Amplitudes of the fundamental and second harmonic
c_0	Wave velocity without a remote stress
σ_{rem}	Remote stress
K_i	The i^{th} order acoustoelastic coefficient
U	Strain energy density
c_{ijkl}, c_{ijklmn}	Second and third order elastic constants
ε_{ij}	Lagrangian strain
l, m, and n	Murnaghan coefficients
λ and μ	Lamé constants
$K_{d,n}$	Acoustoelastic constants of the longitudinal wave (d) propagating normal (n) to the applied stress
$K_{s,np}$ and $K_{s,nn}$	Acoustoelastic constants for a shear wave propagating normal to the applied stress with polarization parallel (p) and normal (n) to the applied stress
β_σ	Material nonlinearity parameter
L_T and L_S	Total measured loss and Scattering induced loss
L_D and L_A	beam diffraction losses and absorption losses
a	Transducer radius
z	Propagation distance, and are
J_0 and J_1	First kind Bessel functions of order 0 and 1
λ	Wavelength
D	Grain size diameter
f	Frequency
α_R	Attenuation coefficient
μ	Magnetic permeability
σ	Electric conductivity of the material
f	Frequency of the injected current

R_1	Measured resistance
V_1	Voltage
I_1	Injecting current
ρ	Electric resistivity
f	Inspection frequency
a	Electrode separation ACPD sensor
z and d	Distance
$S(\omega)$	Frequency spectrum of the source signal
$R_{ws}(\omega)$, $R_{sw}(\omega)$	Reflection coefficients of water-steel and steel-water interfaces
$T_{ws}(\omega)$, $T_{sw}(\omega)$	Transmission coefficients of water-steel and steel-water interfaces
k_s, α_w, α_s	Wavenumber and attenuation coefficient of water, and wavenumber and attenuation coefficient of the steel specimen,
$D_1(\omega)$, $D_2(\omega)$	Diffraction corrections for the propagation paths for the first and second echoes
E_1, E_2	Peak-to-peak voltages front wall and first back wall
T_h	Heat temperature
T_c	Cold temperature
ΔT	Temperature difference
ΔV	Voltage
S_S and S_R	Absolute TEP of the specimen and the reference electrode
S_{SR}	Relative TEP of the sample with respect to the reference electrode
H	A progressively changing material property as function of holding time and aging temperature
t	Holding time
T	Aging temperature
n	Avrami exponent
k	A kinetic coefficient
k_0	pre-exponential factor
Q	Effective activation energy for the phase transformation
Q_r	Reactivation energy
Q_a	Activation energy
R	Universal gas constant (8.314 J-mol-1K-1).
H_{max}	Maximum measured microhardness
H_0	Measured microhardness value of the unaged material
Δ	Normalized shear wave birefringence
c_{sp} and c_{sn}	Shear wave velocities with polarizations parallel and normal

RESUMEN

El acero inoxidable súper dúplex (SDSS) 2507 tienen una excelente combinación de propiedades mecánicas, físicas y de resistencia a la corrosión, estas propiedades son el producto de su composición química y su microestructura que consiste en cantidades aproximadamente iguales de ferrita (α) y austenita (γ). Sin embargo, el deterioro de estas propiedades excelentes de la tenacidad a la fractura y la resistencia a la corrosión cambia como resultado de la exposición a temperaturas en el rango de 280 a 516 °C que es un problema de estos aceros, ya que ellos fragilizan y limitan sus aplicaciones a las temperaturas de por debajo de 280 °C. Para evaluar la pérdida en estas propiedades de tenacidad y susceptibilidad a la corrosión del SDSS 2507 fragilizado térmicamente por medio de ensayos no destructivos y los métodos destructivos.

El SDSS 2507 fue envejecido por diferentes períodos de tiempo hasta de 500 h y 1000h a la temperatura de 475 °C y después sujetas a la Evaluación No Destructivos (NDE) de Ultrasonido midiendo la velocidad de onda longitudinal, transversal y la atenuación de las ondas ultrasónicas, la medición del Potencial Termoeléctrico (TEP), la medición del contenido de ferrita, la medición de caída de potencial de corriente alterna (ACPD), la medición de Ultrasonido no lineal y la medición acustoelastica. Y los ensayos destructivos como son las prueba de dureza Rockwell C (HRC), las mediciones de microdureza Vickers (HV), los ensayos de tensión, la prueba de impacto charpy para determinar la perdida de la tenacidad y la prueba de corrosión por reactivación potencio-cinética electroquímica de doble ciclo (DL-EPR) y el grado de sensitización (DOS) inducido en el SDSS 2507 fragilizado térmicamente, así como, el uso de la microscopia óptica (OM), la Microscopia Electrónica de Barrido (SEM) y la Microscopia Electrónica de Transmisión (TEM).

Los resultados experimentales muestran cambios en las propiedades mecánicas del SDSS 2507 debido a la aplicación del tratamiento térmico de envejecido a baja temperatura de 475 °C que causa la descomposición espinoidal y/o precipitación de la fase alfa prima, con lo que fragiliza el acero y reduce la resistencia a la corrosión del mismo limitando su aplicación a temperaturas inferiores a los 280 °C y esto fue detectado por algunos ensayos no destructivos, las evidencias de microscopia y corroborado por los métodos destructivos.

Palabras clave: Acero inoxidable súper dúplex, Fragilización 475 °C, Evaluación no destructiva, Ultrasonido no lineal, Potencial termoeléctrico, Caracterización de materiales.

ABSTRACT

The super duplex stainless steels (SDSSs) have an excellent combination of mechanical properties and corrosion resistance these properties are the product of their microstructure consisting of approximately equal amounts of ferrite (α) and austenite (γ). However, the deterioration in the fracture toughness and corrosion resistance resulting from exposures to a temperatures between 280 and 516 °C, is known to be a critical issue in these steels, since they suffer embrittlement, which would significantly limits their applications to temperatures below 280 °C. This research intends to evaluate the loss in these properties of tenacity and the susceptibility to the corrosion of the 2507 SDSS due to thermal embrittlement by means of non-destructive evaluation (NDE) and destructive methods.

The 2507 SDSS specimens are aged at 475 °C for different holding times between 500 and 1000h and then subjected to a series of NDE measurements of the ultrasonic velocity and attenuation, thermoelectric power (TEP), ferrite content, alternating current potential drop (ACPD), the Rayleigh wave ultrasonic nonlinearity, and the acoustoelastic effect. Furthermore, numerous destructive methods are performed, including Hardness Rockwell C (HRC), Vickers microhardness (HV), tension, Charpy impact energy tests for the loss of toughness, and corrosion tests, the double loop electrochemical potentiokinetic reactivation (DL-EPR) and the degree of sensitization (DOS). In addition, the optical microscopy (OM), scanning electron microscopy (SEM) and transmission electron microscopy (TEM) are used for the microstructure characterizations.

The experimental results show that changes in the mechanical properties of the 2507 SDSS are due to the spinodal decomposition and/or precipitation of the alpha prime phase which are induced by the application of the thermal aging at the temperature 475 °C and these effects results in the embrittlement of the steel and reduction of the resistance to the corrosion. These effects limit the material´s applications to temperatures below 280 °C. The changes in microstructure are detected by the NDE methods which are supported by the microscopy evidences and the results from the destructive tests.

Finally sensitivities of these different NDE methods are compared and advantages and disadvantages of them including their field applicability are discussed.

CHAPTER I. INTRODUCTION

The duplex stainless steels (DSSs) or austenitic-ferritic stainless steels have commercially available for 80 years. The most of the DSSs exhibit good corrosion resistance and mechanical properties superior to those of austenitic stainless steels: they are stronger (without sacrificing ductility), resist corrosion better, and cost less due to their relatively low nickel content. The DSSs have various applications as structural materials in critical components of nuclear power plants, chemical and petrochemical industries, and oil and gas sectors because of an attractive combination of mechanic properties and corrosion resistance resulting from their duplex microstructure in the two basic phases. The austenite (γ) and the other ferrite (α) are, present in about equal amount (but not less than 30% each). The 2507 SDSS, containing about 25%Cr, 6-7%Ni, 3-4%Mo, 0.2-0.3% N, 0-2%Cu y 0-2%W, have high corrosion resistance expressed in terms of the pitting resistance equivalent: PRE = (%Cr + 3.3Mo +16%N) > 40%, which corresponds to a critical pitting temperature of higher than 60°C [1].

The degradation of these excellent properties in the fracture toughness and corrosion resistance as a result of exposures at a temperature between 280 °C and 500 °C is a common problem of the DSSs and ferritic stainless steels as they are susceptible to the embrittlement phenomenon [2]. This phenomenon is termed 475 °C embrittlement because the rate of embrittlement is highest at 475 °C [3, 4] and is characterized by the reaction undergone by the ferrite phase: $\alpha \rightarrow \alpha' + \alpha$ in this temperature range [5], which is essentially produced by a miscibility gap in iron-chromium binary alloy system [6]. The decomposition of the ferritic phase to chromium-rich phase α' and iron-rich phase α brittles the microstructure.

According to Cahn [7] and Hillard [8], the phenomenon is characterized by: (a) spinodal decomposition ($\alpha \rightarrow \alpha' + \alpha$) and (b) nucleation and growth of α'. The term spinodal decomposition refers to a reaction that promotes the formation of two phases that have the same crystal lattice type, but different chemical compositions and physical properties. The spinodal decomposition produces the hardening of the ferrite phase and a loss of the tenacity of the material [9].

Inevitably, the property changes in DSSs exposed in the temperature range of 280-500°C adversely affect their performance, degrading the corrosion resistance, and embrittlement the steel by decreasing its tenacity.

In this investigation, the loss of the tenacity and corrosion resistance are evaluated with the NDE measurements, which are direct, fast, and sensitive as well as reliable to detect microstructural changes of the 2507 SDSS, such as the spinodal decomposition and/or nucleation and growth of α′. The non-linear and conventional linear ultrasound, thermoelectric power (TEP), alternating current potential drop (ACPD), and ferrite content measurement are performed. As complementary measurements, mechanical characterizations by Hardness Rockwell C (HRC), Vickers microhardness (HV), tension, Charpy impact energy, and corrosion tests are carried out in 2507 SDSS with annealed thermal treatment to 475°C and different holding times up to 1000h. Besides, the optical microscopy (OM), scanning electron microscopy (SEM) and transmission electron microscopy (TEM) are used. The results from these measurements show that the NDE methods are practical and economical way to detect the 475 °C embrittlement in these steels.

JUSTIFICATION

The Duplex Stainless Steels are materials frequently employed thanks to the combination of properties generated by their two phase's austenite and ferrite: the austenite provide high mechanical resistance and the ferrite provide an excellent corrosion resistance, making them very attractive materials in industries where functionality is required in aggressive media as well as good mechanical properties are required. However, their applications are limited to temperatures below 280 °C as they suffer embrittlement when exposed to temperatures of 280 °C by a long period of time or to higher temperatures of up to 516 °C at smaller holding time, which causes changes in the mechanical properties and corrosion resistance of these steels by the effect of the thermal treatment called 475 °C embrittlement, that brittles the steel at ambient temperature.

Although, the microstructural evolution and mechanical property degradation at low temperature has been studied by several investigators, there is no study on nondestructive methods that can accurately indicate the degree of deterioration or to what extent the steel meets the requirements for its application. Investigations of behavior, degradation and damage formation in structures and components can reduce maintenance costs and provides security. Hence, it is of tremendous importance to study and, understand the effect of temperature on the mechanical properties and to evaluate these effects using a nondestructive technique to be able to predict the degree of thermal damage in a component.

OBJECTIVES

The objectives intended to achieve are as follows:

General Objective

Study the effect of embrittlement of a 2507 super duplex stainless steel (SDSS) at low temperature, with different exposure times to aging treatment at 475 °C, on the mechanical properties and linear ultrasonic properties such as the velocity and attenuation, and the nonlinear ultrasonic parameter β.

Specific objectives:

- Characterize microstructurally, mechanically and nondestructively the 2507 SDSS in its as received condition in order to obtain its mechanical and nondestructive characteristics.

- Perform thermal aging treatments at 475 °C for different holding times in order to gradually induce the embrittlement in SDSSs.

- Characterize microstructurally, mechanically and nondestructively the samples of 2507 SDSS to characterize the material degradation.

- Evaluate the results of the nondestructive methods and their sensitivity to detect the effects of 475 °C embrittlement.

- Correlate the results of the nondestructive methods to the resulting microstructure and mechanical properties of the SDSS embrittled by aging treatment.

HYPOTHESIS

If stainless steels such as ferritic and duplex steels in industries are exposed to high temperatures in the 300 °C to 515 °C, the phenomenon known as the spinodal decomposition and/or the precipitation of phases produce embrittlement of these steels as a results of the transformation given by $\alpha \rightarrow \alpha + \alpha'$, where the resulting α' is a Cr-rich phase and α is a Fe-rich phase or precipitation and grown of α'phase, induces changes in physical properties that could be detected and characterized by nondestructive methods.

CHAPTER II. LITERATURE REVIEW

2.1. The stainless steels.

In 1821, the French engineer Pierre Berthier observed that adding a certain amount of chromium (Cr) to iron alloys, resulted in increment in mechanical properties as well as stiffness increased corrosion resistance to acids. Almost a century later, in 1909, the French scientists Leon Guillet and Albert Portevin studied independently the microstructure of Fe-Cr and Fe-Cr-Ni alloys. In 1911, the German metallurgist P. Monnartz, following Guillet and Portevin research, found a scientific explanation to the passivation mechanism and established the lowest percentage of Cr required to impart a corrosion resistance capability to steels. The name of stainless steel was given then and it has been used commonly to designate these type of steels in the United States and United Kingdom [10].

The demand for stainless steels has increased drastically in recent years as more and more companies specify these materials for their products. The different industries that utilize stainless steels components in many industrial processes include chemical, power, food and beverage, pharmaceutical and transportation. The different types of stainless steels owe their extensive use thanks to an improved combination of properties that give them advantages over other steels and nonferrous metals. The principal outstanding characteristics are their resistance to corrosion in many environments, their good mechanical properties over an extremely wide range of temperatures, and their superior resistance to oxidation and scaling at very high temperatures. These unique properties are achieved through substantial additions of Cr to Fe and C, with or without the addition of other elements such as Ni, Mn, Mo and N [11].

The stainless steels are a large family of Fe-Cr-based alloys (Fe-Cr or Fe-Cr-Ni) that are essentially low carbon steels that contain a high of Cr continent (Cr >12 wt. %.), that impart at least the same corrosion resistance conferred by pure Cr plates. The Cr content on the steel, allows the formation of a passivating layer of Cr oxide at the surface. This protective oxide film is resistant to corrosion in many chemical environments.

When this Cr percentage is locally reduced, for instance by precipitation of Cr carbide during heating, the corrosion protection is lost and a corroding process may occur. Moreover, the corrosion resistance and other useful properties of stainless steels are largely enhanced by increasing the Cr content usually well above 12 wt. %, the Cr content is usually 15 % and even goes up to 27 % in certain stainless steel grades as show in Figure 2.1. The corrosion resistant is commonly applied only to metals and alloys that are capable of sustained operation when exposed to attack by corrosive media at service temperatures below 315 °C. There are roughly more than 60 commercial grades of stainless steel available, and the global annual production was roughly 25 million tons in 2004 [10].

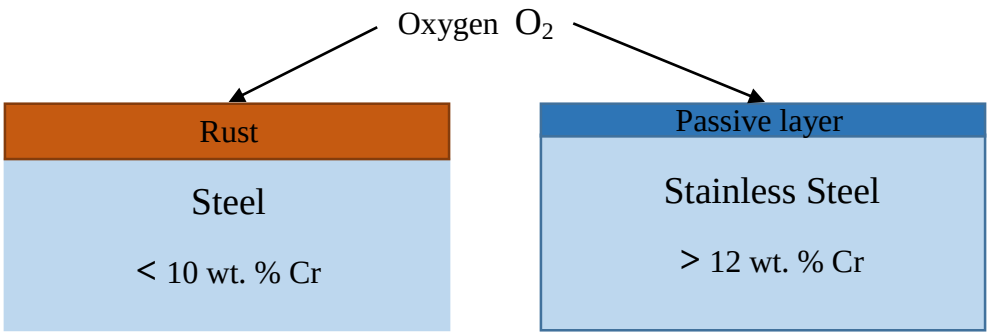

Figure 2.1. Protective oxide film in stainless steel and rust formation in steels.

2.2. Classification of stainless steels.

The stainless steels are chemically complex. The large number of alloying elements makes possible a larger range of possible phases. The three basic phases or microstructures of stainless steels are ferrite, austenite, and martensite [12]; these microstructures can be obtained by adjusting the chemical composition of the steel itself. The stainless steels may be divided into five main groups, the first four of which are based upon a common crystalline structure of the steels within the group. The fifth group, known as precipitation hardening steels, consists of alloys that can be hardened by an aging treatment [11]. Each group is identified by the alloying elements that affect their microstructure, as shown in the Table 2.1 and in the Figure 2.2.

Table 2.1. Classification of stainless steels by microstructure [10].

Type	**Typical composition** [wt. %]
Ferritic stainless steels	Cr: 17–30, C: < 0.2
Austenitic stainless steels	Cr: 18–25, Ni: 8–20
Duplex stainless steels	Cr : 18–26, Ni: 4–7, Mo: 2–3

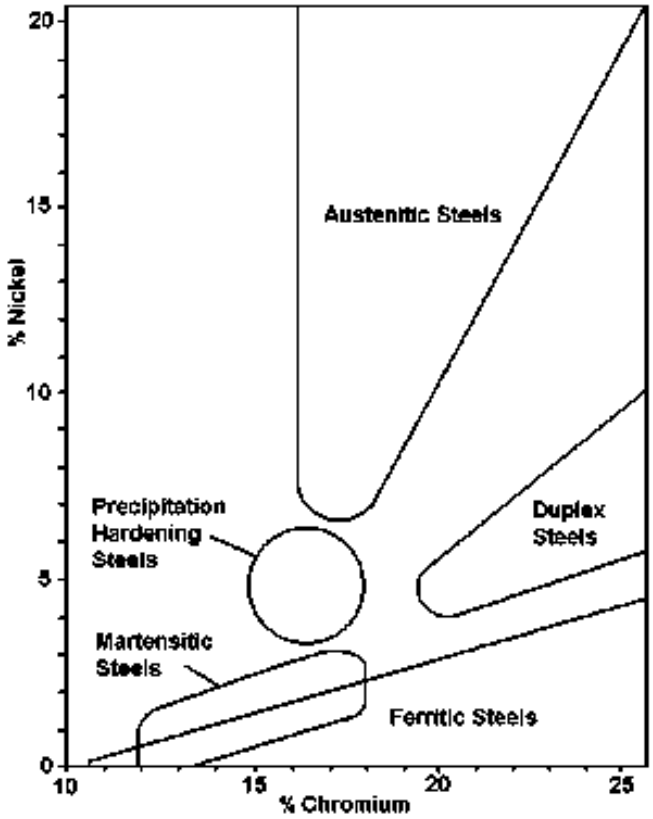

Figure 2.2. Cr and Ni composition for the different stainless steels [13].

2.2.1. Ferritic stainless steels.

The ferritic stainless steels (FSS), with American Iron and Steel Institute series denomination AISI-400, have a Cr content ranging from 17 to 30 %, with a lower carbon level, usually less than 0.2 wt. % C, than martensitic stainless steels [10]. The FSSs exhibit the following common characteristics:

1) They exhibit a BCC ferrite crystal lattice due to the high chromium content.

2) They are ferromagnetic and retain their basic microstructure up to the melting point if sufficient Cr and Mo are present.

3) They cannot be hardened by heat treatment, and they can be only moderately hardened by cold working; hence they are always used in the annealed condition.

4) In the annealed condition, their strength is ca. 50 % higher than that of carbon steels.

5) Like martensitic steels, they have poor weldability.

FSS are typically used where moderate corrosion resistance is required and where toughness is not a major need. They are also used where chloride stress-corrosion cracking (SCC) may be a problem because they have high resistance to this type of corrosion failure. In heavy sections, achieving sufficient toughness is difficult with the higher alloyed ferritic grades. Typical applications include automotive trim and exhaust systems and heat-transfer equipment for the chemical and petrochemical industries [10]. The two common grades are grade AISI 409, used for high-temperature applications, and grade AISI 430 shown in Figure 2.3, the most widely used grade.

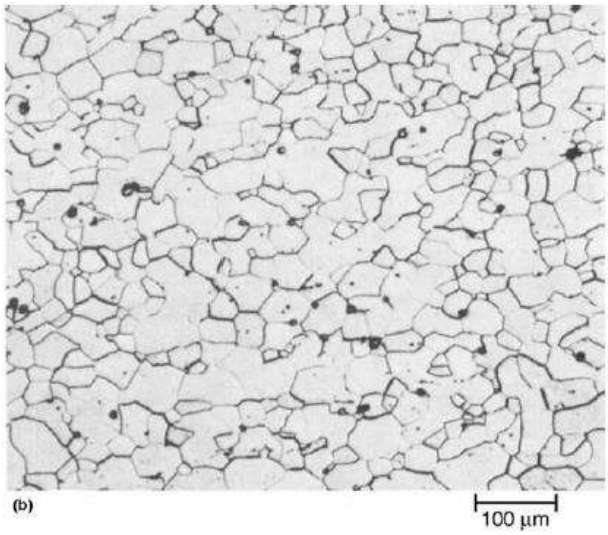

Figure 2.3. Microstructure of a ferritic stainless steel (type 430) annealed strip [14].

2.2.2. Austenitic stainless steels.

Austenitic stainless steels (ASS), which exhibit the unique austenite crystal structure even at room temperature, are the largest and most popular family of stainless steels. They were discovered around 1910 when Ni was added to Cr-bearing Fe alloys. Actually, ASS are Fe-Cr-based alloys containing at least 18 wt. % or more Cr; in addition, they also contain sufficient Ni and/or Mn to stabilize and insure a fully austenitic metallurgical crystal structure at all temperatures ranging from the cryogenic region to the melting point of the alloy. Carbon content is usually less than 0.15 wt. % C. As a general rule, they exhibit the following common characteristics [10]:

1) They possess an austenitic crystal lattice structure.
2) In contrast to other classes, they are not ferromagnetic even after severe cold working.
3) They cannot be hardened by heat treatment.
4) They can be hardened by cold working.
5) They have better corrosion resistance than other classes.
6) They can be easily welded.
7) They possess an excellent cleanability and allow excellent surface finishing.
8) They exhibit excellent corrosion resistance to several corrosive environments at both room and high temperatures.

However, the ASSs have some limitations [10]:

1) The maximum service temperature under oxidizing conditions is 450°C; above this temperature heat-resistant steels are required.
2) They are suitable only for low concentrations of reducing acid such as HCl; super austenites are required for higher acid concentrations.
3) In service and shielded areas, there might not be enough oxygen to maintain the passive oxide film and crevice corrosion might occur, in which case they must be replaced by super austenitics or duplex and super ferritic steels.
4) Very high levels of halide ions, especially the chloride ion, can lead to the breakdown of the passivating film.

It is important to note that upon heating carbon combines with chromium to form chromium carbide. If the chromium content falls below the critical percentage of 10.5 wt. % Cr, the corrosion resistance of the alloy is lost [10]. Wrought ASSs are classified according to the American Iron & Steel Institute (AISI) into three groups: AISI 200 series, i.e., alloys of Fe-Cr-Ni-Mn, AISI 300 series, i.e., alloys of Fe-Cr-Ni; and nitrogen-strengthened alloys (with the suffix N added to the AISI grade) [10]. Type 304 stainless steel is the most widely used steel of the austenitic group. it has a nominal composition of 18 % Cr and 8% Ni [11]. The microstructure of an ASS is shown in Figure 2.4.

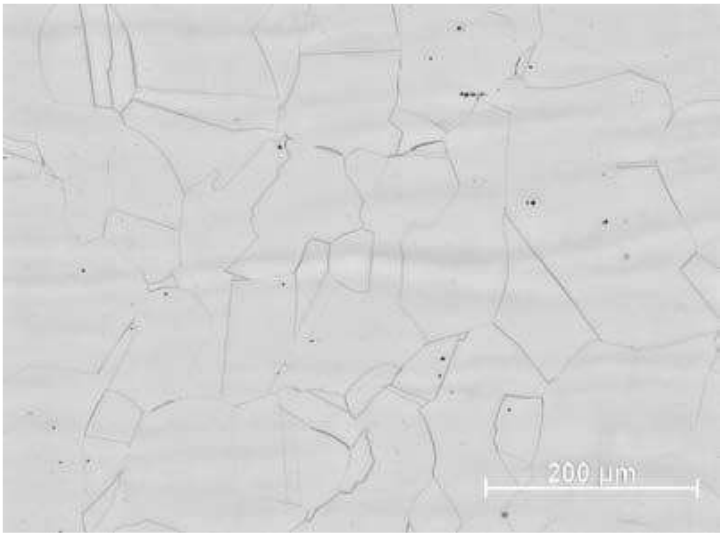

Figure 2.4. Austenite microstructure showing equiaxed grains and characteristic annealing twins. Normal presence of small inclusions can be observed [15].

2.2.3. Duplex stainless steels.

Duplex stainless steels (DSSs) are the newest and fastest-growing alloy group in the stainless steel family. They are called duplex because at room temperature they consist of two phases, ferrite and austenite, as seen in Figure 2.5. Duplex alloys have at least 20% chromium, they possess excellent strength, toughness, and corrosion resistance. They also display exceptional resistance to stress corrosion cracking (SCC) and corrosion fatigue but they are not high-temperature alloys because of embrittling phases. Their low nickel content makes them more economical than austenitic alloys of the same level of corrosion resistance, especially when their greater strength can be utilized to reduce the amount of material required. Their limitations lie in their lack of cryogenic toughness and their inability to withstand temperatures much above 300 °C without forming embrittling phases. But between –100 and 300 °C they are exceptional materials [12].

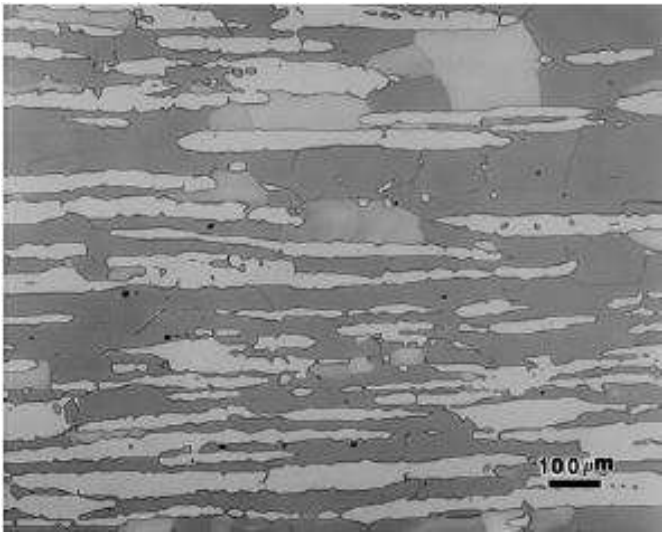

Figure 2.5. Wrought 2205 duplex microstructure, islands of austenite in a continuous matrix of ferrite [12].

They have the following characteristics [10]:

1) High resistance to stress-corrosion cracking.
2) Increased resistance to chloride ion attack.
3) High weldability.
4) Higher tensile and yield strengths than austenitic or ferritic stainless steels.

Table 2.2 lists the entire family of the DSSs, where the range of corrosion resistance depends on their alloy contents. The modern duplex stainless steels can be divided into five groups:

1) Lean alloy duplex stainless steels (also known generically as 2304 duplex) is cheap and Molybdenum free with a chemical composition of 23Cr – 4Ni – 0.1N. This type of DSS was designed to replace and improve the resistance to stress corrosion cracking of AISI 304 and 316 which is often used for construction purposes. The PREN for this type is equal to 25.

2) Standard duplex stainless steels (Also known generically as 2205 duplex) has a chemical composition of 22Cr – 5Ni – 3Mo – 0.17N with corrosion resistance lying between AISI 316 and 6 wt. % Mo + N super-austenitic stainless steel grades. In addition, they are the most popular and less expensive alloys in the duplex stainless steel family. They have a PREN ranging from 30 to 35.

3) 25 % Cr duplex (255) the chemical composition of this type of DSS is 25 Cr with different weight percentage content of Molybdenum, Nitrogen, and addition of Copper and Tungsten as alloy elements. The value of PREN for this type of DSS is in the range of 35 to 39.

4) Super duplex stainless steels (Also known generically as 2507 super duplex) the chemical composition of this type is 25Cr – 7Ni – 3.7Mo – 0.27N with a PREN value greater than 40. It has almost the same Chromium content of 25 % Cr Duplex with increased Mo and N. Sometimes the third and fourth types of DSS are merged as one group.

5) Hyper duplex stainless steels (with PREN greater than 45) designed and developed to increase operating performance and extend service life in severely corrosive applications, such as heat exchangers, has been launched recently by Sandvik. Hyper duplex such as SAF 3207 HD which has a minimum PREN of 50, containing 32 wt. % Cr and 7 wt. % Ni. Results from corrosion and mechanical testing show that SAF 3207 has better corrosion resistance and higher strength than SDSSs. The increase in strength is about 20% compared to SAF 2507.

Table 2.2. Chemical composition in wt. % of wrought Duplex Stainless Steel grades [1].

Type	UNS No.	EN No.	C	Cr	Ni	Mo	N	Mn	Cu	W
Rolled duplex stainless steels. First generation										
329	S32900	1.4460	0,08	23,0-28,0	2,5-5,0	1,0-2,0	---	1,00	---	---
	S31500	1.4424	0,03	18,0-19,0	4,3-5,2	2,5-3,0	0,05-0,1		---	---
	S32404		0,04	20,5-22,5	5,5-8,5	2,0-3,0	0,20	2,00	1,0-2,0	---
Duplex stainless steels. Second generation										
Lean alloy										
	S32001	1.4482	0,03	19,5-21,5	1,0-3,0	0,6	0,05-0,17	4,0-6,0	1,0	---
	S32101	1.4162	0,04	21,0-22,0	1,35-1,7	0,1-0,8	0,20-0,25	4,0-6,0	0,1-0,8	---
	S32202	1.4062	0,03	21,5-24,0	1,0-2,8	0,45	0,18-0,26	2,0	---	---
	S82011		0,03	20,5-23,5	1,0-2,0	0,1-1,0	0,15-0,27	2,0-3,0	0,5	---
2304	S32304	1.4362	0,03	21,5-24,5	3,0-5,5	0,05-0,6	0,05-0,20	2,5	0,05-0,6	---
		1.4655	0,03	22,0-24,0	3,5-5,5	0,1-0,6	0,05-0,20	2,0	1,0-3,0	---
Standard										
	S32003		0,03	19,5-22,5	3,0-4,0	1,5-2,0	0,14-0,20	2,0	---	---
2205	S31803	1.4462	0,03	21,0-23,0	4,5-6,5	2,5-3,5	0,08-0,20	2,0	---	---
2205	S32205	1.4462	0,03	22,0-23,0	4,5-6,5	3,0-3,5	0,14-0,20	2,0	---	---
25 % Cr										
	S31200		0,03	24,0-26,0	5,5-6,5	1,2-2,0	0,14-0,20	2,0	---	---
	S31260		0,03	24,0-26,0	5,5-7,5	2,5-3,5	0,10-0,30	1,0	0,2-0,8	0,1-0,5
	S32506		0,03	24,0-26,0	5,5-7,2	3,0-3,5	0,08-0,20	1,0	---	0,05-0,3
	S32520	1.4507	0,03	24,0-26,0	5,5-8,0	3,0-4,0	0,20-0,35	1,5	0,5-2,0	---
255	S32550	1.4507	0,04	24,0-27,0	4,5-6,5	2,9-3,9	0,10-0,25	1,5	1,5-2,5	---
Super duplex										
2507	S32750	1.4410	0,03	24,0-26,0	6,0-8,0	3,0-5,0	0,24-0,32	1,20	0,5	---
	S32760	1.4501	0,03	24,0-26,0	6,0-8,0	3,0-4,0	0,20-0,30	1,00	0,5-1,0	0,5-1,0
	S32808		0,03	27,0-27,9	7,0-8,2	0,8-1,2	0,30-0,40	1,10	---	2,1-2,5
	S32906		0,03	28,0-30,0	5,8-7,5	1,5-2,6	0,30-0,40	0,80-1,5	0,8	---
	S32950		0,03	26,0-29,0	3,5-5,2	1,0-2,5	0,15-0,35	2,00	---	---
	S39274		0,03	24,0-26,0	6,8-8,0	2,5-3,5	0,24-0,32	1,00	0,2-0,8	1,5-2,5
	S39277		0,025	24,0-26,0	6,5-8,0	3,0-4,0	0,23-0,33	0,80	1,2-2,0	0,8-1,2
		1.4477	0,03	28,0-30,0	5,8-7,5	1,5-2,6	0,30-0,40	0,80-1,5	0,8	---
Hyper duplex										
	S32707		0,03	26,0-29,0	5,5-9,5	4,0-5,0	0,30-0,50	1,50	1,0	---
	S33207		0,03	29,0-33,0	6,0-9,0	3,0-5,0	0,40-0,60	1,50	1,0	---

2.3. Chemical composition.

An important aspect related to DSSs is the phase balance control, because it has a direct impact on corrosion and mechanical properties. Chemical compositions, as well as thermomechanical treatments of modern DSSs are usually selected to produce volume fraction of the ferrite constituent. Chemical composition is used for the classification of DSSs by calculating pitting resistance equivalent (PRE), sometimes also called PREN, since it takes into account the nitrogen content [16]. The most common way of ranking stainless steels for their Pitting Resistance Equivalence Number (PREN) according to the relation between the amount of the essential elements and the corrosion properties can be formulated by using this relation:

PREN = [wt. % Cr] + 3.3 [wt. % Mo] + 16 [wt. % N].....(2.1)

However, for DSSs it is necessary to consider the pitting resistance of ferrite and austenite individually due to the partitioning of the alloying elements between the phases, especially if the heat treatment is not optimized. Many researchers have pointed out that PREN calculated from the bulk alloy composition may be misleading in duplex alloys because they contain austenite and ferrite [17], which have different compositions. Austenite is enriched with N whereas ferrite is richer in Cr and Mo. In general, it has been found that austenite has a higher PREN than ferrite.

On the other hand, Okamoto showed theoretical calculation results that, by adjusting the ferrite/austenite balance via adjusting Ni and the heat treatment temperature, it is possible to achieve an equal PREN for both ferrite and austenite [18]. With the introduction of tungsten as an active alloying element, the following expression has been proposed:

PREN = [wt. % Cr] + 3.3 [wt. % Mo] + 0.5 [wt. %W] + 16 [wt. % N].....(2.2)

Therefore, higher PREN numbers mean higher resistance to pitting corrosion. However, PREN numbers only provide an approximate grading of alloys and do not account for the microstructure of the material.

2.3.1. Influence of alloying elements.

Stainless steels contain a number of alloying additions (other than Cr, C and Ni) that are intended to improve mechanical properties and corrosion resistance or to control the microstructure. Stainless steels are Fe-base alloys with Fe contents ranging from 50 to 88 wt. % of the composition. The principal alloying additions to stainless steel are Cr and C for the ferritic and martensitic grades, with the addition of Ni for the austenitic and duplex grades. Essentially all of the stainless steels contain Mn and Si as intentional additions. Other alloying additions include molybdenum, niobium, titanium, aluminum, copper, tungsten, nitrogen, and others to improve fabricability, develop special properties, enhance corrosion resistance, or influence microstructure. Impurity elements commonly found in stainless steels include nitrogen, oxygen, sulfur, and phosphorus. All of these alloy and impurity elements have some effect on weldability and performance. In most cases, the level of these elements in the base or filler metal is controlled by the material specification to assure that the steel performs as anticipated [19].

2.3.1.1. Chromium (Cr).

Chromium is added primarily for a protection of the steel. With the addition of Cr, an oxide of stoichiometry $(Fe, Cr)_2 O_3$ forms on the steel surface. The presence of Cr increases the stability of the oxide since it has a much higher affinity for oxygen than does the iron. When the Cr level exceeds approximately 10.5 wt. %, the steel is considered “stainless” under ambient conditions. Higher levels of Cr may be required for oxide stability in more aggressive environments [19]. Figure 2.6 shows the important role of Cr in making the Fe surface passive by forming a Cr-rich surface oxide film that protects the underlying metal from corrosion. This oxide film is the main advantage of the addition of Cr to the steels improving the corrosion resistance [20].

Cr is also a ferrite promoter, increasing Cr will promote ferrite formation and retention in martensitic and duplex grades. Since, Cr is the primary alloying element stabilizing the ferritic microstructure [19].

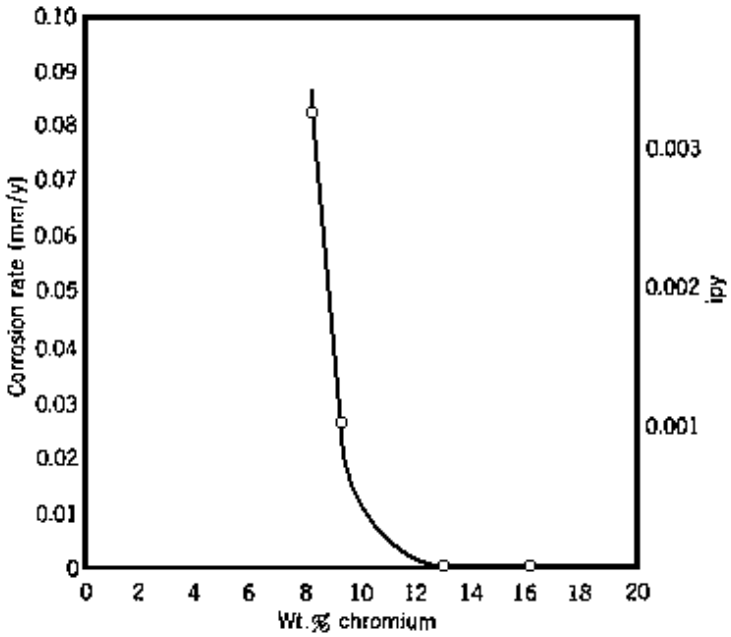

Figure 2.6. Corrosion rate profile with respect to Cr contents in intermittent water spray at room temperature [21].

Cr is also a strong carbide former. The more common Cr-rich carbide is $M_{23}C_6$, where the "M" is predominantly Cr but may also have some fraction of Fe and Mo present. This carbide is found in virtually all the stainless steels. It is also possible to form a Cr_7C_3 carbide. Other complex carbides and carbonitrides $M_{23}(C,N)_6$ are also possible [22]. Cr also combines with N to form a nitride. The most common is Cr_2N, which has been observed in both ferritic and duplex grades [19]. The Cr is also a key ingredient in the formation of intermetallic compounds, many of which tend to embrittle the stainless steels [1, 23]. The most common is sigma phase (σ), also present in chi (χ) and Laves intermetallic phases [19]. From a mechanical properties standpoint, Cr will provide some degree of solid solution strengthening since it is a substitutional atom in both the BCC and FCC crystal lattices. High Cr levels in ferritic alloys can result in very poor toughness and ductility, particularly when carbon and nitrogen are present. High-Cr ferritic grades must be treated very carefully, or carbon and nitrogen reduced to very low levels, to have acceptable mechanical properties in welded fabrication [19].

2.3.1.2. Nickel (Ni).

The primary function of Ni is to promote the austenite phase such that predominantly austenitic or austenitic-ferritic alloys can be produced as shown in Figure 2.7. By adding sufficient Ni, the austenite phase field can be greatly expanded such that austenite is stable to room temperature and below [19]. Ni is not strong carbide former and does not generally promote the formation of intermetallic compounds, although there is evidence that its presence in the alloy may influence precipitation kinetics [22]. There is some evidence that the presence of Ni in ferritic alloys improves general corrosion resistance, particularly in reducing environments such as those containing sulfuric acid. However, Ni has been associated with a decrease in stress corrosion cracking (SCC) resistance [24]. Ni is a good solid solution strengthener but is most beneficial in terms of improving toughness in both the martensitic and ferritic grades. Additions of up to 2 wt. % Ni to high-Cr ferritic stainless steel can dramatically reduce the ductile-to-brittle fracture transition temperature (DBTT) [25].

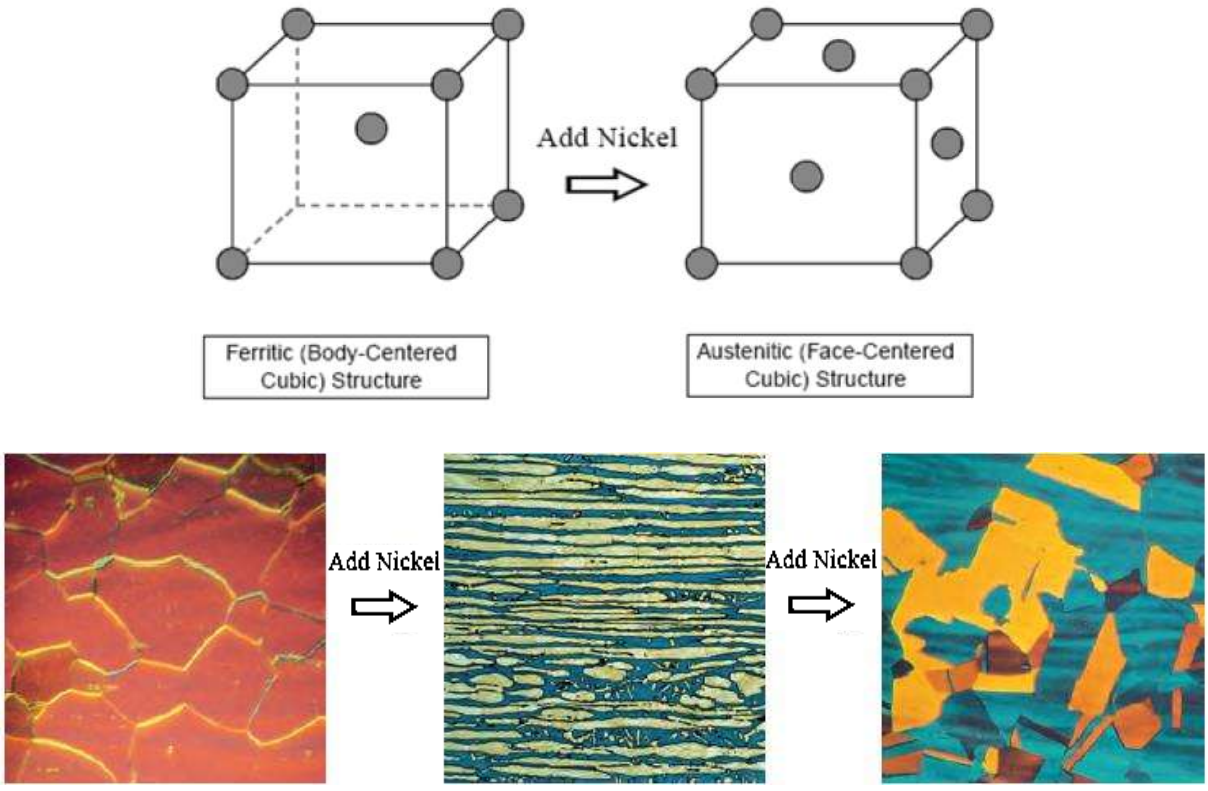

Figure 2.7. Effect of Nickel addition to stainless steels [1].

2.3.1.3. Molybdenum (Mo).

Molybdenum is added to a number of stainless steels and has different functions depending on the particular grade. For the ferritic, austenitic, and duplex grades, Mo is added in amounts up to 6% or more in super austenitics in order to improve corrosion resistance, particularly with respect to local corrosion such as, pitting and crevice corrosion [19]. The mechanism by which Mo increases the pitting resistance has been found to be the suppression of active sites via formation of an oxy-hydroxide or molybdenum ion [26].

An addition of at least 3% is recommended while 4% is thought to be an upper limit to prevent crevice corrosion in high temperature sea water. Mo also improves elevated temperature strength [22]. This can also have a negative effect, since alloys containing Mo will be more difficult to hot work. The addition of as little as 0.5 wt. % Mo increases the secondary hardening characteristics of the steel, resulting in higher room temperature yield and tensile strength and improved elevated temperature properties [19]. Mo is a ferrite promoting element and has a similar effect on ferrite stability as Cr, ferrite formation and retention in the microstructure. This can a potential problem in the martensitic grades, where residual room temperature ferrite can reduce toughness and ductility [19].

2.3.1.4. Nitrogen (N).

Nitrogen is usually present as an impurity in many of the stainless steels but is an intentional addition to some of the austenitic and almost all the duplex grades. N is a powerful solid solution strengthening agent, and additions of as little as 0.15 wt. % can dramatically increase the strength of austenitic alloys [27]. It partitions to the austenite due to the increased solubility in the phase and also concentrates at the metal passive film interface [28]. For the DSSs, N is added to improve strength, but more important, to increase resistance to pitting and crevice corrosion. Some duplex grades contain up to 0.3 wt. % N. the solubility of N in stainless steels is relatively low, particularly in the ferrite phase. In the ferritic and duplex grades, Cr_2N will precipitate in the ferrite phase if the solubility limit is exceeded, as can be observed in the weld metals and HAZs of these alloys if appreciable austenite fails to form during cooling from temperatures above about 1100°C [19].

N like Ni, is a strong austenite former and can often be used in place of Ni for austenite stabilization since it is more effective than Ni. N is essential in the newer duplex grades for increasing the austenite content, diminishing Cr and Mo segregation, and for raising the corrosion resistance of the austenitic phase. N also effectively increases strength without the risk of sensitization, gives a good improvement in weldability, increases localized corrosion performance, and critical pitting temperature (CPT) more effectively than Cr [29].

2.3.1.5. Manganese (Mn).

Manganese is added to virtually every steel. In ASSs, it is normally present in the range 1 to 2 wt. %. In FSSs and MSSs, it is more commonly present at less than 1 wt. %. Historically, it was added to prevent hot shortness during casting. This is a form of solidification cracking that is associated with the formation of low melting point iron-sulfide eutectic constituents. Since Mn combines much more readily with sulfur than does iron, the addition of sufficient Mn and the formation of stable Mn sulfide (MnS) effectively eliminated the hot shortness problem [19].

Mn is considered to be an austenite-promoting element, although the degree of promotion is dependent on the amount present and the level of Ni. It's very effective in stabilizing austenite at low temperature to prevent transformation to martensite. Its potency in promoting austenite at elevated temperature is dependent on the overall composition of the alloy. In ASS Type 304, it appears to have little effect on promoting austenite versus ferrite. Mn is sometimes added to specialty alloys to increase the solubility of N in the austenite phase. The Mn effect on mechanical properties is minimal. It provide some solid solution strengthening and appear to have little effect on embrittlement[19]. Mn is generally used in stainless steels in order to improve hot ductility [15].

2.3.1.6. Copper (Cu).

Copper additions improve corrosion resistance of SDSSs in many not oxidizing acids, but the amount is limited to 2 wt. % due to a reduction in hot ductility with higher amounts. Higher amounts of Cu in SDSSs will also lead to formation of epsilon phase (ε), which reduces the pitting resistance [30].

Cu addition to high alloy ASSs is used to decrease the corrosion rate in non-oxidizing environments such as sulphuric acid [31]. Cu can also be added to decrease work hardening in grades for improved machinability. It may also be added to improve formability [15].

Cu, aluminum (Al), titanium (Ti) and Mo can be added to stainless steels to promote a precipitation reaction that hardens the alloy. The P-H martensitic alloys contain Cu, Al and Mo and can be heat-treated to produce room-temperature yield strengths in excess of 1375 MPa. Cu is a weak austenite promoting element [19].

2.3.1.7. Carbon (C).

Carbon is present in all steels, but unlike C-Mn and low alloy structural steels, it is usually desirable to control C below 0.1 wt. %. In solution, C provides an interstitial strengthening effect, particularly at elevated temperatures. In most alloys, C combines with other elements to form carbides, in the case of Cr-rich $M_{23}C_6$ carbides, a degradation in corrosion resistance can result, and for this reason low-C (L-grade) alloys are produced where C is kept below 0.04 wt.% [19].

The C content of most wrought DSSs is limited to 0.02% or 0.03%, primarily to suppress the precipitation of Cr-rich carbides which can act as initiation sites for pitting corrosion and intergranular attack. Similarly, sulphur (S) and phosphorus (P) contents are controlled, although not eliminated as the presence of some S is important for weld bead penetration. Nowadays, levels of C and S can be controlled by the modern steel making processes, while P contents can be reduced using good melting practice [29].

C is a strong austenite former that also significantly increases the mechanical strength. However, it also reduces the resistance to intergranular corrosion caused by carbide formation. The modern grades do not suffer from intergranular corrosion due to the low carbon content. In FSSs C will strongly reduce both toughness and corrosion resistance. In the martensitic steels C increases hardness and strength, but decrease the toughness [15].

2.3.1.8. Tungsten (W).

Tungsten additions of up to 2 % in DSSs improve pitting resistance [15, 18, 19, 32], i.e. extend the passive potential range and reduce i pass, as shown in Figure 2.8. Similarly, W increases crevice corrosion resistance in heated chloride solutions. This is thought to be due to the adsorption of W into the passive layer without modification of its oxide state. However, in acid chloride solutions W appears to pass from the substrate into the passive film by interaction with water to form insoluble WO_3. In neutral chloride solutions, WO_3 interacts with other oxides increasing their stability and bonding to the substrate [29].

W is known to encourage intermetallic formation in the 700 to 1000°C temperature range as shown in Figure 2.9, and encourages secondary austenite formation in weld metal. It is believed to be thermodynamically equivalent, but kinetically non-equivalent, to Mo with respect to sigma formation. However, levels between 1% and 3% have been shown to restrict the formation of sigma at the phase boundaries and, instead, precipitation occurs at intragranular sites [29].

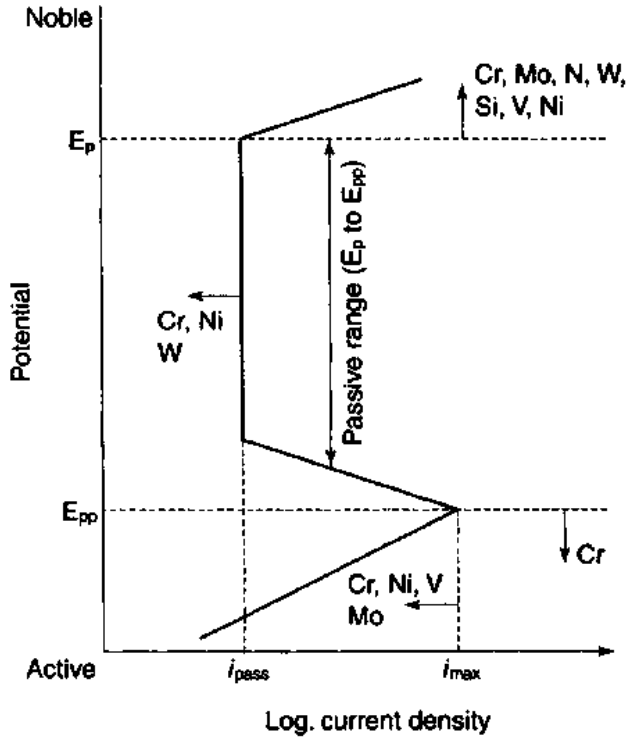

Figure 2.8. Schematic summary of the effects of alloying elements on the anodic polarization curve [29].

This is thought to be due to the large W atom influencing the diffusion of Mo and W at the phase boundaries and thus nucleation of sigma. Notwithstanding this, W alloyed weld metal has been shown to form chi phase more rapidly than otherwise similar deposits without the addition [18, 29]. Nevertheless, a W content of 1% is usually not exceeded in a 4 % Mo duplex steel, with 2 % W added to steels with about 3 % Mo [29].

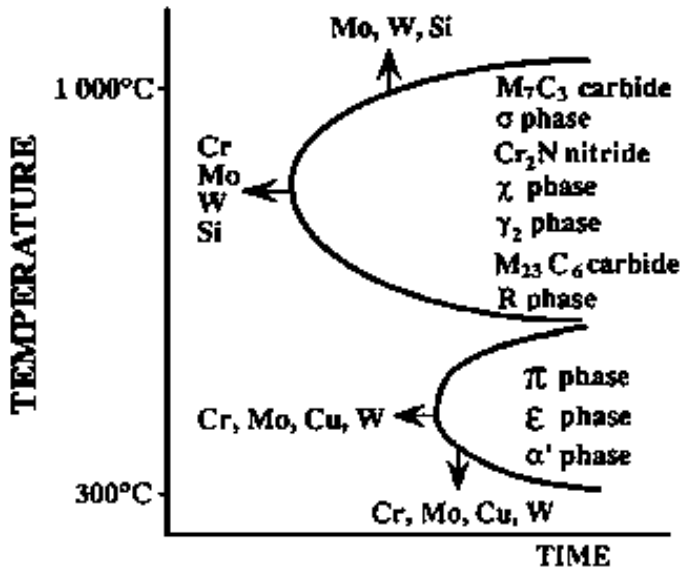

Figure 2.9. Schematic summary of the effects of alloying elements on the formation of various precipitates [29].

2.3.1.9. Silicon (Si).

Silicon is also present in virtually all stainless steels and added primarily for deoxidation during melting. In most alloys it is present in the range 0.3 to 0.6 wt. %. In some cases Al may be substituted as a deoxidizer, but this is rarely the case in stainless steels [19]. It has been found to improve corrosion resistance in DSSs when present at levels of 4 to 5 wt. % have been developed with increased pitting resistance as shown in Figure 2.8, and a claimed immunity to stress corrosion cracking (SCC), nevertheless, as Si is generally considered to enhance sigma formation and combination of Si and Mo can be particularly dangerous as shown in Figure 2.9, also is added to some heat-resisting alloys in the range 1 to 3 wt. % to improve oxide scaling resistance at elevated temperature [15, 19, 29].

The role of Si in promoting ferrite or austenite is not entirely clear. In ASSs, up to 1 wt. % seems to have no effect on the phase balance, but higher levels appear to promote ferrite. In FSS and MSSs, Si appears to help promote ferrite [15, 19]. Silicon forms a number of iron silicide's (FeSi, Fe_2Si, Fe_3Si, Fe_5Si_3) and a Cr_3Si intermetallic, all of which tend to embrittle the structure. It also expands the composition range over which sigma form [33]. Si is known to segregate during solidification, resulting in the formation of low melting eutectic constituents, particularly in combination with Ni. For these reasons, it is usually help below 1 wt. % [19, 29]. Silicon is well known to improve the fluidity of molten steel. For this reason, it may be added in somewhat higher than normal amounts to weld filler metals. Some stainless steels, particularly the austenitic grades, tend to be quite sluggish in the molten state, and the addition of Si can greatly improve the fluidity [19].

2.3.1.10. Other elements.

There are a number of other intentional alloying additions made to various stainless steels for very specific applications.

- Titanium (Ti) is a strong ferrite former and a strong carbide former, thus lowering the effective C content and promoting a ferritic structure in two ways. In austenitic steels with increased C content it is added to increase the resistance to intergranular corrosion, but it also increases the mechanical properties at high temperatures. In FSSs Ti is added to improve toughness, formability and corrosion resistance. In martensitic steels Ti lowers the martensite hardness by combining with C and increases the tempering resistance. In P-H steels Ti is used to form the intermetallic compounds that are used to increase the strength [15].

- Vanadium (V) forms carbides and nitrides at lower temperatures, promotes ferrite in the microstructure, and increases the toughness. It increases the hardness of martensitic steels due to its effect on the type of carbide present. It also increases tempering resistance. It is only used in hardenable stainless steels [15].

- Niobium (Nb) is both a strong ferrite and carbide former. Like Ti, it promotes a ferritic structure. In austenitic steels it is added to improve the resistance to intergranular corrosion, but it also enhances mechanical properties at high temperatures. In FSSs Nb and/or Ti is sometimes added to improve toughness and to improve resistance to sensitization to minimize the risk for intergranular corrosion. In martensitic steels Nb lowers the hardness and increases the tempering resistance. In the US it is designated Columbium (Cb) [15].

- Aluminum (Al) improves oxidation resistance, if added in substantial amounts [19]. It is used in certain heat resisting grades for this purpose. In P-H steels Al is used to form the intermetallic compounds that increase the strength in the aged condition [15].

- Cobalt (Co) is an effective solid solution strengthener, and in the MSSs it can be added to increase the martensite start temperature. Co promotes austenite formation [19]. It increases the hardness and tempering resistance, especially at higher temperatures [15].

- Sulfur (S), Selenium (Se), and Lead (Pb) are added to free-machining grades to improve machinability by allowing higher machining speeds and improved tool live. These additions reduce the corrosion resistance and typically make the alloys unwieldable, although control of solidification behavior (primary ferrite versus primary austenite) may negate the effect of sulfur [19].

- Cerium (Ce) is one of the rare earth metals and is added in small amounts to certain heat resisting grades in order to increase the resistance to oxidation at high temperature [15].

The Table 2.3 summarizes the effects of alloying elements on the ferrite and austenite phases and on corrosion properties.

Table 2.3. Effects of different alloying additions and microstructure on the pitting and crevice resistance of DSSs [34].

Alloying	Effect	Reason	Practical Limitation
C	Negative	Causes precipitation of chromium carbides with accompanying chromium depleted zones	About 0.03% maximum
Si	Positive	Si Stabilizes the passive film	About 2% maximum, due to its effect on structural stability and on nitrogen solubility
Mn	Negative	Mn-rich sulphides act as initiation sites for pitting. Mn may also destabilize the passive film	About 2%. Higher level may increase the risk of intermetallic precipitation
S	Negative	Sulphides if not Cr-Ti or Ce rich, tend to initiate pitting attack	About 0.003%, if maximum pitting resistance required. For reasonable machining, up to 0.02% allowed
Cr	Positive	Cr stabilizes the passive film	Between 25 and 28% maximum depending on the Mo content. Higher Cr content increases the risk of intermetallic precipitation
Ni	Negative	Increased Ni, other elements constant, dilutes the γ- phase with regard to N, which in turn decreases the PRE of the γ- phase. If the alloy is very sensitive to precipitation of chromium nitrides, Ni can have a positive effect	Ni should primarily be used to give the alloy desired austenite content.
Mo	Positive	Mo stabilizes the passive film, either directly or through enrichment beneath the film	About 4–5% depending on the Cr content. Mo enhances the risk of intermetallic precipitation
N	Positive	N increases the PREN of the γ phase, not only be increasing the N content of that phase, but also by increasing the Cr and Mo contents through their partitioning coefficients	About 0.15% in Mo free grades. About 0.3% in super duplex and some in 0.4% in 25%Cr, high Mo, high Mn alloys
W	Positive	Probably same as Mo	Increases the tendency of intermetallic precipitation
Cu	Disputed	Marginal positive and negative effect	About 2.5% maximum. Higher levels reduce hot workability and undesirable hardenability

2.3.2. Microstructure of duplex stainless steels.

DSSs are characterized by a two phase structure, which consists of a mixture of about 50 % volume FCC austenite islands in BCC ferrite grains. Both cast and wrought products have roughly equivalent volume fractions of ferrite and austenite, in the case of wrought components, contain a rolling texture obtained by hot working, followed by a solution annealing and quench [29].

The optimum phase balance for wrought products varies, but overall a range of between 45% and 60% austenite may be expected. The structure is obtained by simultaneous control of the chemical composition and annealing temperature [29].

2.3.2.1. Ferrite promoting versus austenite promoting elements.

Stainless steels are iron base alloys containing from 12 to over 50 wt. % alloying additions. Alloying elements affect the equilibrium phase relationships relative to the stability of the austenite and ferrite phases. Elements added to stainless steels can be divided into those that promote, or stabilize, either the ferrite or the austenite phase [29].

Chromium, molybdenum, silicon, niobium, titanium, aluminum, vanadium and tungsten are often used as ferrite forming elements, while nickel, manganese, carbon, nitrogen, copper and cobalt are often used as austenite forming elements [19]. The volume fraction of each phase in DSS depends on the chemical composition and heat treatment. The ferrite content can vary between 35 and 55 %, but manufacturers balance the steels close to the ideal 50 - 50 % ferrite/austenite ratio [35].

2.3.2.2. Effects of alloying elements on phase balance.

The effect of the alloying elements on the microstructure of stainless steels is summarized in the empirical Schaeffler DeLong diagram shown in Figure 2.10. The diagram is based on the fact that the alloying elements can be divided into ferrite-stabilizers and austenite-stabilizers. This means that they favour the formation of either ferrite or austenite in the microstructure. If the austenite stabilizers ability to promote the formation of austenite is related to that for nickel, and the ferrite-stabilizers likewise compared to chromium, it becomes possible to calculate the total ferrite and austenite stabilizing effect of the alloying elements in the steel [15].
This gives the so-called chromium and nickel equivalents in the Schaeffler DeLong diagram:

Nickel equivalent = % Ni + 0.5 [% Mn] + 30 [%C].....(2.3)

Chromium equivalent = % Cr + % Mo + 1.5 [% Si] + 0.5 [% Nb].....(2.4)

In this way it is possible to take the combined effect of alloying elements into consideration. The Schaeffler diagram was originally developed for weld metal, i.e. it describes the structure after melting and rapid cooling but it has also been found to give a useful preview of the effect of the alloying elements for wrought and annealed material. However, annealed steels with predicted ferrite contents in the range 0 – 5 % according to the diagram contain in practice smaller amounts of ferrite [15].

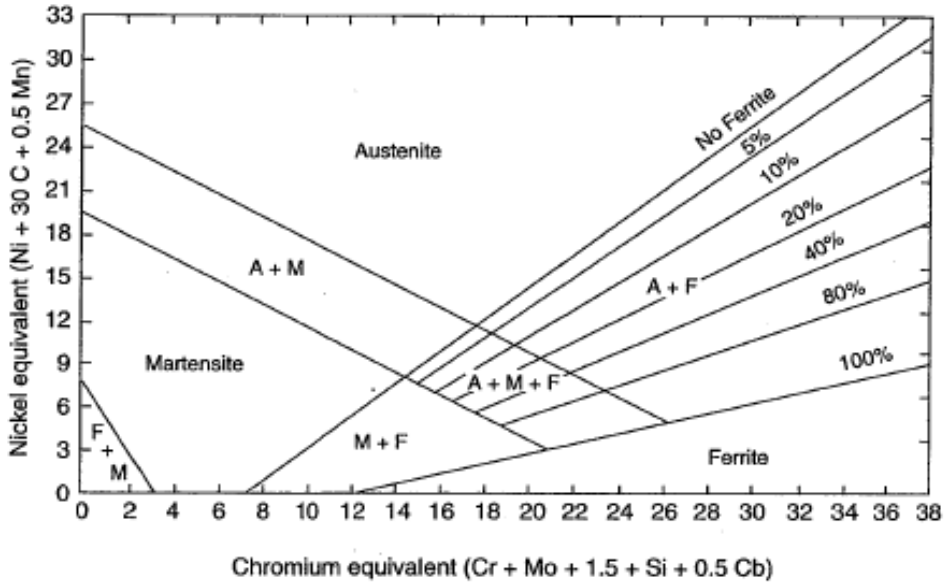

Figure 2.10. Schaeffler diagram of 1949 [36].

It should also be mentioned that the Schaeffler diagram is not the only diagram for assessment of ferrite contents and structure of stainless steels.

2.3.3. Metallurgy of duplex stainless steels.

Stainless steels are designed by carefully balancing the alloying elements so that an appropriate microstructure is maintained during processing and the required final structure and properties are achieved by heat treatment. Inappropriate heat treatment, service at high temperatures or welding can, lead to the formation of other phases. These may be thermodynamically stable or kinetically favored in lower temperature regimes and can have a major influence on mechanical properties and corrosion resistance.

2.3.3.1. Austenite-Ferrite phase balance.

DSSs are based on the Fe-Cr-Ni-N alloy system. The chemical compositions of these have been adjusted such that the base metal microstructure consists of nominally 50% ferrite and 50% austenite, hence the term duplex. However, all DSSs solidify as virtually 100% ferrite and depend on partial solid-state transformation to austenite for this balanced microstructure. N is usually added as an alloying element to accelerate formation of the austenite phase and stabilize it, and also to improve pitting corrosion resistance [19], with the high temperature stability of the duplex structure being influenced more by N content, than by Cr or Mo. The addition of 0.25 % N to a 25 % Cr alloy produces a ferrite volume fraction of about 50% at 1250 °C, compared to nearly 80% ferrite with 0.18 % N. Nevertheless, it is difficult to predict the microstructure of a duplex alloy from simplified diagrams, due to the effects of other alloying elements [29]. Figure 2.11 indicates that alloys whose WRC-1992 Cr equivalent is about 1.85 times their Ni equivalent, or more, will solidify as 100% ferrite. The DSS base metals typically have ratios between about 2.25 and 3.5. At high temperatures (above the ferrite solvus), the alloys remain 100% ferrite. Austenite can only nucleate and grown below the ferrite solvus. Annealing and hot-working operations of these steels are generally performed at temperatures below the ferrite solvus, where the austenite and ferrite can coexist in equilibrium. By controlling the processing temperature and cooling rate from that temperature, the proportion and distribution of ferrite and austenite can be controlled in the wrought product [19]. Although constitution tie-lines cannot be drawn any reasonable accuracy in a pseudobinary diagram, it should be evident from Figure 2.11 that alloys annealed or hot worked at temperature near the ferrite solvus, followed by quenching, can be excepted to contain mostly ferrite, with only small amounts of grain boundary austenite. As the temperature of annealing or hot working is reduced, the equilibrium microstructure will contain progressively more austenite and less ferrite [19].

Under equilibrium conditions, there is a partitioning of the alloy elements, so that the ferrite promoting elements (Cr, Mo, W) will concentrate, by diffusion, into the ferrite. At the same time, the austenite promoting elements (Ni, C, N, and Cu) will concentrate, by diffusion, into the austenite. With falling temperature, the equilibrium compositions of the ferrite and austenite are continually changing, according to the austenite and ferrite solvus line compositions. At the same time, diffusion is slowing with falling temperature.

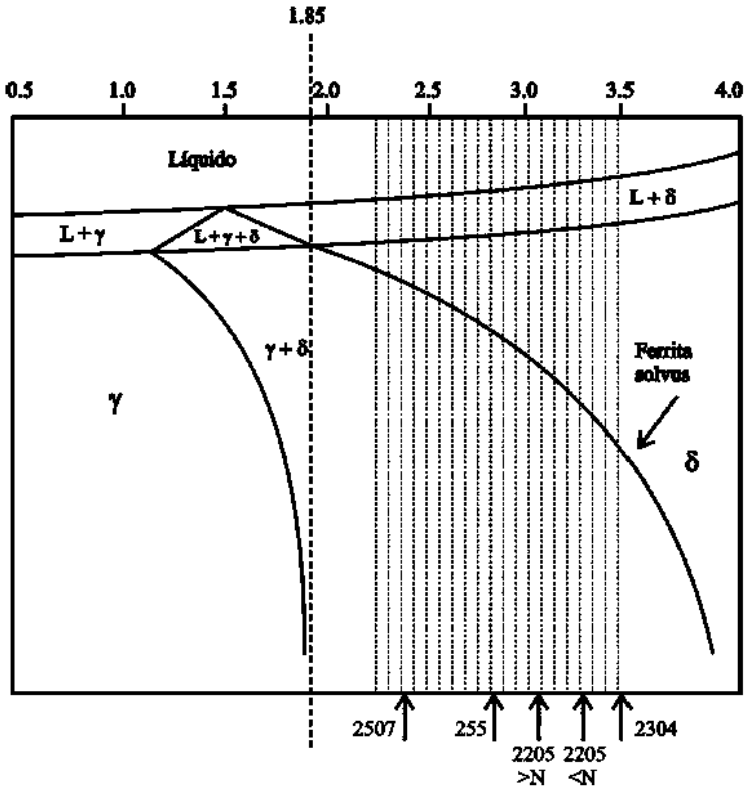

Figure 2.11. Elevated temperature region of a pseudobinary phase diagram for DSS compositions. Shaded region represents the range for commercial alloys [19].

At some temperature during cooling, diffusion can no longer keep pace with the equilibrium compositions of the two phases, and whatever compositions and phase balance are present at that time and temperature are then frozen into the alloy, as if it had been quenched from that temperature [19].

In a DSS, if the effective quench temperature is high [37] (close to the ferrite solvus temperature), the phase balance will be very high in ferrite. If the effective quench temperature is well below the ferrite solvus temperature, there will be more austenite. Hot working speeds diffusion, so that a lower effective quench temperature is more easily obtained for wrought DSSs than for cast DSSs or for weld metals. Cast DSSs obtain their ambient temperature microstructures by annealing at temperatures at or above 1040 °C, followed by quenching [38]. In practice, the annealing temperature, or hot working temperature, is chose as low as possible but sufficiently high to take into solution any precipitate phases [23]. This practice minimizes the amount of N remaining in the ferrite phase [19].

2.3.3.2. Precipitation reactions.

The curvature of the two phase ferrite + austenite region of Figure 2.11 indicates that more austenite will be formed, at the expense of ferrite, at lower hot working or annealing temperature (effective quench temperatures). However, a lower limit on these temperatures is imposed by the appearance of undesirable precipitates within the ferrite phase. Because of the complex alloying of the duple grades, a number of precipitation reactions can occur over a range of temperatures from below approximately 1000 °C. All of these precipitation reactions are time and temperature dependent, as indicated schematically in Figure 2.9. Many of these precipitates embrittle the duplex alloys and are to be avoided. These include sigma (σ), chi (χ), and alpha prime (α′), as well as chromium nitride. Also, it should be noted that the addition, or increased levels, of Cr, Mo, and W tend to accelerate the formation of these precipitates, particularly the sigma and chi phases. This acceleration has potential implications with respect to embrittlement during post-weld heat treatment or multipass welding. The lower temperature precipitation reactions effectively limit the use of the duplex alloys to temperatures below 280 °C [19].

For the DSS grades, which solidifies ferritically and then undergoes solid state transformation. The austenite forms both along grain boundaries. The final microstructure after annealing contains approximately equal fractions of austenite and ferrite. In order to achieve the correct phase balance it is important that DSSs are annealed within a fairly narrow temperature window, typically 950–1120 °C [15].

2.3.4. Heat treatment of duplex stainless steels.

The optimal microstructure of DSS contain approximately equal amounts (50%) of ferrite and austenite, and offer good combinations of mechanical properties and corrosion resistance. This can be obtained by solution annealing at 1050 – 1150 °C followed by rapid cooling. The temperature of this solution annealing heat treatment is a parameter that affects the corrosion properties of the steel [39]. SDSS are prone to the formation of intermetallic precipitates and secondary phases, which may form in the temperature range of 300 – 1000 °C, during isothermal aging or incorrect heat treatment [16].

The recommended annealing temperature is about 1100 °C for DSS and SDSS containing molybdenum, since the formation of intermetallic precipitates and secondary phases is possible up to about 1050 °C. The situation in a welded part of SDSS is more complex. The balance of alloying elements can be disturbed, either by formation of intermetallic precipitates and Cr_2N, or by excessive precipitation of secondary austenite (γ_2). Redistribution of alloying elements may lead to local reductions in pitting resistance [32]. This can happen either in regions that are depleted with respect to crucial alloying elements or in precipitates.

Structural changes can occur in the DSSs during isothermal or anisothermal heat treatments. Most of these transformations are concerned with the ferrite, as element diffusion rates are approximately 100 times faster than in austenite. Due to it is less compact lattice of the BCC crystal structure. Moreover, as already mentioned, the ferrite is enriched in Cr and Mo, which are known to promote the formation of intermetallic phases. Furthermore, element solubility in the ferrite falls with a decrease in temperature, increasing the probability of precipitation during heat treatment [29].

Time-temperature transformation (TTT) diagrams, generated by isothermal heat treatment followed by quenching, are often employed to depict the susceptibility of different grades to embrittlement and shown in Figure 2.12. In this diagram, within the 600-1050°C temperature range, the curves are based on optical microscope observations, while in the range 300-600°C, they are determined from hardness measurements. The diagrams are conservative in nature and do not imply that the mechanical properties or corrosion resistance are modified as soon as the boundaries indicated are reached, although an effect on properties may be noticed before the boundaries are reached [29].

2.3.4.1. Temperatures above 1050 °C.

DSSs solidify completely in the ferrite field, for standard grades and normal cooling rates. This is followed by solid state transformation to austenite, which is naturally reversible, so that any large increase in temperature, from l050°C to 1300°C, leads to an increase in ferrite content. Further, as the temperature increases, there is a reduction in the partitioning of substitutional elements between the phases. In addition, the ferrite becomes enriched in interstitial elements such as C and N [29].

2.3.4.2. The 600-1050 °C nose.

Intermetallic precipitation strongly depends on sample chemistry, concentration of sigma forming elements such as Cr, Mo at this temperature range. Thus, S32304 grade, leaner with Cr and Mo, found to be the least prone to intermetallic precipitation. This grade requires at least 10 to 20 hours to begin the precipitation below 900 °C as shown in Figure 2.12 and thus can be allowed to solution anneal below 1000 °C [29]. S32205/S31803 grade (2.5-3.5 wt. % Mo) experiences more propensities towards intermetallic precipitation than the leaner grade S32304 (Mo content is very low). Due to this, higher solution annealing temperature (greater than 1000 °C) should be employed for these steels. SDSSs display the greatest tendency for intermetallic precipitation as these are mostly enriched with Cr, Mo and W. Nonetheless, the severity of precipitation kinetics of these SDSSs can be equivalent to super-austenitic or super-ferritic stainless steels. Problem arises when heavy section components, greater than 60mm thickness are subjected to cooling [40]. Open bore holes accelerate the cooling, particularly in mid-section. Re-dissolution of the precipitates while annealing requires higher temperature for SDSSs than for comparatively leaner standard duplex grades. Similar high temperatures are required for weld joints while solution annealing treatment [41], as consumables tend to contain higher Ni, Si and Mn contents than base materials. The higher Ni-content encourages high austenite contents when annealed and results in enrichment of Cr and Mo in the remaining ferrite. This fact, combined with higher Si and Mn levels, increases the stability of intermetallic phases [29].

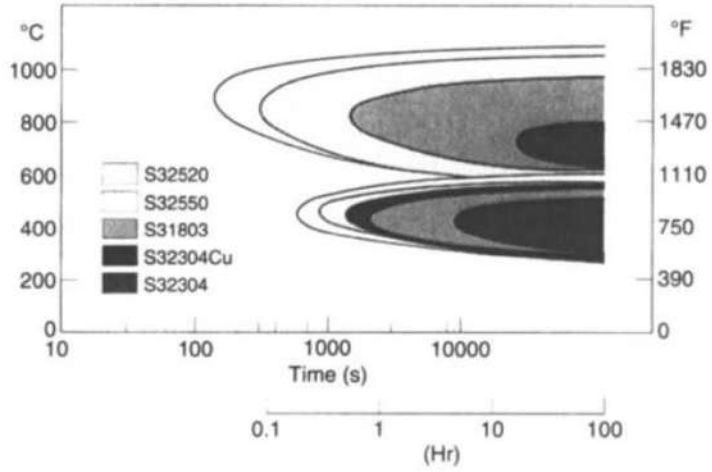

Figure 2.12. TTT diagrams of duplex stainless steels derived by optical metallography between 600 and 1050°C and hardness measurements between 300 and 600°C [23].

2.3.4.3. The 300-600 °C nose.

At this temperature range, the alloy lean grade S32304 is the less sensitive to hardening, and a significant effect is not recorded until about three hours exposure to 400 °C as shown in Figure 2.12. A much shorter time is needed for grades S32205 and S31803, containing Mo, which would appear to accelerate hardening [23].

The 25%Cr and SDSSs show the widest temperature range for hardening and shortest incubation times. This is the result of both the higher Cr and Mo contents and, if present, copper additions [29]. In this temperature range, the formation of α′ or G-phase is possible if the steel is subjected to long-term thermal ageing. Formation of these precipitates is practically impossible in case of lean DSSs. The annealing temperature affects the structure of each phase and the associated corrosion behavior of SDSSs. The results of the precipitation of different phases in SDSSs can be summarized in a TTT diagram. A TTT diagram of the SDSS grade UNS S32750 is shown in Figure 2.13, where the most common precipitates in SDSSs are illustrated [16].

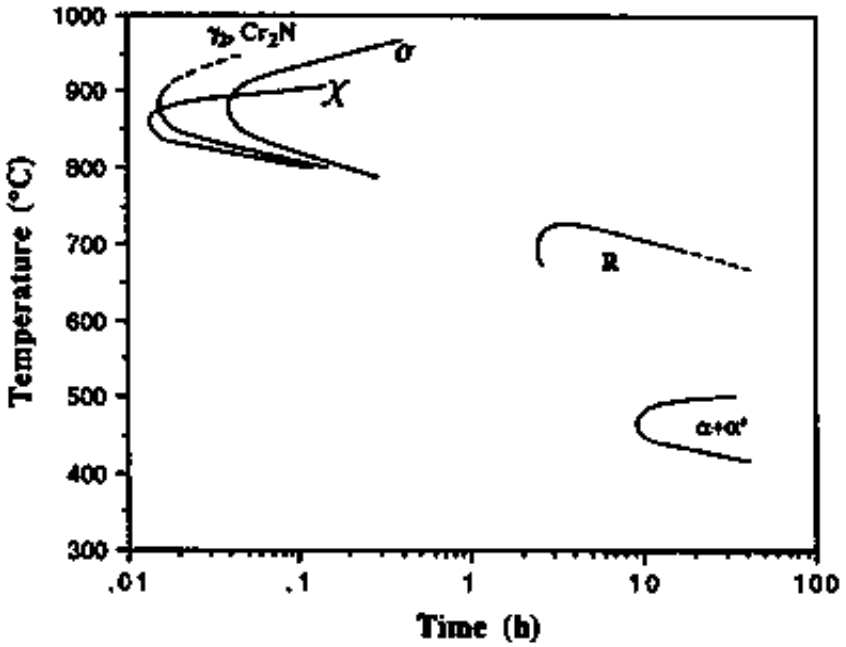

Figure 2.13. TTT diagram of UNS S32750 (SAF 2507), showing the precipitation kinetics of intermetallic precipitates and secondary phases [16].

2.3.5. Intermetallic precipitates and secondary phases.

A variety of undesirable phases may form on solidification of DSSs or during subsequent heat treatment, welding, or ageing during their operational life. The character and morphology of these phases vary markedly, as do the time for them to form and their effect on properties.

2.3.5.1. Sigma phase (σ).

Sigma phase is usually the most important secondary phases since it can be present at the highest volume fractions and clearly devastates the toughness and corrosion properties of DSSs [16].
Sigma is a brittle tetragonal phase richer in Cr and Mo than either the ferrite or austenite matrix around it. It forms preferentially at ferrite-austenite boundaries in the temperature range 600 to 1000 °C in steels with more than about 18% Cr plus Mo. And often starts at triple junctions or grain boundaries (δ/δ or δ/γ) and grows into the adjacent ferrite grains. Its composition is sometimes given as $(CrMo)_{35}$ $(FeNi)_{65}$. It is strongly promoted by Si and suppressed by N.

In unstabilized steels the prior precipitation of carbides destabilizes austenite, leading to subsequent sigma formation. Sigma forms much more rapidly from ferrite than from austenite because of the 100-fold higher diffusion rate of alloy elements in ferrite.

2.3.5.2. Chi phase (χ).

Chi (χ) phase precipitates in the temperature range 700-900°C, and has a similar effect on the material as σ, but occurs mainly at somewhat lower temperatures, where the diffusion is slower. Moreover, χ needs large amount of Mo and less Cr to form and has a cubic structure [16]. This can explain why the precipitated volume fraction of χ is significantly lower compared to σ in commercial DSSs. χ Phase is more unstable than σ phase and might eventually transform into σ phase during aging. The stoichiometry of χ phase is $Fe_{36}Cr_{12}Mo_{10}$, its composition is similar to that of the σ phase, but χ is richer in Mo, so it could be distinguished from σ using electron backscattered diffraction [16]. In addition, in contrast to σ, carbon can dissolve in the χ phase. It also precipitates at δ/γ boundaries and has the same deleterious effects as σ phase [12].

2.3.5.3. Secondary austenite (γ_2).

SDSSs are almost entirely ferritic at temperatures just below solidus, but during cooling, transformation from ferrite to austenite will occur. This type of austenite is termed primary austenite and forms through solid state transformation out of the ferrite, given by $\delta \rightarrow \gamma$.
Secondary austenite or γ_2 can form relatively quickly and by different mechanisms depending on the temperature. Below about 650 °C, γ_2 has a similar composition to the surrounding ferrite, suggesting a diffusion less transformation. At temperatures between 650 and 800 °C where diffusion is more rapid, many Widmanstatten austenite forms can precipitate. In this temperature range, its formation involves diffusion as it is enriched in Ni compared to the ferrite matrix. Even though there is some enrichment of N in γ_2 compared to the ferrite matrix, both Cr and N contents of γ_2 are substantially below that of primary austenite [29]. In the 700-900 °C temperature range, a eutectoid of $\gamma_2 + \sigma$ can form, as γ_2 absorbs Ni and, to some extent, rejects Cr and Mo, encouraging Cr, Mo-rich precipitates, such as σ phase. Similarly, one form of γ_2 which forms at δ/γ boundaries is found to be depleted in Cr, especially if it has co-precipitated with Cr_2N. Either of these diffusion controlled reactions can render the area susceptible to pitting corrosion [29].

2.3.5.4. Laves phase.

The laves or R phase (Fe_2Mo) has the structure A_2B where A is Fe or Cr and B is Mo, Nb, Ti, or Si. It forms at 550 to 650 °C over the course of hours. Thus, although its effect would be deleterious, it seldom becomes a practical problem. It is possible for it to form at temperatures below σ and above alpha prime, but the long times for formation make it rare [12].

2.3.5.5. Carbides.

The type M_7C_3 can precipitate in the temperature range of 950-1050 °C, while $M_{23}C_6$ precipitates below 950 °C [16]. Both types of carbides can form at δ/γ grain boundaries, but precipitation has also been observed at δ/δ and γ/γ boundaries. The carbides have a less important role in SDSSs due to the low carbon content, type 2507 has not revealed carbide precipitates of any type [16].

2.3.5.6. Nitrides.

DSSs are intentionally alloyed with N and contain up to 0.35 wt. % N. At low levels, N can substitute for C in $M_{23}C_6$. At higher N levels, hexagonal Cr_2N can form. This can occur in DSSs if they are heated to a solution annealing temperature about 1040 °C at which the alloy has high solubility for N. Cooling from these temperatures can cause the excess N to precipitate as needles of Cr_2N [16]. Isothermal exposure to the 700-950°C temperature range, produces intergranular Cr_2N at δ/δ grain boundaries as thin plates on subgrain boundaries, triple points, inclusions and along dislocation arrays [29]. Another cubic nitride CrN can form in HAZs of welds [12].

2.3.5.7. Cu-rich epsilon phase (ε).

For steels containing Cu and/or W, other hardening mechanisms can occur. In the case of Cu, the supersaturation of the ferrite due to the decrease in solubility at lower temperatures leads to the precipitation of extremely fine Cu-rich ε phase particles after 100 hours at 500 °C [23], which significantly extend the low temperature hardening range of the DSSs. Although the reported temperature range for their formation varies, it would seem that they all form in the same temperature regime as γ_2 and have been mistaken for such [29].

2.3.5.8. Alpha prime (α΄).

The ferrite phase can decompose into Fe-rich α and a Cr-rich α΄. This can form in a DSS in the temperature range of 300-525°C, and is the main cause of hardening and "475 embrittlement". It is suggested that α΄ formation is a consequence of the miscibility gap in the Fe-Cr system, propose for Williams [6], whereby ferrite undergoes spinodal decomposition [42], into α and α΄ or just outside the spinodal but still within the gap, classical nucleation and growth of α΄ occurs [43]. Alpha prime is often associated with the co-precipitation of Cr_2N in the form of subgrain networks of Cr_2N needles interspersed within a film of α΄ [29]. At temperatures below 400 °C, the Arrhenius equation is often employed to describe the kinetics of embrittlement. The activation energy characteristic of' "475 embrittlement" is similar to Cr-diffusion in ferrite, although other factors influence α΄ formation, such as Cr, Mo and Cu contents and high ferrite levels [29].

2.3.5.9. G phase.

Spinodal decomposition of ferrite in the temperature range of 300–500 °C, precipitation of G phase, it is a silicide with nominal composition $Ti_6Ni_{16}Si_7$ with Mo substituting Ti in DSSs. precipitation of G phase was observed in the ferrite phase of DSSs after long exposures 7500 to 70000 h at 300-500 °C [44]. G-phase develops at α/α′ interfaces, due to enrichment of Ni and Si at these locations [45]. The Table 2.4. Show the phases observed in DSSs.

Table 2.4. Phases observed in duplex stainless steels [29].

Phase	**Chemical formula**	**Formation range °C**	**Lattice type**	**Space group**	**Lattice parameter (A)**	**Preferred location**
Ferrite δ	--- 27.4Cr, 8.7Ni, 4.0Mo	---	BCC	Im3m	*a* = 2.86-2.88	Matrix
alpha prime α′	--- 65Cr, 2.5Ni, 13Mo	300-525	BCC	Im3m	*a* = 2.86-2.88	Intra- δ
G phase	--- 25Cr, 25Ni, 4Mo ≥ 14%Si	300-400	---	---	---	Inter α - α′
Primary austenite γ	--- 26.6Cr. 9.6Ni, 3.3Mo	<1250	FCC	Fm3m	*a* = 3.58-3.62	lntra-δ
Secondary austenite γ_2	Type 1 same as ferrite Type 2 24.3Cr, 11Ni, 3.4Mo Type 3 ---	<650 550-800 700-900	FCC	---	---	lntra-δ δ/γ and δ With σ
Sigma σ	Fe-Cr-Mo Fe35-55, Cr25-40, Mo11-25	600-1000	tetragonal	$P4_2/mnm$	a = 8.79, c = 4.54	Inter δ/γ
Chi χ	$Fe_{36}Cr_{12}Mo_{10}$	700-900	BCC-xMn	143m	a = 8.92	Inter δ/γ
R or Laves	Fe_2Mo	550-650	trigonal	R3	a = 10.903, c = 19.34	δ/γ and δ
Chromium nitrides	Cr_2N CrN	700-950	hexagonal cubic	P31m Fm3m	a = 4.8,c = 4.47 a = 4.13-4.47	lntra-δ
Pi (π)	Fe7MonN4	550-600	cubic	$P4_132$	a = 6.47	lntra-δ
Epsilon (ε)	Cu-rich	not defined	---	---	---	lntra-δ
Tau (τ)	---	550-650	orthorhombic	Fmmm	a=4, b=4.84, c=2.86	---
Carbides	M_7C_3 $M_{23}C_6$	950-1050 550-950	--- FCC	Pnma Fm3m	a=4.52, b=6.99, c=12.11 a=10.56-10.65	Inter δ/γ Inter δ/γ

2.3.6. Physical properties.

DSSs have low thermal expansion coefficients, similar to carbon steels. This reduces the requirement for expansion joints and renders duplex suitable for thermal cycling conditions [23]. The thermal conductivity is higher than for austenitic grades and this, combined with the higher mechanical strength, allows for thinner walled components in many applications, such as pressure vessels and tubing. Finally, as DSSs contain about 50 % ferrite, they show a degree of magnetism, but at an insufficient level to avoid mechanical clamping during machining [29]. The Physical properties of 2507 SDSS are shown in Table 2.5.

Table 2.5. Physical properties of 2507 super duplex stainless steel [11].

Physical Properties in the Annealed Condition

Modulus of Elasticity in Tension

psi	*MPa*
29×10^6	200,000

Thermal Conductivity

Btu/ft/h/°F		*W/m·K*	
68°F	8.2	20°C	14.2

Specific Heat

Btu/lb °F	*kJ/kg·K*
32-212°F	0-100°C
0.11	0.46

Mean Coefficient of Expansion

in/in/°F		*cm/cm/°C*	
68-212°F	7.2×10^{-6}	20-100° C	13.0×10^{-6}
68-752°F	8.1×10^{-6}	20-400° C	14.5×10^{-6}

Electrical Resistivity

Microhm — mm at 68°F (20°C)
850

Density

lb/in³	*kg/m³*
0.28	7,800

Magnetic Permeability

Magnetizable

2.3.7. Mechanical properties.

These properties result from their dual-phase microstructure. They offer high as-annealed strength with good toughness and ductility.

2.3.7.1. Tensile characteristics.

Table 2.6 lists typical and minimum tensile properties for DSS plate, sheet and strip listed in ASTM A2404 and demonstrates that duplex alloys have higher $R_{P0.2}$, and Rm values than most ferritic and austenitic grades. The mechanical properties depend on factors such as the grain size, texture and degree of segregation [29]. The most striking and unexpected characteristic of the duplex grades is their high yield strength, more than double that of comparable austenitic grades. The strength of the duplex grades is driven by the strength of the continuous ferrite phase [12]. It owes its strengthening primarily to:

- Substitutional solid solution hardening by Ni, Mo, Cr, Cu, and Mn.
- Interstitial solid solution hardening by C and N.
- Strengthening by grain refinement due to the presence of two phases.

Because the ferrite phase controls mechanical properties, the dependence of these properties on temperature is significant since flow in BCC structures is thermally activated [12].

Table 2.6. Minimum room temperature tensile properties and maximum hardness of wrought solution annealed stainless steels [46].

	Grades	$R_{p0.2}$ MPa	R_m MPa	A_5 %	Hardness	
					HB	HRC
Ferritic	S40900	205	380	20	179	–
	S44700	415	550	20	223	20
Austenitic	S31603	170	485	40	217	–
	S31254	300	650	35	223	–
Duplex	S31200	450	690	25	293	31
	S31260	485	690	20	290	–
	S31803	450	620	25	293	31
	S32304	400	600	25	290	32
	S32550	550	760	15	302	32
	S32750	550	795	15	310	32
	S32760	550	750	25	270	–
	S32900	485	620	15	269	28
	S32950	485	690	15	293	32

2.3.7.2. Hardness.

The hardness of DSSs has received attention, especially due to the NACE MR-01-75 requirements for sour service [47]. In this standard, the hardness requirement varies between 28 and 34 Rockwell C (HRC) depending on the type. As shown in Table 2.6 the hardness of solution annealed DSSs and SDSSs is generally below these limits, unless subject to cold work or precipitation of intermetallic phases. Thus, as far as meeting the NACE requirements for solution annealed products are concerned, DSSs should not pose a problem. This situation is different for weldments [29].

2.3.7.3. Impact strength.

Toughness is the significant property to be considered when using DSSs to replace the extremely tough austenitic steels. DSSs low-temperature toughness is intermediate to that of ferritic and austenitic steels. This having been said, it should be noted that the DSSs can have excellent toughness levels, such as 100J at –100 °C in the solution-annealed condition [29], as shown in Figure 2.14. As would be expected, toughness improves with decreasing grain size and deteriorates with cold work. The most deleterious effect on toughness comes from the precipitation of intermetallic phases, such as α′ and σ, which cause a sharp decrease in toughness level and a concurrent increase in transition temperature [12]. The exact mechanism of the embrittlement and toughness reduction at temperatures below 500 °C remains still unclear.

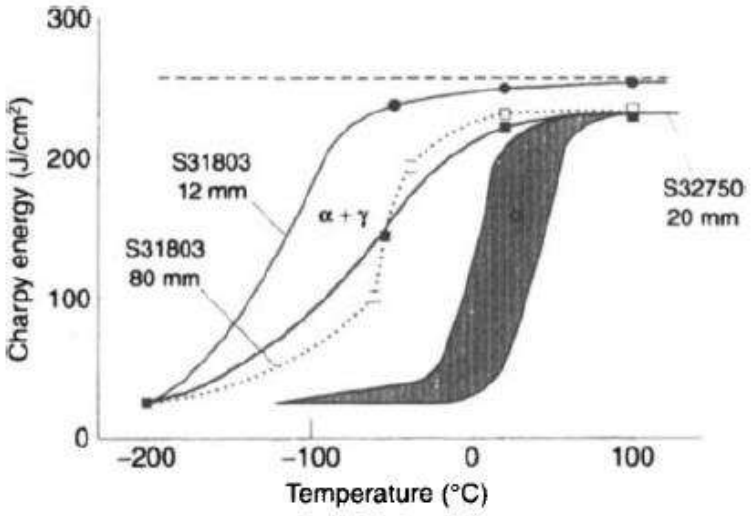

Figure 2.14. Normalized Charpy energy versus temperature measured for several stainless steels [23].

However, it is believed that it is related either to the true spinodal decomposition of the ferrite phase, or to the classical nucleation and growth of α´ phase. Low temperature embrittlement can occur even at temperatures below 300 °C, very long aging times are required. As a consequence, there are limits for the temperature range allowed for the DSS applications. Figure 2.15 shown a TTT diagram for 2507 SDSS with curve corresponds to 27J impact toughness.

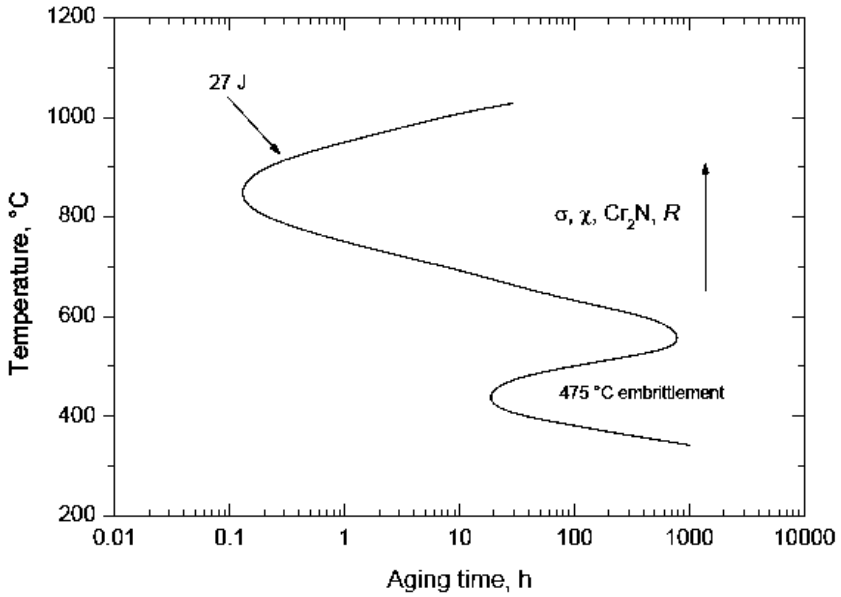

Figure 2.15. Time-temperature-transformation (TTT) diagram for SAF 2507 SDSS. The curve corresponds to 27J impact toughness indicating the rate of embrittlement at different temperature regions [16].

2.3.7.4. Fatigue.

DSSs reveal generally very good properties, better than those of ASSs due to the higher strength of DSSs. Fatigue tests on DSSs indicate that they possess a fatigue limit of about 50% of the yield strength when tested in air [23]. The ratio of the fatigue strength in a hostile environment to that in air is a useful measure of the complementary strong points of the DSSs, that is to say, strength and corrosion resistance. The drop in fatigue strength in a corrosive environment is clearly linked to the intrinsic resistance of the materials to the corrosion mechanisms encountered in the test medium employed. Thus, for sea water, the ratio between the fatigue limit in the corrosive medium and the fatigue limit in air can be correlated with the pitting resistance.

The Figure 2.16 shows that ratio for various alloys plotted versus their PREN. Alloys in Band X indicate that a PREN greater than 40 is necessary to ensure minimum risk of fatigue strength reduction in sea water (ratio = 1), while a PREN of around 32 is desirable to minimize the reduction in fatigue strength. The value of 1 represents the limiting conditions for resistance to pitting corrosion in sea water. It is quite normal that the fatigue limit in the corrosive environment should be reduced when the passive film is damaged by pitting [29].

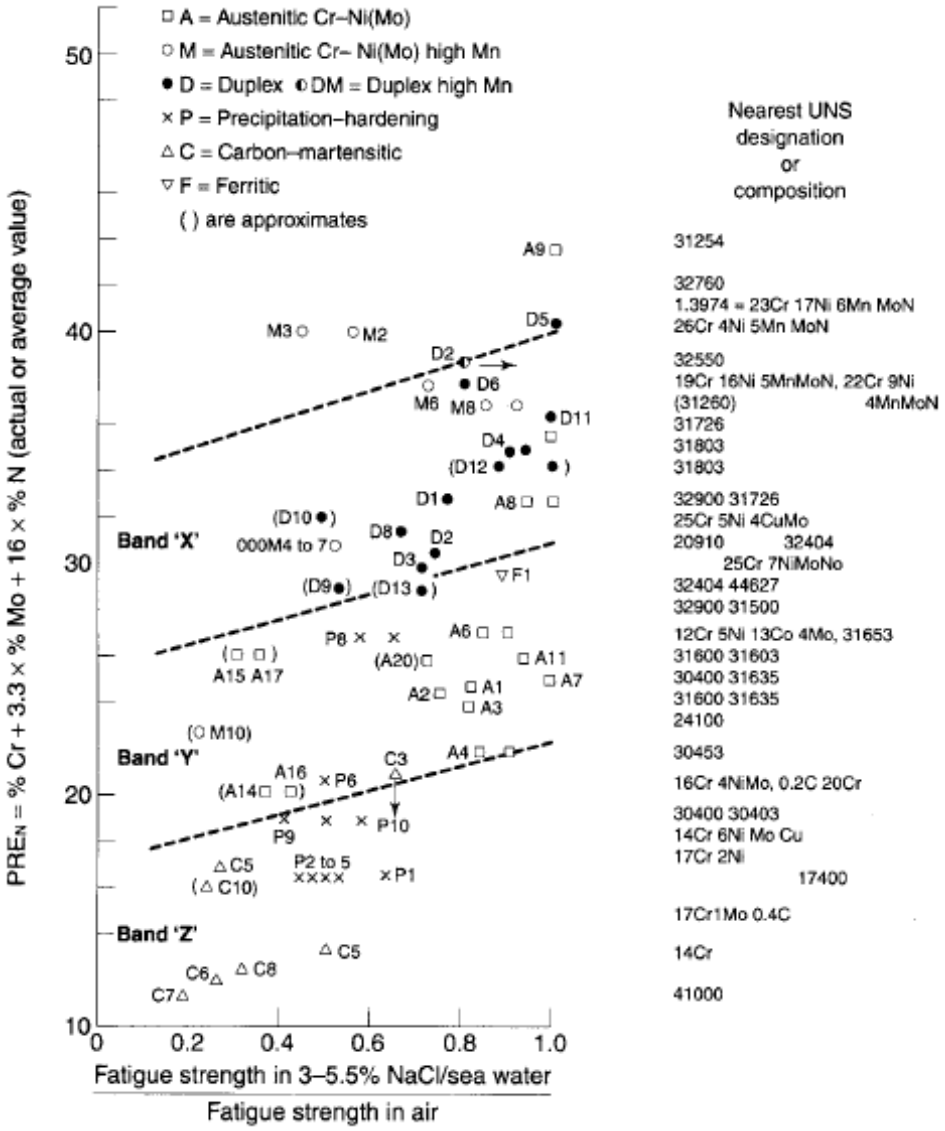

Figure 2.16. Influence of pitting resistance equivalent number (PREN) to fatigue strength in NaCl solution versus in air [29].

As an alloy's resistance to corrosive attack increases, its fatigue limit in a given environment approaches that in air, indicating simply that corrosion plays an increasingly small role in fatigue crack propagation as corrosion resistance increases. While this is intuitively reasonable, it is not diminished because the duplex reward the user with a higher level of yield strength and fatigue strength in air, so the net useful strength under cyclic loading is much greater than that of equivalent-PREN austenitic steels [12].

2.3.8. Corrosion resistance.

The corrosion properties of the DSSs, and of stainless steels in general, are defined mainly by the ability to passivate and to remain in the passive state in the service environment. However, there are fundamental differences in alloy design of duplex and austenitic grades, which leads to significant variations in their corrosion behavior, especially in environments where general corrosion is taking place [29].

Duplex are made up of two phases, ferrite and austenite, each must carry its own weight in resisting corrosion. Early alloys that were lacking in N generally had a ferrite phase that, because of the greater partitioning of the Cr and Mo to the ferrite, had higher corrosion resistance than the austenite. As N is added, it enriches the austenite phase preferentially until the corrosion resistance of the austenite phase reaches that of the ferrite [12].

2.3.8.1. General corrosion.

The DSSs offer important advantages in performance over the austenitic grades in a number of significant aggressive media, including sulfuric acid, hydrochloric acid, sodium hydroxide, phosphoric acid, and organic acids. This performance extends to situations in which the aggressiveness of these media is enhanced by contamination [12].

2.3.8.2. Sulfuric acid.

All duplex grades show lower corrosion rates than 304L and 316L in dilute sulphuric acid. Higher alloy grades are more resistant, with some variation in behavior apparent depending on the degree of aeration. Figure 2.17 show that duplex grades S32304, S31803, S32750 compare well with high alloy austenitic and some Ni-base grades N08904, S31254 and carbon steel. The beneficial effect of copper, as an active alloying element in reducing acids, and duplex with Cu can be used at even higher concentrations and temperatures [29]. In real-life situations, such as seen in flue gas desulfurization, sulfuric acid can be contaminated with chlorides. While this contamination is deadly to 316 and 317, it has only a minor effect on the copper-alloyed duplexes.

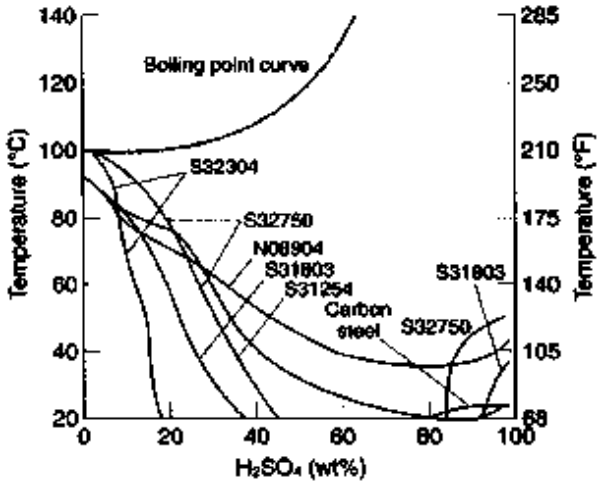

Figure 2.17. Sulphuric acid: 0.1 mm/yr. isocorrosion curves: aerated: S32304, S31803, S32750, S31254, N08940 and carbon steel [29].

2.3.8.3. Hydrochloric acid.

Historically stainless steels have had their poorest performance when confronted by hydrochloric acid, can still be applied at low concentrations. Grade S32205/S31803 offers similar resistance to 316L at low temperatures, although the resistance is better at higher temperatures. Here again, the Cu and W alloyed duplex show exceptionally good performance (S32760) [29], as seen in Figure 2.18. This extends the usefulness of stainless steels to an environment that had previously been off limits. Indeed, the DSSs in general can be said to be relatively indifferent to the pH of chloride solutions and are affected rather by the chloride concentration and temperature [12].

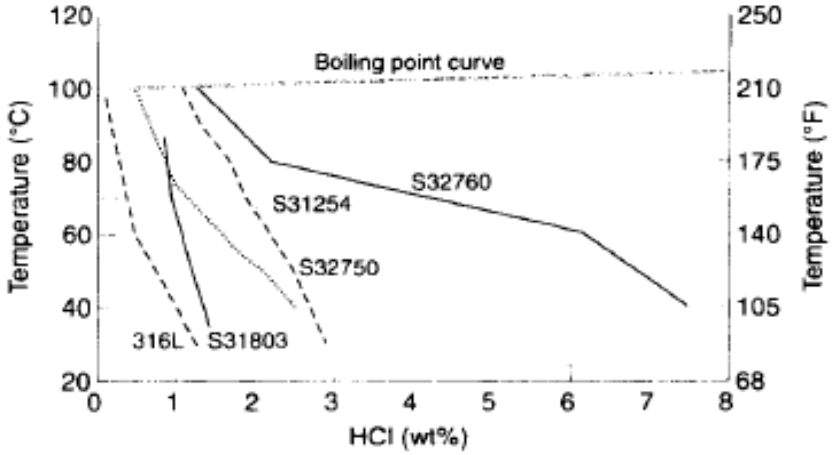

Figure 2.18. Hydrochloric acid: stagnant: 0.1 mm/year iso-corrosion curves [29].

2.3.8.4. Nitric acid.

It is fairly well known and accepted that resistance to nitric acid, which was one of the first uses of stainless steel, depends almost entirely on the Cr content. The DSSs exhibit dramatically different behavior. Mo, in all other instances a very beneficial alloying element, has a strongly negative influence on resistance to this highly oxidizing acid. Consequently, only the leanest-Mo duplex alloys, such as S32304 [29], should be considered for use with nitric acid as shown in Figure 2.19, and even then no advantage can be claimed.

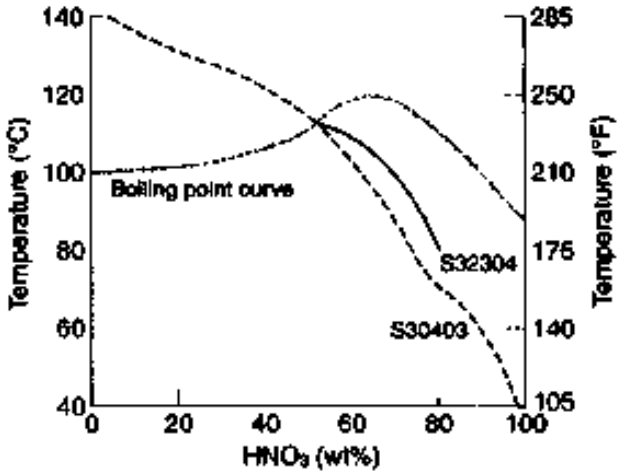

Figure 2.19. Nitric acid: 0.1 mm/year iso-corrosion curves [29].

2.3.8.5. Sodium hydroxide.

Different duplex grades can be applied successfully in caustic environments at low concentrations, < 30 %. Several field studies in the pulp and paper industry have shown that DSSs have much lower corrosion rates than standard austenitic grades in white liquors of Kraft digesters [29]. The behavior of stainless steel has seemed to promote the notion that higher Ni levels were beneficial in strong bases. As shown in Figure 2.20 clearly indicate, that the DSSs with their relatively low Ni levels significantly outperform the higher Ni 304L and 316L, with performance improving with increasing Cr content [12].

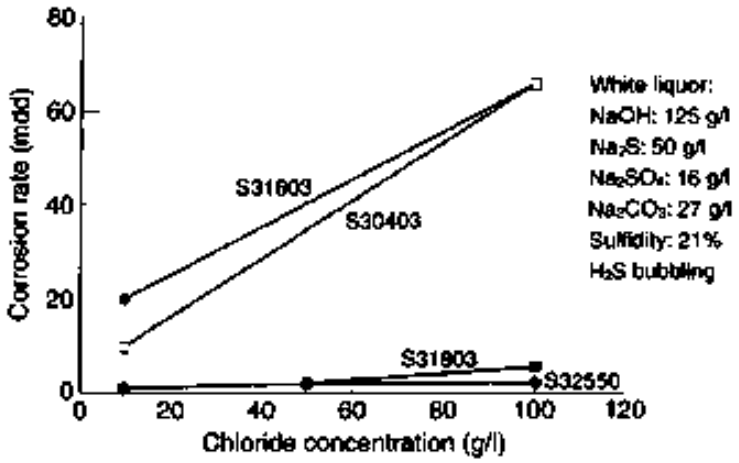

Figure 2.20. White liquors plus chlorides [29].

2.3.8.6. Phosphoric acid.

While pure phosphoric acid is not a very corrosive medium for stainless steel, contaminants in wet process phosphoric acid, such as chlorides and fluorides, can lead to high corrosion rates. Figure 2.21 shows the substantial improvement in performance of the DSSs like S31803 and S32550 over 316L when contaminants are present, as pumps and valves, and in chemical tankers [29]. Performance again improves with increasing Cr, Mo, and N levels.

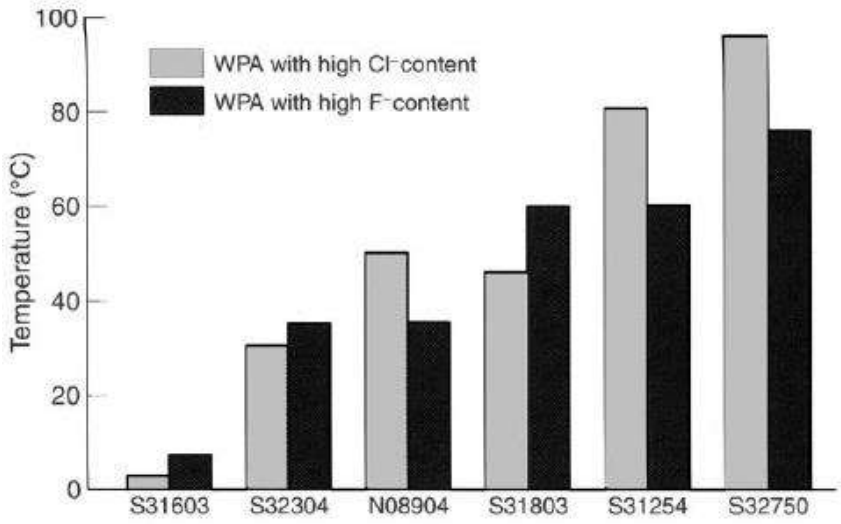

Figure 2.21. Wet phosphoric acid (WPA): minimum temperature for a corrosion rate of 0.127 mm/y [48].

2.3.8.7. Organic acids.

DSSs and, in particular, SDSSs have shown remarkably good passivation properties in pure and contaminated acids, and have an excellent record in industrial plants. SDSSs have been considered as their corrosion resistance, even in boiling 99.7% industrial acetic acid, is excellent (the S32520 grade with Cr, Ni and Cu additions had a corrosion rate lower than 0.02 mm/year). In formic acid, the most aggressive organic acid, S32750 SDSS is resistant at all concentrations almost to the boiling point, outperforming even titanium [48], as shown in Figure 2.22.

In combinations of acetic and formic acid, the superiority of DSSs is quite evident, as shown in Figure 2.23. S32750 SDSS shows virtual immunity, while in mixtures contaminated with halides its performance ranks very closely to expensive Ni-based super alloys such as N06625 and N06455.

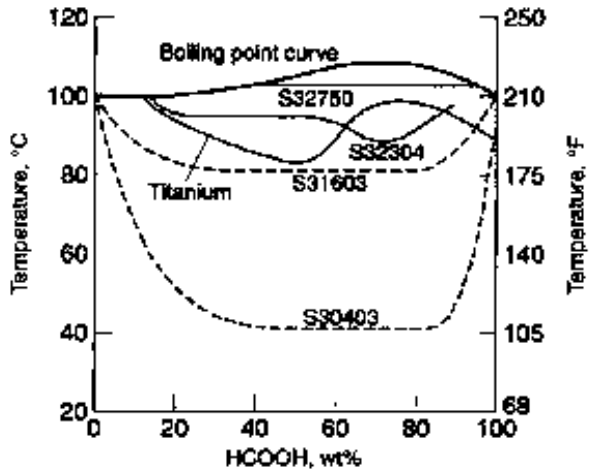

Figure 2.22. Formic acid: 0.1 mm/yr. isocorrosion curves [48].

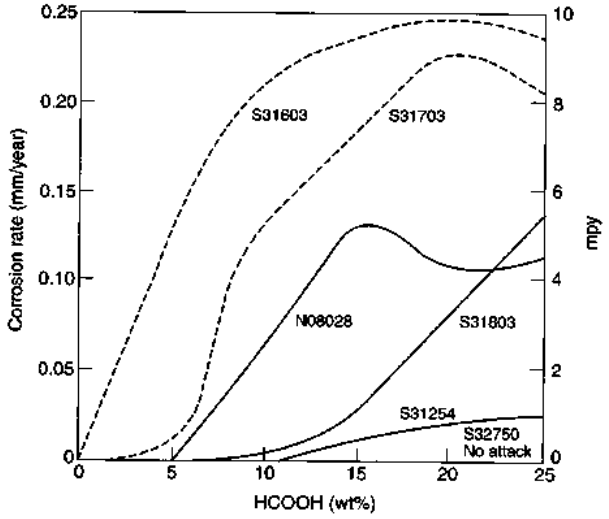

Figure 2.23. Acetic (50%) plus formic acids (and water): boiling [29].

2.3.9. Localized corrosion.

Local corrosion attack most frequently occur in DSS at the austenite/ferrite phase boundaries [16]. In DSS segregation of impurities does not seem to be a probable reason for that, since the steels are extremely pure (e.g., sulfur content can be achieved as low as 0.0015 wt. % or even less). Phase transformations occurring at the grain and phase boundaries may indeed lead to a passivity breakdown.

2.3.9.1. Pitting corrosion.

The alloying elements determining the pitting corrosion properties of the stainless steels are again Cr, Mo, and N. All alloying elements, to varying degrees, affect the pitting resistance of DSSs in chloride environments [29], Table 2.7 list the influence of different alloying additions and microstructure on the pitting and crevice corrosion resistance of DSSs.

Table 2.7. Influence of different alloying additions and microstructure on the pitting and crevice corrosion resistance of DSSs [29].

Alloying	Effect	Reason	Practical limitation
C	Negative	Causes precipitation of chromium carbides with accompanying Cr depleted zones.	About 0.03 % maximum.
Si	Positive	Si stabilises the passive film.	About 2 % maximum, due to its effect on structural stability and on N solubility.
Mn	Negative	Mn-rich sulphides act as initiation sites for pitting. Mn may also destabilize the passive film.	About 2 %. Higher levels might also increase the risk of intermetallic precipitation.
S	Negative	Sulphides, if not Cr- Ti- or Ce-rich, tend to initiate pitting attack.	About 0.003 %, if maximum pitting resistance required. For reasonable machinability, up to 0.02 % allowed.
Cr	Positive	Cr stabilizes the passive film.	Between 25 and 28 % maximum depending on the Mo-content. Higher Cr-content increases the risk of intermetallic precipitation.
Ni	Negative	Increased Ni, other elements constant, dilutes the γ phase with regard to N, which in tum decreases the PRE of the γ phase. If the alloy is very sensitive to precipitation of chromium nitrides, Ni can have a positive effect.	Ni should primarily be used to give the alloy the desired austenite content.
Mo	Positive	Mo stabilizes the passive film, either directly or through enrichment beneath the film.	About 4-5 % maximum depending on the Cr-content. Mo enhances the risk of intermetallic precipitation.
N	Positive	N increases the PRE-number of the γ phase dramatically, not only by increasing the N-content of that phase, but also by increasing the Cr and Mo contents through their partitioning coefficients.	About 0.15 % in Mo-free grades. About 0.3 % in SDSSs and some 0.4% in 25 % Cr, high Mo, high Mn alloys.
Cu	Disputed	Marginal positive or negative effects.	About 2.5% maximum. Higher levels reduces hot workability and undesirable hardenability.
W	Positive	Probably the same as for Mo.	Increases the tendency for intennetallic precipitation.
Ferrite	Positive	Increased ferrite content increases the N, Cr and Mo contents of the γ phase.	Too high ferrite can enhance chromium carbide/nitride precipitation in a coarse microstructure.
Intermetallic phases.	Negative	Precipitates with accompanying depletion of alloying elements (Cr, Mo).	If steel manufacturers recommendations are followed, intermetallic precipitation should not occur during heat treatment or welding.
Chromium carbides and nitrides.	Negative in oxidizing and corrosive chloride containing media.	Precipitation of carbides/nitrides causes Cr-depleted zones which are selectively attacked in certain corrosive media.	In older generations of duplex alloys, nitrides were frequently present in welded joints and in base metal with a coarse microstructure. This has rarely been the reason for a corrosion failure.

Several attempts have been made to establish a mathematical formula describing the relationship between the amount of these elements and the corrosion properties. To determine quantitatively the effects of these elements on the corrosion resistance of stainless steels, pitting resistance equivalent PRE coefficient was introduced. The PRE expressions may be used as an approximate ranking between different wrought stainless steels [29].

Initiation of pitting comprises local breakdown of the surface passive layer and, for DSSs as well as for austenitic steels, the condition of the surface, e.g. grinding, pickling, cold work, dirt, has a more marked influence in chloride environments than in environments where general corrosion takes place. The pitting resistance is further influenced by factors such as the grain size, inclusion distribution and possible precipitation of intermetallic phases [29].

Laboratory data generated in NaCl solutions at + 300 mV saturated calomel electrode (SCE) are provided in Figure 2.24. The ranking order of different duplex and austenitic grades can be obtained from standard laboratory data, in mild conditions. Steels S32205/S31803 is resistant to pitting up to about 80 °C in 1.5 % NaCl (0.90 % Cl) solution, while SDSSs are immune up to the boiling point. On the other hand, in more aggressive media, i.e. higher potential and chloride levels, lower critical pitting temperatures (CPTs) are obtained [29].

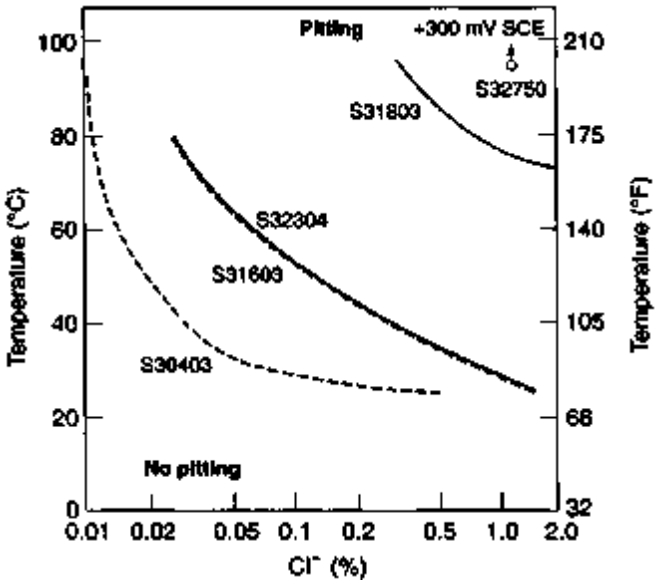

Figure 2.24. CPTs in various NaCl concentration at +300 mV SCE, neutral pH [29].

2.3.9.2. Crevice corrosion.

An alloy's susceptibility to crevice corrosion of stainless steels can be related to the pitting corrosion resistance, as the critical crevice temperatures (CCTs) are roughly proportional to the CPTs, although considerably lower [29]. The difference increases with total alloy content, as can be seen in Figure 2.25. Interestingly, the difference is approximately the same as is the difference in CPT between the wrought alloy and the welded alloy.

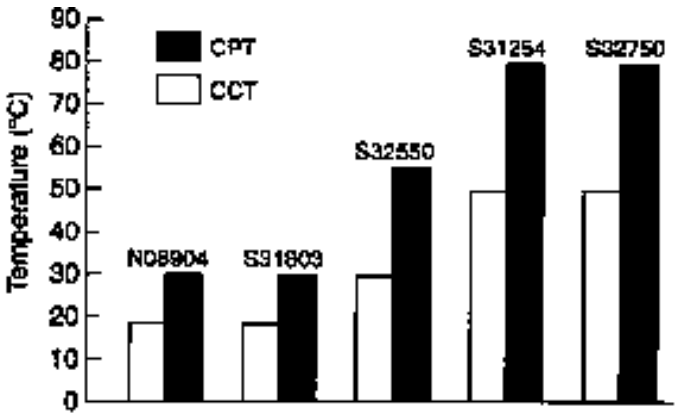

Figure 2.25. CPTs and CCTs in 6% ferric chloride solution, 24 hours [29].

2.3.9.3. Stress corrosion cracking.

SCC is a phenomenon that occurs under the combined influence of an aggressive environment and static mechanical loading. The stress system must include at least one positive (tensile) component. The process takes place often in media, which apparently are minimally corrosive. Furthermore, in most cases it is very difficult to detect cracking before having reached catastrophic proportions. The process is thus extremely dangerous.

One of the most common failure mechanisms in stainless steels is chloride induced stress corrosion cracking (SCC). In particular, the conventional austenitic grades are susceptible to this failure mode. DSSs offer much greater resistance to this form of cracking as shown in Figure 2.26. With all grades being superior to 316L and the SDSSs apparently immune in 3 % NaCl up to 250 °C [34]. Nevertheless, duplex alloys do suffer from SCC given concentrated chloride solutions [29].

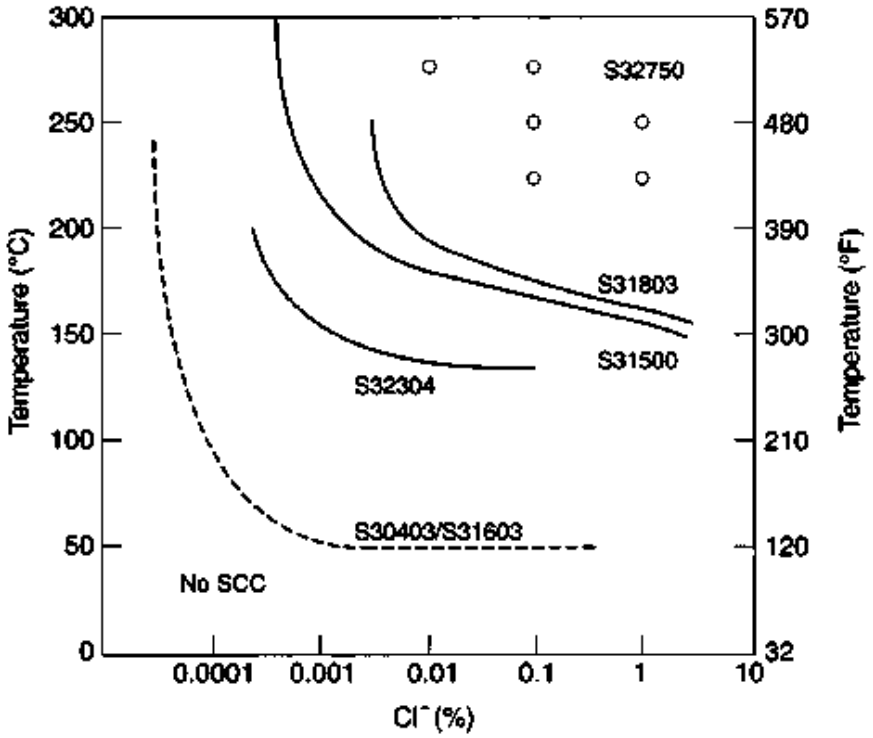

Figure 2.26. Stress corrosion cracking of practical experience and laboratory test data in neutral aerated (~8 ppm) aqueous NaCl environments. Testing time 1000 hours Load ≥ R_p at test temperature [34].

2.4. The 475 °C embrittlement.

Like in ferritic stainless steels, SDSSs are susceptible to the embrittlement phenomenon if they are exposed to a temperature between 280 °C and 500 °C during service. This phenomenon is known as 475 °C embrittlement since the rate of embrittlement is highest at this temperature [4, 49]. This phenomenon was observed first by Reidrich and Loib [50], further investigated by Fisher et al. [51] and Williams [6] and now is well recognized.

William was the first to propose explicitly, the existence of a miscibility gap in the Fe–Cr phase diagram in the temperature range of 280–500 °C as the cause of precipitation of α′ as shown in Figure 2.27. According to this phase diagram 475 °C embrittlement may be expected at temperatures below 516 °C in the composition range of 12–92 at. % Cr in Fe–Cr binary alloy system [6]. It was a confirmation of the earlier study by Reidrich and Loib on the redissolution of α′ precipitate when aged at 550 °C [50].

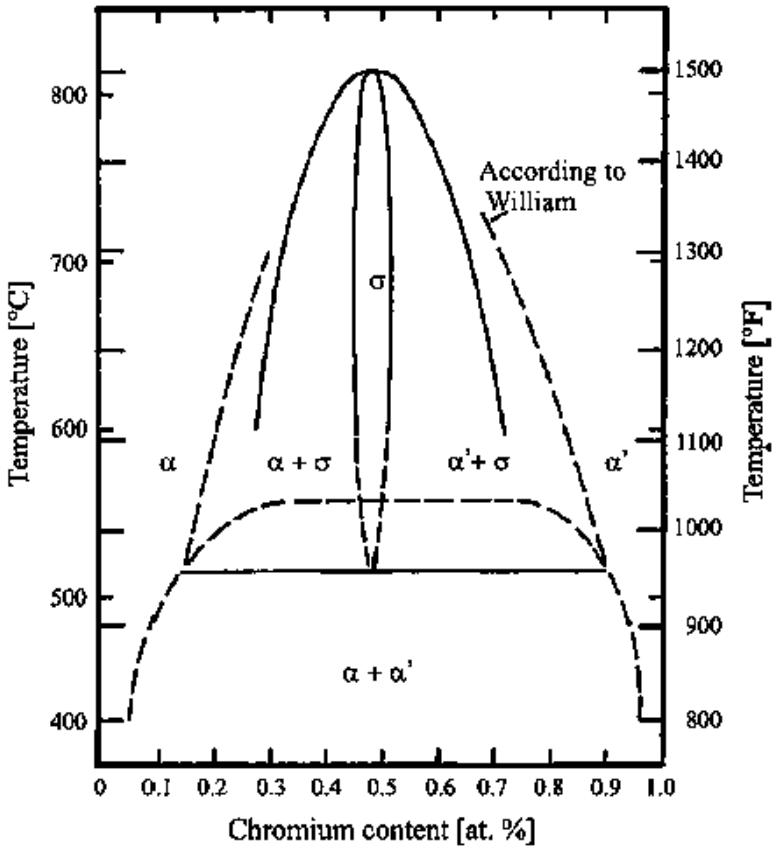

Figure 2.27. Phase diagram of the iron–chromium binary system [6].

According to Cahn [43] and Hillard [8] the phenomenon is characterized by: (a) spinodal decomposition ($\alpha \rightarrow \alpha' + \alpha$) and (b) nucleation and growth of α'. The new phase α' has richer chromium content than the α phase [51, 52]. The term spinodal decomposition refers to a reaction that promotes the formation of two phases that have the same crystal lattice type, but different chemical compositions and physical properties. This is essentially produced by a miscibility gap in the iron–chromium binary alloy system by means of uphill diffusion without nucleation [9, 53].

Studying DSSs via Mössbauer spectroscopy is always difficult as α-austenite is paramagnetic and obscures the detection of paramagnetic α' phase. Solomon and Levinson successfully studied the effects of other alloying elements on 475 °C embrittlement with the help of Mössbauer spectroscopy and transmission electron microscopy in DSSs and seven single-phase ferritic alloys. They showed that Ni promoted the formation of α' whereas Mn, Si and Mo did not influence the formation of α' [52, 54]

Sahu investigated a wrought grade of DSSs and observed needle-shaped precipitate after aging treatment at 475 °C for 100 h in the ferritic grains as shown in Figure 2.28. He identified these precipitates as needles of α′ [55].

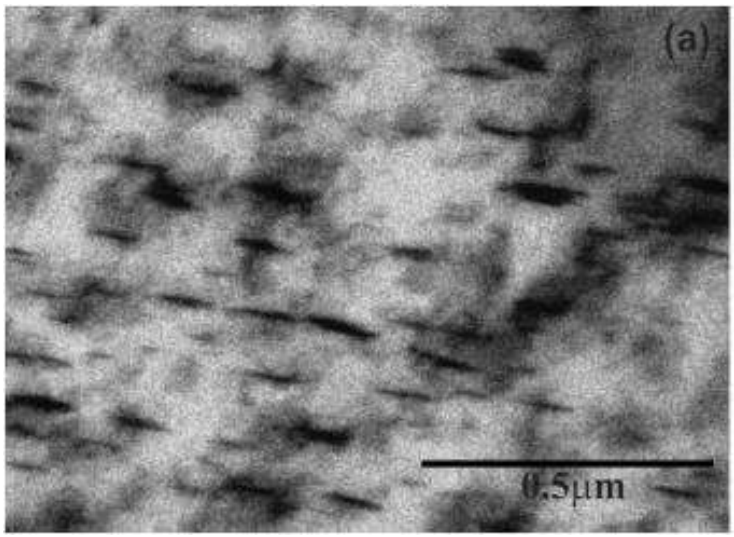

Figure 2.28. Needle like precipitates observed in the ferritic phase of DIN W Nr. 1.4462 grade DSS after aging treatment at 475 °C for 100 h [55].

Weng et al. [56] carried out detailed investigations on the nano-scaled structure of the low-temperature aged specimens of a 2205 wrought alloy with the help of field-emission gun transmission electron microscopy. They noticed the ferritic phase giving a modulated contrast after aging and there is a sudden change to an even contrast in austenitic phase, when observed under TEM. This mottled image with the gradient in contrast, which has the appearance of an orange-peel is shown in Figure 2.29. The modulated microstructure coarsens with the time of aging, maintaining the similar morphology. Fine scale isotropic spinodal decomposition of ferritic phase revealed Cr-rich bright image domains and Fe-rich dark image domains, i.e. α and α′ phases, separately. It also revealed that Mo and Mn were partitioning to the α′ phase, while Ni was partitioning to the α phase [56]

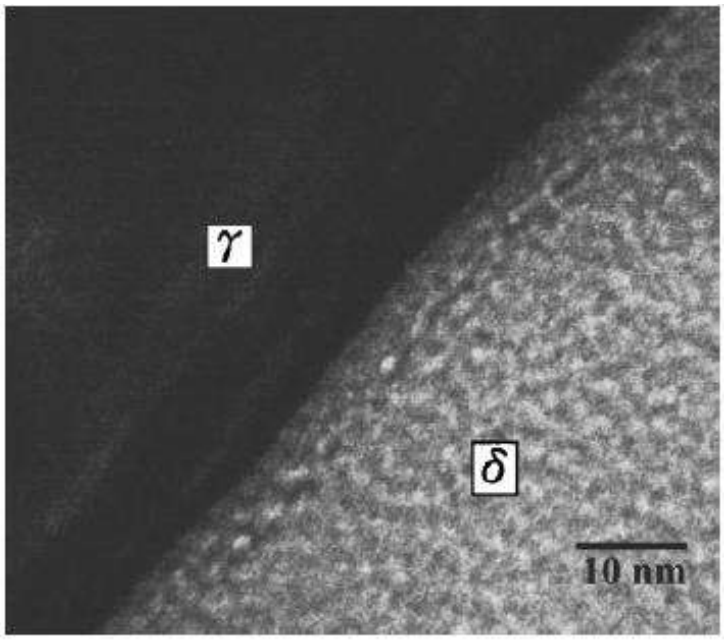

Figure 2.29. Modulated contrast observed in the ferritic phase of 2205 DSS aged at 475 °C for 2 h [56].

Miller and Bentley suggested that the α′ phase forms a typical complex interconnected network structure from the studies conducted by atom probe field ion microscope [44]. Mateo et al. studied the G-phase precipitation in detail in an AISI 329 grade DSS and observed an incubation time from the completion of spinodal decomposition to the nucleation of G-phase. After 200 h aging treatment at 475 °C, they observed very fine spots in TEM right field image. The uniform G-phase particles in the grain body were observed only after 15,000 h of aging at 475 °C. This indicates that the possibility of G-phase precipitation in the ferritic phase requires long duration aging treatment at 475 °C [57].

The kinetics of 475 °C embrittlement have been determined through indirect observations such as changes in certain mechanical properties like hardness [54], impact energy [55] or saturation of certain microscopic features [56]. The kinetics of precipitation plays a very important role for some of the critical engineering components particularly in nuclear power plants.

Miller et al made comparison of the rate of decomposition of the ferrite in Fe–45 wt.% Cr, Fe–45 wt.% Cr–5wt.% Ni alloys and two CF3 grade DSS during long-term aging at 400 °C. According to this group the addition of Ni to the binary Fe–Cr alloy accelerated the kinetics of decomposition and significantly increased the hardness of the alloy as shown in Figure 2.30. Although the hardness data from the ternary alloys are similar to those of the ferritic phase in the DSS, they observed significant differences in the scale and composition amplitudes of α and α′ phases. It is evident that the kinetics of precipitation plays an important role in the deterioration of mechanical properties. The composition also plays a key role in determining the kinetics of precipitation [54].

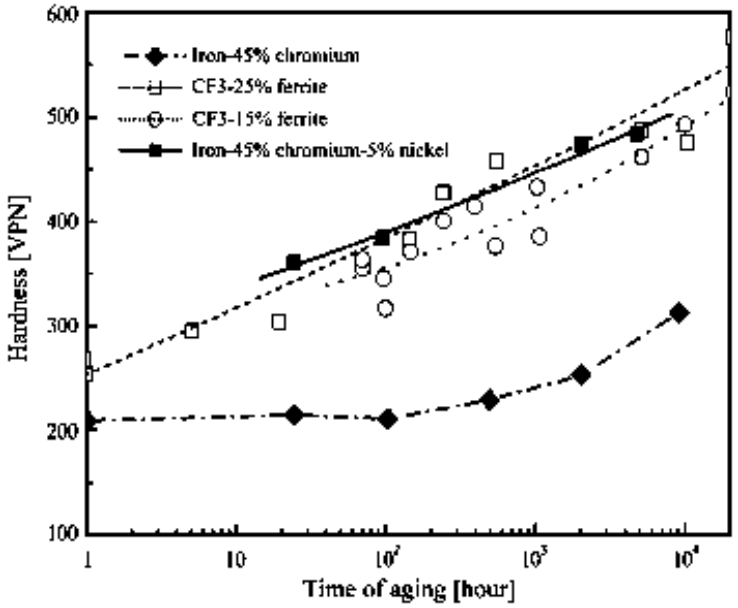

Figure 2.30. Hardness of the Fe–45% Cr–5% Ni, Fe–45% Cr alloys and the ferrite phase in two CF3 stainless steels as a function of aging time at 400 °C [54].

Sahu observed that the deterioration of impact energy for the DINWNr 1.4462 grade DSS fit into a sigmoidal shape when plotted on a semi-log scale with time of aging at 475 °C as shown in Figure 2.31. He obtained a value of 8 J for 100, 200 and 300 h of aging treatment and concluded that the embrittlement reaches saturation in 100 h for the investigated grade [55].

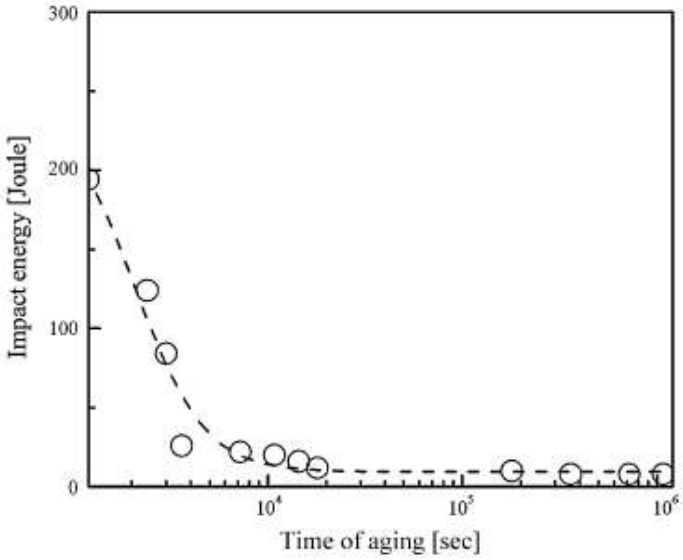

Figure 2.31. Variation of impact energy with time of aging at 475°C for the DINWNr1.4462 grade DSS[55].

Grobner reported that in the temperature range of 371–482 °C Fe–Cr alloy with 18 at.% Cr embrittled in times as short as 2 h, whereas with 14 at.% Cr embrittlement was observed after longer exposure time. This is a clear indication of the sensitivity of this embrittlement to alloy composition. According to Grobner interstitial element accelerated the embrittlement caused by precipitation of phase on dislocation whereas substitutional alloying elements such as Mo and Ti did not substantially affect the kinetics of embrittlement [4].

The distribution of ferritic phase in the matrix, their grain size and grain shape play a very important role in determining the degree of embrittlement. As only the ferritic phase is embrittled during aging at 475 °C, the degradation in material properties directly depends on the amount and morphology of the ferritic phase. It has been established that 475 °C embrittlement is a major concern only when the volume fraction of the ferrite exceeds approximately 15–20%.

With the demand for efficiency improvement of energy generation processes, the components and systems are required to operate at higher temperatures, which can potentially compromise the structural integrity of SDSSs due to the 475 °C thermal embrittlement. For decades, different techniques such as the Mössbauer spectroscopy and TEM have been used to the transformation of ferrite phase in these materials. The paramagnetic characteristic of the austenite phase makes the Mössbauer spectroscopy difficult to use. TEM analysis is capable of detecting the precipitation of nanoparticles, but its use is limited to a laboratory environment.

2.5. Ultrasonic properties

2.5.1. Longitudinal and shear wave velocity.

In materials characterization, NDE methods have been used to study different types of damage in metallic materials. Using ultrasonic wave velocity measurements found that the longitudinal velocity is sensitive and could detect phase transformations. Ruiz et al. [58] investigated the thermal effect on DSS using ultrasonic attenuation and shear wave velocity measurements. Their results indicate that the measured high frequency attenuation can predict thermal degradation after 30 min holding time at 700 °C.

2.5.2. Nonlinear ultrasound.

In recent years, nonlinear ultrasonic techniques have shown their effectiveness to nondestructively detect the degradation in the microstructure of metallic materials caused by different mechanical and thermomechanical phenomena. These microstructural changes may affect the mechanical response of critical components, and therefore, the detection of the onset of the damage or microstructural change could help prevent unforeseen failures of such components and possibly extend their service life. Two nonlinear effects of practical importance to detect the material nonlinearity are exploited in this research for characterizing the α'phase precipitation in SDSSs. The first one is the stress dependence of the ultrasonic velocity, also called the acoustoelastic effect [59]. The second order acoustoelastic coefficient has been shown to be more sensitive to early fatigue damage than the linear ultrasonic parameters [60]. The second effect is the second harmonic generation in propagating ultrasound as a result of its interactions with the microstructure of material that might have been changed by the precipitation of second phases [58, 61], fatigue damage [60, 62, 63], stress corrosion cracking [64, 65], and creep damage [66]. Recently, the use of Rayleigh surface waves has shown their potential to detect high temperature material damage caused by the precipitation carbides in ferritic-martensitic steels [61] and the precipitation of sigma phase [58].

From the NDE point of view, the use of nonlinear Rayleigh waves has a main advantage that access to only one side of the specimen and/or structures is needed to perform the test, therefore, being more suitable to on-site applications.

2.5.2.1. Nonlinear Rayleigh waves: nonlinearity parameter.

The nonlinearity parameter for the second harmonic generation in Rayleigh surface waves is written as:

$$\beta_R = \frac{8u_2}{\omega^2 x_1 u_1^2} \frac{c_l \sqrt{c_l^2 - c_R^2}}{2\left(c_s / c_R\right)^2 - 1} \tag{2.5}$$

where x_1 is the propagation distance, u_1 and u_2 are the out-of-plane displacement amplitudes of the fundamental and second-order harmonics, respectively, c_l, c_s and c_R are the longitudinal, shear and Rayleigh wave speeds in the solid, and ω is the fundamental angular frequency. In the measurements, the fundamental frequency is maintained constant, while the propagation distance is varied. The signal amplitudes of the fundamental (A_1) and second harmonic (A_2), which are proportional to u_1 and $u_2$in Eq. (2.5), are measured at numerous spots along the acoustic axis and then A_2 / A_1^2 as a function of propagation distance is plotted. In this case, we define a relative nonlinearity parameter which is proportional to the absolute parameter in Eq. (2.5):

$$\beta_R = \frac{A_2}{x_1 A_1^2} \tag{2.6}$$

With this approach, it is possible to isolate the material nonlinearity from other nonlinear effects [61]. There are two different second harmonic signals propagating together: one due to the material nonlinearity and the other from the electronic devices and transducers. The second harmonic due to the material nonlinearity grows cumulatively over the distance because the fundamental wave keeps interacting with the material and generating the second harmonic.

The instrumentation nonlinearity, once introduced into the material, propagates following the linear diffraction law for this frequency, and will have a decreasing amplitude. At a location relatively far from the source, the measured second harmonic wave will be mostly due to the material nonlinearity, and the effects of other nonlinear sources are minimal. Note that using this approach does not measure an absolute nonlinearity parameter; in order to do this, the diffraction effects on the fundamental and second harmonic waves would need to be corrected for as shown in [67].

2.5.2.2 Acoustoelasticity.

The acoustoelasticity effect is the change of the ultrasonic velocity in a material subjected to stresses. The dependence of ultrasonic velocity on the stress is written as:

$$c(\sigma_{rem}) = c_0 + K_1\sigma_{rem} + K_2\sigma_{rem} \tag{2.7}$$

where c_0 is the wave velocity without a remote stress (σ_{rem}) and K_i is the ith order acoustoelastic coefficient. The second order acoustoelastic coefficient has been shown to be especially sensitive to fatigue damage in adhesive joints and plastic materials [68] and to thermally induced residual stress in metal matrix composites [69].

The theory of finite-deformation elasticity introduces three independent constants, denoted as third-order elastic constants (TOEC), to describe the nonlinear stress-strain behavior in an isotropic material. The strain energy density (U) is written as follows:

$$U = \frac{1}{2!}c_{ijkl}\varepsilon_{ij}\varepsilon_{kl} + \frac{1}{3!}c_{ijklmn}\varepsilon_{ij}\varepsilon_{kl}\varepsilon_{mn} + \cdots, \tag{2.8}$$

where c_{ijkl} and c_{ijklmn} are the second and third order elastic constants with ε_{ij} is the Lagrangian strain. Different sets of independent TOECs have been proposed by various authors, including A, B and C used by Landau and Lifshitz [70], which are a linear combination of the Murnaghan constants, l, m and n [71]. The nonlinear elastic behavior manifests itself through variations in ultrasonic wave velocity with applied stress (or strain). Hughes and Kelly [72] derived equations that relate acoustoelastic coefficients to the Lamé and the Murnaghan coefficients.

Therefore by measuring the velocities of ultrasonic waves with different polarizations at unstrained and strained states, all three TOECs can be determined. To do this, three independent acoustoelastic measurements were taken in this research to experimentally obtain the acoustoelastic constants and from them. The three Murnaghan coefficients (*l*, *m*, and *n*) are obtained by inverting Hughes and Kelly equations to get:

$$\begin{aligned} l &= (3\lambda + 2\mu)(\lambda + 2\mu)K_{d,n} + 4\lambda(\lambda + \mu)K_{s,np} + 2\lambda^2 K_{s,nn} + \frac{\lambda^2}{\mu} \\ m &= \mu\left[4(\lambda + \mu)K_{s,np} + 2\lambda K_{s,nn} - 2\right] \\ n &= 4\mu\left[2\mu(K_{s,np} - K_{s,nn}) - 1\right] \end{aligned} \tag{2.9}$$

where λ and μ are the Lamé constants, $K_{d,n}$ is the acoustoelastic constants of the longitudinal wave (*d*) propagating normal (*n*) to the applied uniaxial tensile stress, $K_{s,np}$ and $K_{s,nn}$ are the acoustoelastic constants for a shear wave propagating normal to the applied stress with polarization parallel (*p*) and normal (*n*) to the applied stress. Using the independent TOEC *A*, *B*, and *C* by Landau and Lifshitz [73] and the Murnaghan constants as: $l = B + C$, $m = (A + 2B)$ and $n = A$, the standard form of the third-order elastic constants (C_{111}, C_{112}, C_{144} and C_{166}) are obtained:

$$\begin{aligned} C_{111} &= 2A + 6B + 2C = 2(l + 2m) \\ C_{112} &= 2B + 2C = 2l \\ C_{144} &= B = \frac{2m - n}{2} \\ C_{166} &= \frac{1}{2}A + B = m \end{aligned} \tag{2.10}$$

In addition, two second-order elastic coefficients (C_{11} and C_{44}) are calculated from longitudinal and shear ultrasonic velocity data that were obtained from separate measurements. Then the material nonlinearity parameter is calculated using these calculated second- and third-order elastic constants [74]:

$$\beta_\sigma = \left(3 + \frac{C_{111}}{C_{11}}\right) \tag{2.11}$$

2.5.3. Ultrasonic attenuation.

Ultrasonic techniques are extensively used because of their capabilities to detect and size internal flaws and to characterize materials' microstructures. Different efforts have been made in recent years to relate changes in the microstructure characteristics to ultrasonic variables such as the wave velocity, the attenuation, and the acoustic nonlinearity.

The effect of the material microstructure on a propagating ultrasonic wave is related to a scattering phenomenon that causes a loss of the ultrasonic signal; this loss is mainly caused at the grain boundaries due to the slight impedance mismatch at the grain boundaries. This is known as scattering-induced attenuation of the ultrasonic wave. If this loss is measured it can be used to nondestructively characterize the microstructure of polycrystalline materials.

Scattering induced loss (L_S) is not the only component of the total loss (L_T) that is measured from an ultrasonic experiment such as the pulse-echo technique; where L_T includes two more sources of loss i.e., I) beam diffraction loss (L_D) and II) absorption loss (L_A); therefore the total loss can be expressed as follows:

$$L_T = L_S + L_D + L_A \tag{2.12}$$

The beam diffraction loss is caused by the geometry of the transducer and transducer-sample distance and can be determined experimentally or analytically using Rogers and van Buren expression [75]:

$$D(\omega) = 1 - e^{-i2\pi/s}[J_0(2\pi/s) + iJ_1(2\pi/s)] \tag{2.13}$$

where $s = 2\pi z/ka^2$ with k ($=2\pi/\lambda$) being the wavenumber, a the transducer radius, z the propagation distance, and J_0 and J_1 are the first kind Bessel functions of order 0 and 1, respectively. On the other hand, the absorption loss in metallic polycrystalline materials can be neglected.

In the low frequency range, the scattering induced attenuation can be described by the Rayleigh scattering where the wavelength (λ) is much larger than the grain size diameter (D). Therefore, the attenuation coefficient is proportional to fourth power of the frequency (f) can be denoted by [76]:

$$\alpha_R = \Delta D^3 f^4 \tag{2.14}$$

The attenuation in this case is primarily due to the scattering of propagating waves at grain boundaries, the level of which will depend on the wave propagation direction with respect to the crystallographic orientations of grains [77]. Measurement of attenuation due to the grain scattering presents real difficulties, especially in anisotropic materials [78, 79]. Ahmed et al. [77] calculated the attenuation coefficient numerically on randomly oriented grains in an aluminum and aligned grains in a stainless steel. They concluded that the attenuation is controlled by grain volume. Welding also produces complex microstructural regions with different acoustic properties that could complicate residual stress assessment [80].

Saniie et al. [81] measured the backscattered signal that consists of multiple interfering echoes, finding that the attenuation coefficient is position dependent. In the literature, authors used this approach to investigate microstructure characteristics of different materials [82-84]. Several models have been proposed to study the scattering-induced attenuation of the ultrasonic wave [85, 86]. Since the grain size has an important parameter that influences many mechanical properties, a quantitative characterization of grain size would be very useful, Ruiz et al. [87], used ultrasonic c-scan imaging to characterize welded joints of 2101 lean duplex stainless steel. The experimental results showed that the attenuation coefficient of the longitudinal waves is sensitive to gradual microstructure changes produced by the deposition of multiple weld beads.

In this study, the changes of the ultrasonic attenuation coefficient caused by low temperature embrittlement are investigated and high frequency c-scan attenuation coefficient images show a clear difference between undamaged and damaged samples of 2507 SDSS. The degradation was tracked with microhardness measurements and validated by SEM and TEM observations.

2.6. Electric conductivity measurements using alternating current potential drop (ACPD).

For decades, various electromagnetic methods such as the thermoelectric power, eddy current technique and ACPD technique have been used for nondestructive evaluation (NDE) of materials. The potential drop or potential difference nondestructive technique relies on the measurement of electric voltage (potential drop) throughout the surface of a metallic material in which an electric current passes. This measurement is a function of the electrical resistance between the measuring points. If the electrical resistance is measured, the specimen´s electric conductivity, can be determined. The measurement of the resistance can be affected by the permeability which depends on the working frequency, probe geometry and probe dimensions. Alternating current potential drop (ACPD) has gained wide acceptance in the NDE community since it is a reliable, low cost electric conductivity measurement method. The ACPD has been used to evaluate microstructural changes by measuring conductivity and permeability of materials [88-91] and to measure the length and the depth of surface-breaking cracks [89, 92, 93]. Recently, finite element calculations showed that modifying the geometry of the modeled test sample allows an accurate prediction of the results of ACPD [94].

A novel directional four point ACPD probe was developed and used to monitor creep damage [95], and further investigated by Prajapati et al. [96] for creep detection in the vicinity of welds. In their experiments, one pair of electrodes injects electric current into the sample and a second pair of electrodes measures the resulting voltage difference at the electrodes' locations. In ACPD inspections, the injected current is limited to a penetration depth beneath the surface, and the depth can be controlled by the inspection frequency as follows:

$$\delta = \frac{1}{\sqrt{\pi \mu \sigma f}} \tag{2.15}$$

Here, μ is the magnetic permeability, σ is the electric conductivity of the material and f is the frequency of the injected current. Compared to direct current potential drop (DCPD), Hwang [97] indicated that ACPD has the advantage that the same injection current produces much larger potential differences. Among other benefits of using ACPD are: the elimination of thermoelectric effect, enhanced common mode rejection ratio, impedance matching and ground loop elimination by transformer coupling, and higher signal to noise ratio [96].

2.7. Thermoelectric conductivity measurements.

The Seebeck coefficient (also known as thermoelectric power or TEP), S, is a temperature dependent electronic property of a metallic material that can be described as the entropy of the free electrons in the alloy. Several factors control the Seebeck coefficient, which includes: electron concentration, effective mass of the electrons and electronic scattering behavior in an alloy [98]. All these factors are influenced by the solute content, lattice strain, microstructural changes, material processing and time-dependent phase changes. All this can be exploited for nondestructive evaluation (NDE) and materials characterization. All existing thermoelectric NDE methods are based on the well-known Seebeck effect that is commonly used in thermocouples to measure temperature at a junction between two different conductors. The Seebeck coefficient of metals is affected by diverse material properties. Chemical composition exerts the strongest effect on the thermoelectric properties; therefore, one of the main applications of materials characterization by thermoelectric means is metal sorting [99].

However, it is also known that during fabrication processes, materials with identical chemical composition can also create an efficient thermocouple, and this characteristic can be further exploited for NDE of materials [100, 101]. Also, TEP has been successfully applied to follow the precipitation of molybdenum in secondary hardening steel [102], as well as to measure the effects of sigma phase precipitation in 2205 DSS [91].

This research was conducted to investigate the possibility of using TEP measurements as a rapid and reliable NDE technique to assess the 475 °C embrittlement of 2507 SDSS caused by the precipitation of α´ Cr-rich phase in this material.

CHAPTER III. EXPERIMENTAL METHODOLOGY

3.1. Sample preparation.

A 12.7 mm thick UNS S32750 DSS plate with the chemical composition given in Table 3.1 and a Pitting Resistance Equivalent Number of 42 was used in this study. Six samples were obtained from the plate; each has dimensions 180 × 50 × 12.7 mm^3, the rolling direction (previously established using shear wave birefringence) coincides with the longest dimension. Embrittlement treatments on the samples were conducted at 475 °C for holding periods of 10 minutes, 0.5, 1, 10, 50, 100, 300 and 500 h, respectively, followed by water quenching.

Table 3.1. Chemical composition of 2507 SDSS in wt. %.

C	Cr	Ni	Mo	Fe	Cu	Si	Co	Mn	N	P	Nb	S
0.017	25.37	7.09	3.87	61.306	0.24	0.32	0.012	0.82	0.28	0.24	0.015	0.001

3.2. Electric conductivity measurements on thermally embrittled 2507 SDSS.

The effect of 475 °C embrittlement on the corrosion behavior of 2507 super duplex stainless steel (SDSS) was investigated using the double loop electrochemical potentiokinetic reactivation (DL-EPR) test to determine localized corrosion susceptibility, the potentiostatic polarization to determine the critical pitting temperature (CPT) and precise electric conductivity measurements using a recently developed alternating current potential drop (ACPD) probe. Electric conductivity measurements show substantial changes with aging time, which have reasonable correlation with the electrochemical and microhardness measurements. Scanning electron microscopy (SEM) analysis of the fracture surfaces and Charpy impact tests applied to the aged samples provided direct evidence of gradual embrittlement. This research, therefore, demonstrates the feasibility of using the ACPD as a reliable alternative for laboratory and in-situ applications to determine 475°C embrittlement.

The aim of this research is to investigate the sensitivity of ACPD technique as a nondestructive method to monitor the susceptibility of a commercial AISI 2507 SDSS undergoing localized

corrosion caused by the spinodal decomposition of the δ ferrite phase, consisting of Cr-enriched α´ and Fe-rich α phases due to so-called 475 °C embrittlement. The ACPD measurements were associated with the microstructure changes that were analyzed by means of scanning electron microscopy (SEM). The effect of the aging time on the mechanical properties was evaluated using Vickers microhardness measurements and Charpy impact test.

The effect of the 475 °C embrittlement on the resistance to localized corrosion of AISI 2507 DSS aged for different periods was assessed by the CPT and DL-EPR measurements. Both methods provided results that are in agreement with the ACPD measurements. Figure 3.1(a) shows a square-electrode ACPD probe used to measure the electric resistance of the embrittled samples. This probe has four spring-loaded heavy-duty needle-shaped pins with 4 mm separations that are mounted in a Plexiglas fixture. This research uses a low frequency ACPD to measure the electric resistance in the *x* direction at the same location as shown in Figure 3.1(b). The transfer resistance $R_1=V_1/I_1$ is obtained by injecting current I_1 at electrodes A_1–A_2 and measuring the resulting in-phase voltage drop V_1 between electrodes C_1–C_2. The spring-loaded electrodes would guarantee that the average electrode separation *a* remains constant and independent between measurements.

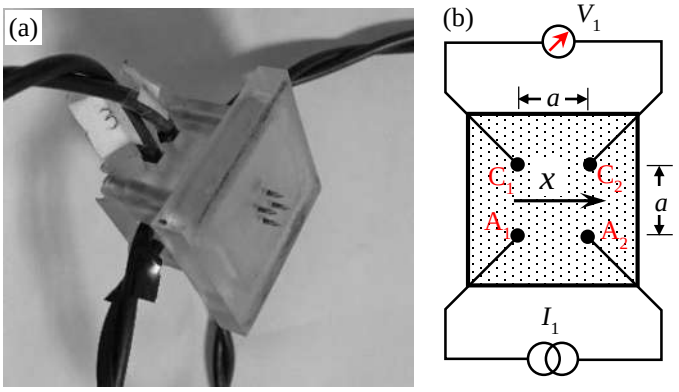

Figure 3.1. (a) A picture of the deployable ACPD probe and (b) schematic diagram of ACPD measurements in the *x* direction.

Because of this, the probe is not sensitive to geometrical effects and can be used selectively to detect material changes only. The measured resistance (R_1) is related to the electric conductivity (σ) and electrode separation (*a*) by:

$$R_1 = \frac{1}{\sigma \pi a}\left(1 - \frac{1}{\sqrt{2}}\right) \tag{3.1}$$

It is worth noting that the electric conductivity is the inverse of the electric resistivity (ρ). In all experiments, the injection current (*I*), inspection frequency (*f*), and electrode separation (*a*) were kept constant at 10 mA, 3 Hz, and 4 mm, respectively.

3.3. Longitudinal and shear wave ultrasonic velocity measurements.

For the linear and nonlinear ultrasound measurements all the specimens were carefully ground to grade 1200 emery paper. The shear wave velocity was measured the specimens. Figure 3.2 shows a schematic diagram of the experimental setup used for shear wave birefringence measurements. Were a 5 MHz normal incidence shear wave transducer was placed on the specimen and excited by a Panametrics 5073PR broadband pulser/receiver. The ultrasonic signal was digitized and averaged by a LeCroy HDO 4034 oscilloscope, and the time of flight of two consecutive back wall echoes was measured at different positions on each samples. For accurate time measurement, we choose to measure the corresponding positive zero-crossings of the RF signals, the shear wave velocity was measured for the fast and slow shear wave modes propagating in the thickness direction (*d*) with polarization in the rolling direction (length direction, *l*) and the slow mode with polarization in the normal to rolling direction (width direction, *w*). The velocity of the shear wave was determined using the method described by in [103]:

$$c_{m,n} = \frac{2d}{t_{m,n}} \tag{3.2}$$

Where $c_{m,n}$ is the shear wave velocity, the sub index *m* and *n* indicates the propagation direction and the polarization direction respectively, *d* is the thickness of the specimen, and $t_{m,n}$ is the two-way propagation time.

The longitudinal velocity was determined using the same approach but using the immersion technique as shown in Figure 3.3(a).

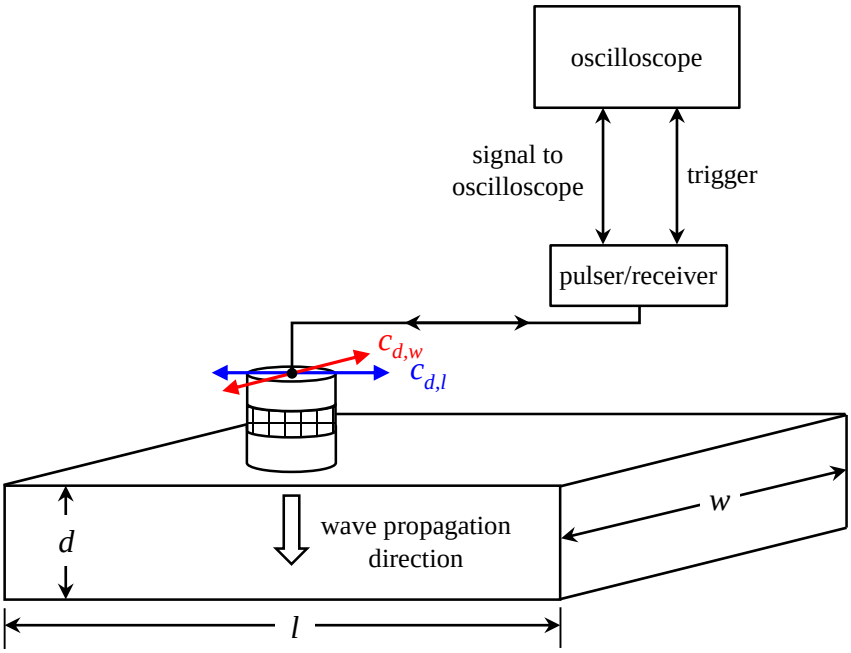

Figure 3.2. Schematic representation of pulse-echo method to measure the shear wave velocity measurements.

3.4. Ultrasonic attenuation measurements.

The attenuation coefficients of untreated and embrittled specimens are measured in the pulse-echo setup and are calculated from the frequency spectra of two reflection signals. A schematic diagram of the ultrasonic attenuation measurement is shown in Figure 3.3. An immersion transducer with a central frequency of 25 MHz and a diameter of 6.35 mm is located vertically at a distance (z) of 15 mm from the specimen surface. An x-y goniometer and a balance plate were used to keep the transducer being always perpendicular to the specimen while scanning. A pulser-receiver (Panametrics 5073PR) excites the transducer to generate ultrasonic pulse signals in the water. The ultrasonic pulse is reflected at the front wall (water-steel interface) back to the transducer ($E_1(t)$) and the pulse transmitted into the specimen is reflected at the back wall (steel-water interface) also back to the transducer ($E_2(t)$).

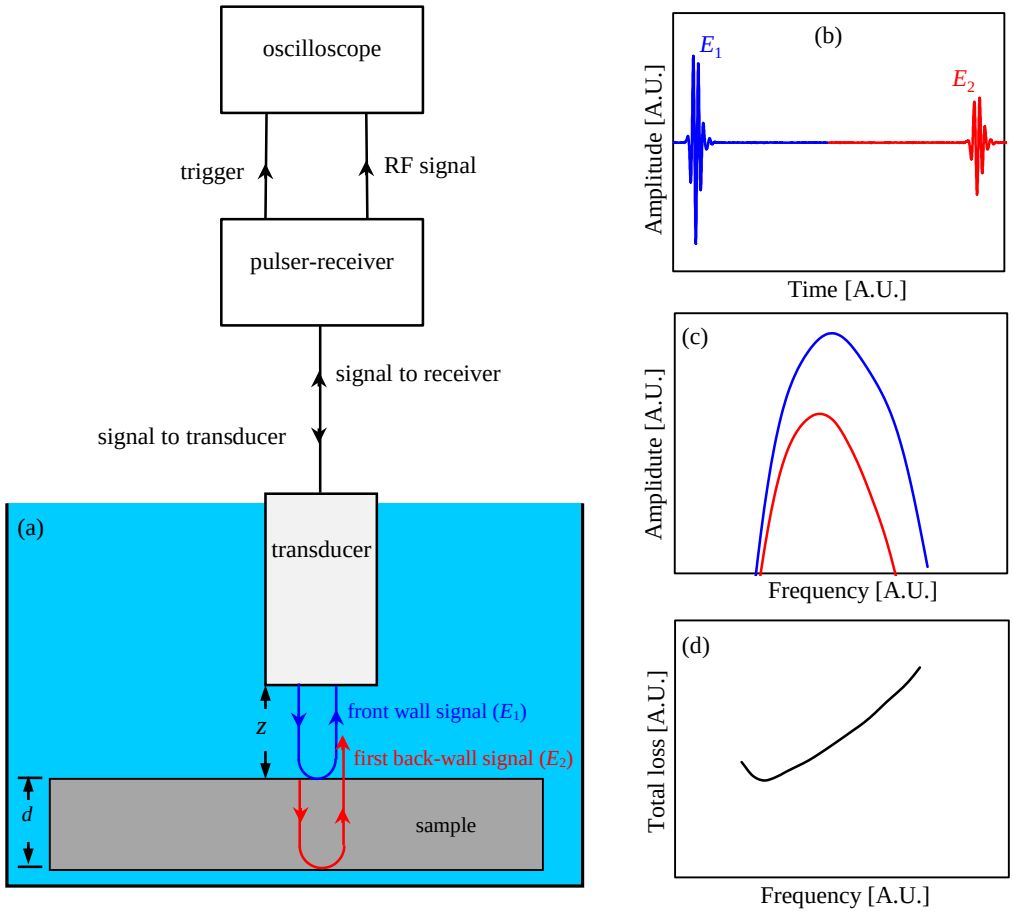

Figure 3.3. (a) Schematic representation of pulse-echo method for attenuation coefficient measurements, (b) Corresponding time domain RF signal, (c) Frequency domain signals and (d) total loss as function of frequency.

Between these two reflections, the ultrasonic pulse travels a distance 2*d* which is twice the thickness of the sample, interacting with the microstructure of the material. The detected signals are amplified by the receiver and sent to the oscilloscope which displays RF signals on its screen (Figure 3.3(b)). The ratio of the two frequency spectra of these two signals yields the total or apparent loss which not only includes the loss due to the material attenuation but also losses due to beam spreading, partial reflections (impedance mismatch) at the interfaces, and the rough surface scattering. Therefore, it is necessary to make corrections for these additional losses to the total loss to obtain the desired attenuation coefficient of the material. The first two effects are corrected using relevant theoretical formulas while the surface roughness effect is minimized by carefully polishing the specimen surfaces up to 2000-grade emery papers.

The frequency spectra of the front wall and first back wall echo signals are written as:

$$E_1(\omega) = S(\omega)D_1(\omega)R_{ws}(\omega)e^{2ik_w z - 2\alpha_w z} \tag{3.3}$$

$$E_2(\omega) = S(\omega)D_2(\omega)T_{ws}(\omega)(-T_{sw}(\omega))R_{sw}(\omega)e^{2ik_w z - 2\alpha_w z}e^{2ik_s d - 2\alpha_s d} \tag{3.4}$$

where $S(\omega)$ is the frequency spectrum of the source signal, $R_{ws}(\omega)$ and $R_{sw}(\omega)$ are the reflection coefficients of water-steel and steel-water interfaces, $T_{ws}(\omega)$ and $T_{sw}(\omega)$ are the transmission coefficients of water-steel and steel-water interfaces, k_{sw} and α_{sw} are the wavenumber and attenuation coefficient of water, and are the wavenumber and attenuation coefficient of the steel specimen, and $D_1(\omega)$ and $D_2(\omega)$ are the diffraction corrections for the propagation paths for the first and second echoes, for which the equation (2.13) from Rogers and van Buren [75] is used to analytically determine the diffraction correction losses. From Eqs. (3.3) and (3.4), one gets the formula for the attenuation coefficient of the specimen with the other two effects taken into account:

$$\alpha_s(\omega) = \frac{10}{d}\log\left[\frac{E_1(\omega)}{E_2(\omega)}\frac{D_2(\omega)}{D_1(\omega)}T_{ws}^2\right] \tag{3.5}$$

3.4.1 Ultrasonic C-scan imaging.

In order to better observe the microstructural changes produced by the embrittlement process, a series of c-scan images of the attenuation coefficient were obtained by scanning the specimens in an area of 20 × 20 mm^2 using the immersion ultrasonic measurement setup described in the above. The spatial resolution in the scanning system with stepping motors is 200 μm. Figure 3.4 illustrates the experimental arrangement of the ultrasonic c-scan setup using pulse-echo configuration and the way the specimen is scanned. At a frequency of 20 MHz, the longitudinal wave has a wavelength (λ) of about 290 μm. The scanning and imaging formation is done using commercial ultrasonic c-scan software, MISTRAS™. For the purpose of creating attenuation images, it is not necessary to make corrections for the other effects as discussed in the above because these other effects will remain constant at all locations.

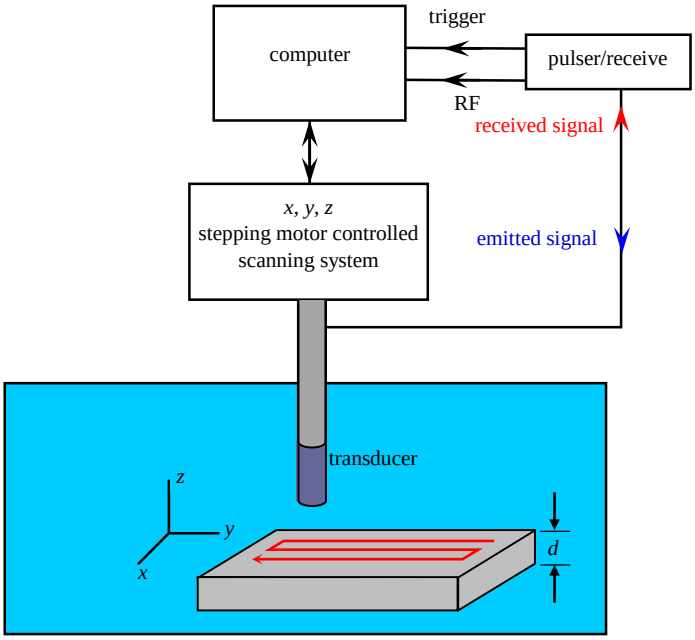

Figure 3.4. Experimental arrangement for c-scan imaging.

In this case, the front wall (E_1) and first back wall (E_2) peak-to-peak voltages are recorded at each scanning position and the following total loss is used to create an image:

$$L_{Total} = 20\log_{10}\left(\frac{E_1}{E_2}\right) \tag{3.6}$$

3.5. Nonlinear ultrasonic measurements.

In contrast to the conventional linear ultrasonic NDE, nonlinear ultrasound offers a unique advantage of high sensitivity to microstructural changes such as those due to the precipitation of second phases, fatigue damage, plastic deformation, and thermal damage in metallic alloys. In this research, ultrasonic measurements were conducted to determine the nonlinearity parameter (β) of thermally embrittled 2507 SDSS specimens. The β parameter of these specimens were measured by exploiting two different nonlinear effects: the acoustoelastic effect and second harmonic generation in Rayleigh waves. Experimental results indicate that nonlinear parameter obtained from these independent experiments are consistent and sensitive to the 475 °C embrittlement process.

3.5.1 Rayleigh wave measurement.

Figure 3.5 shows the experimental setup used for the generation and detection of the fundamental and second harmonic Rayleigh waves [104]. A function generator (Agilent 33250A) generates a 30-cycle tone-burst signal. A high power gated amplifier (RITEC GA-2500A) amplifies this tone-burst signal by as much as 60 dB. A wedge transducer that is mounted with a narrow-band contact piezoelectric transducer (Panametrics V106; a center frequency 2.25 MHz) generates Rayleigh waves in the specimen. Light lubrication oil acoustically couples the wedge and transducer as well as the wedge and the specimen. An air-coupled transducer with center frequency 4 MHz (UltranNCT4-D13) detects the leaky Rayleigh wave signals which are post-amplified by 40 dB. A digital oscilloscope records and averages 512 detected ultrasonic signals.

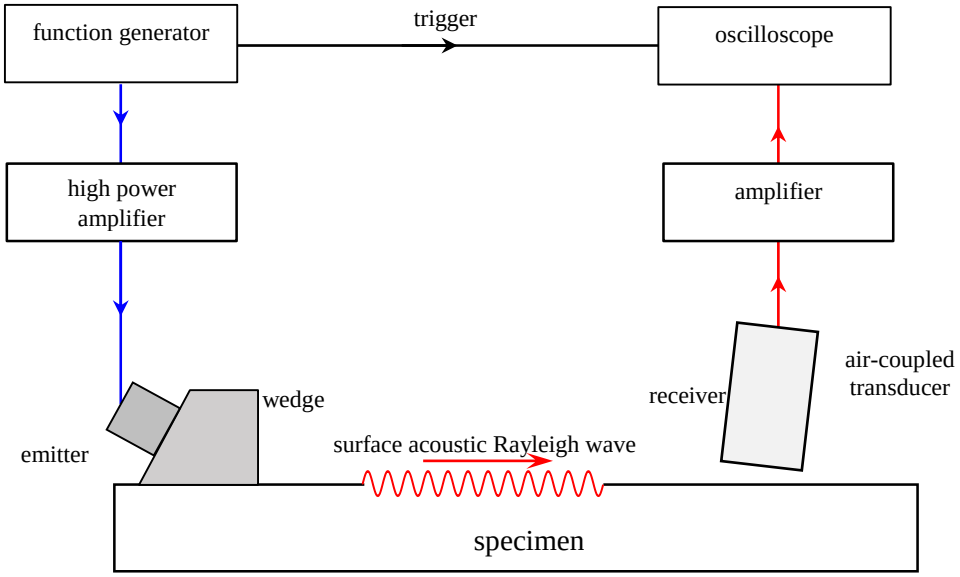

Figure 3.5. Experimental setup for nonlinear surface wave measurements.

Figure 3.6(a) shows a typical time domain signal with a steady state portion in the middle. A Hann window was applied to suppress the transient responses in the beginning and at the end. The fast Fourier transform (FFT) maps the time domain signal to the frequency domain. Figure 3.6(b) shows the frequency spectrum corresponding to the time domain signal in Figure 3.6(a), where the contributions of the fundamental (A_1), and second harmonic (A_2), amplitudes are clearly visible.

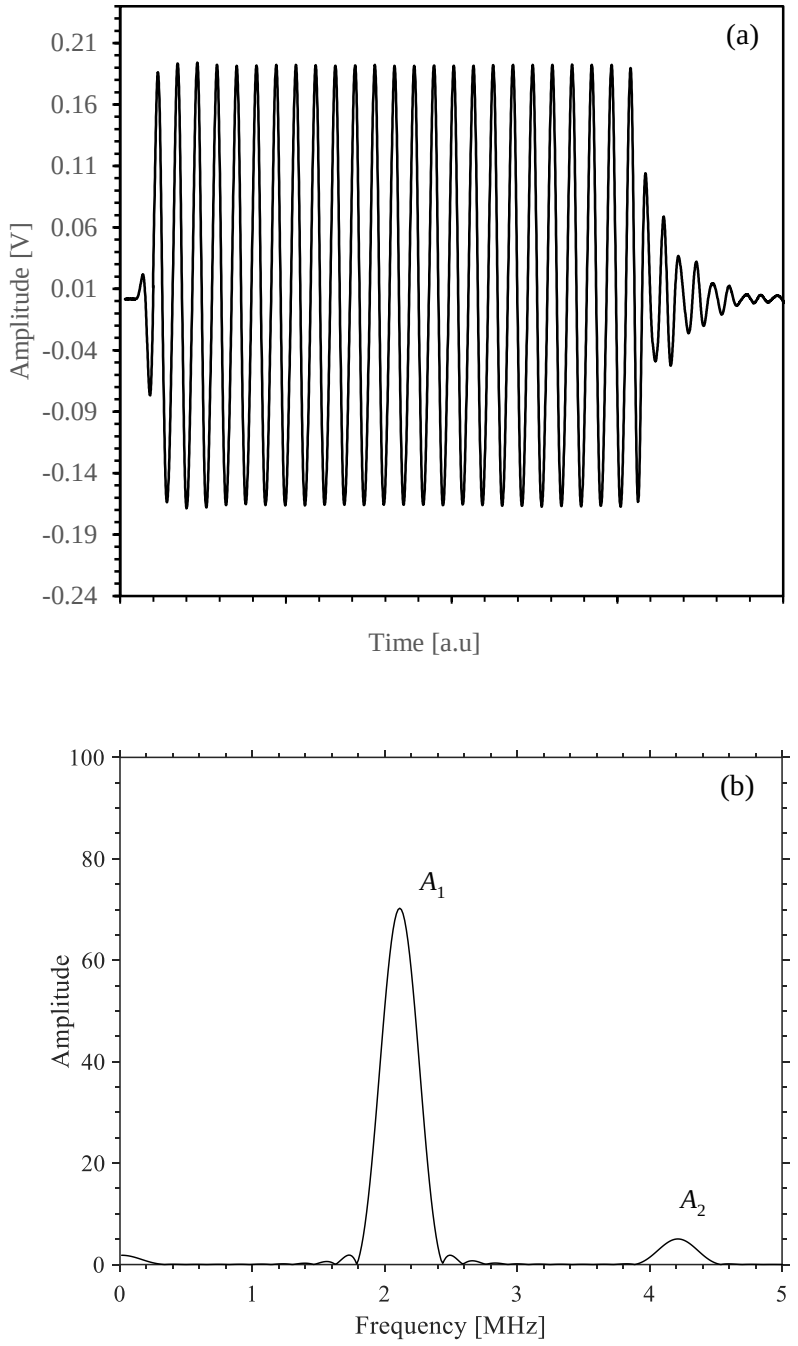

Figure 3.6. (a) A typical time-domain signal and (b) its frequency spectrum that shows both fundamental and second harmonic amplitude.

Figure 3.7(a) shows the amplitude of the fundamental signal as a function of propagation distance, where A_1 decreases monotonically with propagation distance due to the diffraction and attenuation effects. Figure 3.7(b) shows that the material nonlinearity causes a monotonic increase of A_2 with increasing distance propagation. Figure 3.7(c) shows an approximately linear increase of the ratio with propagation distance; the nonlinear parameter (β) is the slope of this plot according to Eq. (2.6).

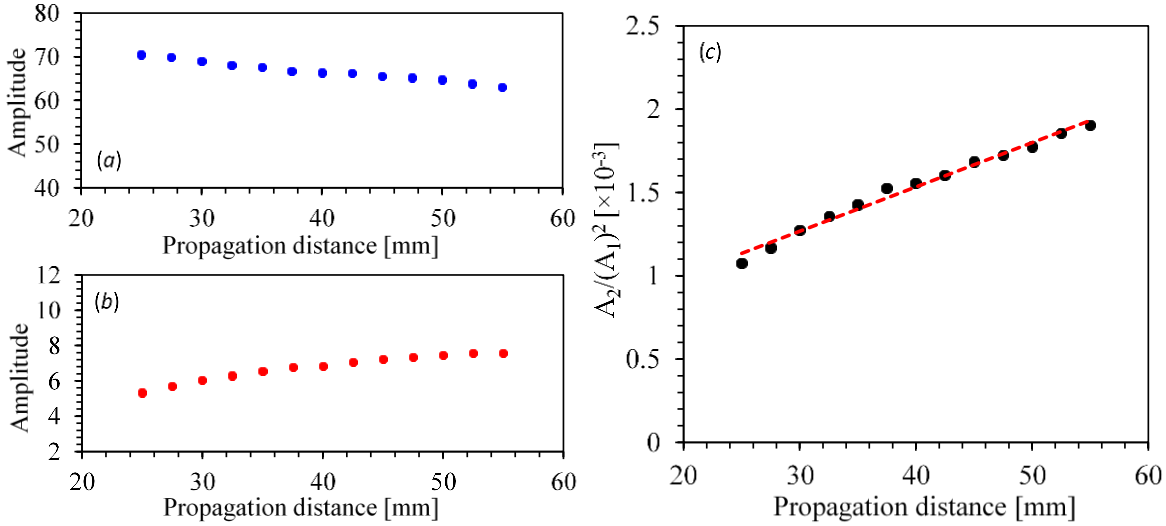

Figure 3.7. Amplitudes of A_1 (a), A_2 (b), and $A_2/(A_1)^2$, (c) as a function of propagation distance.

Figure 3.8(a) shows a schematic of the experimental setup for the acoustoelastic measurement, where a pulser/receiver excites contact longitudinal and shear wave transducers with a center frequency of 5 MHz and diameter of 6.3 mm. A Stanford Research digital delay pulse generator gates two consecutive back wall echoes and then a Stanford Research universal time interval counter measures the time of flight with high accuracy.

A series of measurements were conducted on 2507 SDSS specimens aged at 475 °C for different thermal exposure times to determine the acoustoelastic constants. These coefficients were estimated from shear-wave birefringence and longitudinal wave velocity measurements. The stress-dependent shear and longitudinal wave velocities were measured while the specimens were under uniaxial tension and compression. Both the shear and longitudinal shear waves propagate perpendicular to the loading direction. Shear waves have a polarization either normal or parallel to the loading direction.

Figure 3.8(b) shows the transducer-sample configuration for the case of shear wave birefringence measurement on the specimen under the uniaxial compression-tension load which varied from -8,874 N to 28,913 N and applied at the frequency of 10 Hz. 5 MHz contact transducers (shear and longitudinal waves) were exited using a manually controlled pulser/receiver (Olympus® model 5073PR) and then two consecutive back-wall echoes were gated using the SRS® Digital Delay/Pulse Generator model DG535. The time shift between the unloaded and loaded conditions was then measured using an SRS® universal time interval counter at a sampling frequency of 5 Hz.

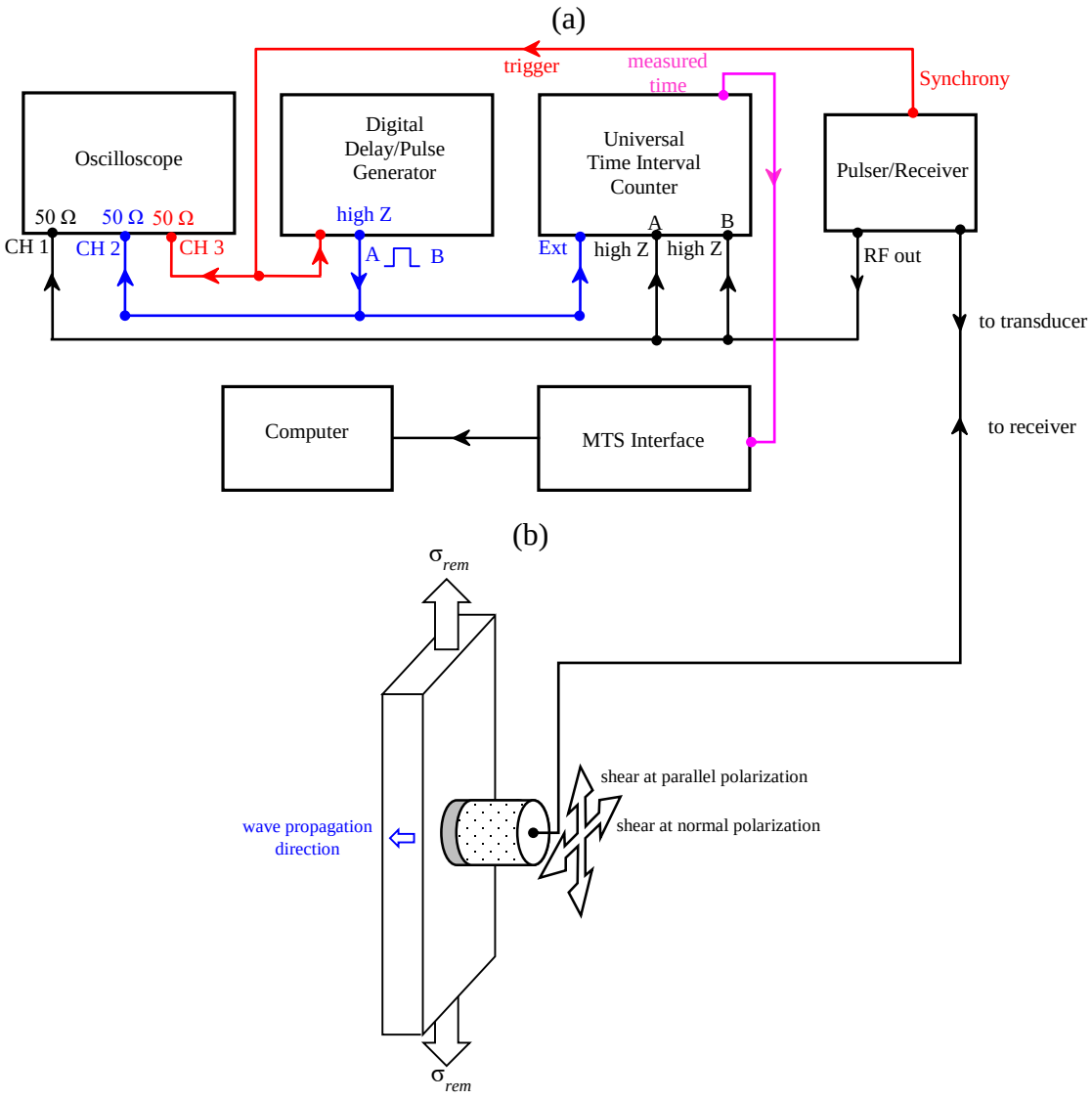

Figure 3.8(a) Experimental setup for acoustoelastic velocity measurement and (b) transducer-sample configuration for velocity measurements under cyclic loading.

3.6. Thermoelectric measurements on thermally embrittled 2507 SDSS.

The presence of the α′ phase has been only detected through very special techniques such as transmission electron microscopy and atom probe field ion microscopy [45, 56, 105]. Due to this difficulty, this phenomenon is often studied through indirect observations such as hardness and impact energy.

The Seebeck coefficient was used as the NDE method to assess the embrittlement of the 2507 SDSS after thermal aging. For TEP measurements, the thermoelectric voltage was measured using Walker Scientific alloy thermo-sorter model ATS-6044T that has probes with cold and hot tips made of copper and gold, respectively. Figure 3.9 shows a schematic diagram of the thermoelectric measurements used in the characterization of the embrittlement phenomenon. The measurement system includes two reference electrodes; one of the electrodes is heated by an electrical means to a preset temperature T_h, while the other electrode is left cold at room temperature T_c. For the measurement of Seebeck coefficient, a temperature difference (ΔT) is produced between the electrodes and the corresponding voltage (ΔV) developed between the ends is measured. The measurement is done rapidly in a few seconds to assure that the hot reference electrode is not cooled down by the specimen while the rest of the specimen beyond the close vicinity of the contact point is not warmed up perceivably.

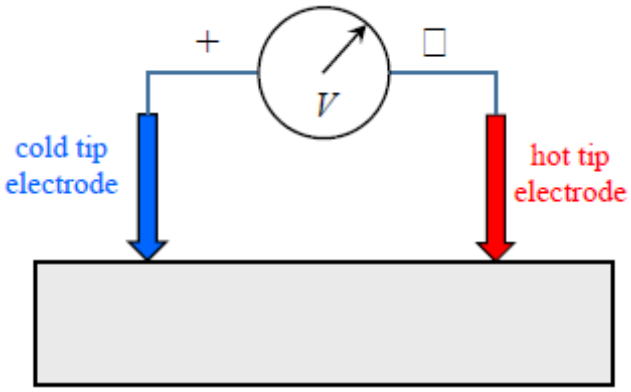

Figure 3.9. Schematic diagram of the thermoelectric measurements using a two-tipped probe.

The measured thermoelectric voltage is determined using [29]:

$$V_{SR} = \int_{T_c}^{T_h} \left[S_S(T) - S_R(T) \right] dT = \int_{T_c}^{T_h} S_{SR}(T) dT \tag{3.7}$$

where T is the temperature, and S_S and S_R denote the absolute TEP of the specimen and the reference electrode, respectively, S_{SR} is the relative TEP of the sample with respect to the reference electrode. Variations in the material properties affect the measured TEP as:

$$S_{SR} = S_S - S_R \tag{3.8}$$

In most experimental situations, the temperature-dependence of the TEP is neglected and can be approximated according to [100]:

$$V \approx \left(T_h - T_c \right) S_{SR} \tag{3.9}$$

Regardless of how high the temperature difference between the junctions is, only materials with different TEPs will generate a thermoelectric voltage. This unique feature makes the thermoelectric measurement an extremely sensitive NDE method. The TEP of each sample was calculated using a linear model obtained from best-fitting the measured thermoelectric voltages in materials with known TEPs, namely copper, alumel and chromel from [91] in this way the TEP measurement method allows to obtain voltage values within few seconds.

3.7. Microstructural characterization.

For the microstructural analysis, specimens were prepared by conventional metallographic polishing and etching in a KOH electrolyte (50 g KOH, 100 ml water) with a voltage of 3 V for approximately 10 seconds. Microstructural examination of specimens was done using optical microscopy and scanning electron microscope (SEM) using JEOL JSM-5910LV microscope.

3.8. Mechanical characterization.

Charpy impact test, Rockwell and Vickers microhardness test, and tension test were selected to measure the performance of the 2507 SDSS during the 475 °C aging treatment.

3.8.1 Charpy impact test.

This test is commonly used to determine the brittleness of a material. This test detects small changes in the impact property of the material that has been affected by different fabrication processes and generally these changes are not detected by the quasi-static tension test. The test is conducted on a specimen with a square cross section (10×10 mm) and contains a 2 mm deep notch with a 0.25 mm root radius and a 45° angular aperture. The specimen is supported horizontally as a beam. An impact pendulum is used to strike behind the notch forcing the specimen to bend and fracture at high strain rates. The energy absorbed during the fracture is usually expressed in joules. Charpy impact test was performed at the room temperature.

3.8.2 Tension test.

Tensile tests of SDSS samples were carried out in the aged specimens. Aged tensile specimens were prepared having rectangular cross-section and a gauge length of 70 mm. All tests were conducted at room temperature on an MTS servo-hydraulic universal testing machine at a crosshead speed of 0.005 mm/min.

3.8.3 Hardness measurements.

Vickers microhardness was measured using a computer controlled Minutolo microhardness tester that is equipped with a manually controlled *x-y* stage unit and digital micrometer heads with 1 μm spatial resolution. Five measurements of Vickers microhardness were performed in five individual grains of ferrite and austenite using a load of 10 g.

Rockwell C hardness establishes the bulk hardness of materials. This hardness testing does not give a direct measurement of any performance properties but in many cases the hardness of a material connects directly with wear resistance and strength.

3.9. KJMA model applied to embrittled 2507 SDSS.

Mechanical properties such as hardness, absorbed impact energy, and strength are affected by precipitation processes caused by exposure to high temperatures. Models such as the KJMA model have been used to simulate these behaviors as a function of holding time [106-109]. The effect of phase transformation on measured microhardness and absorbed impact energy in 2507 SDSS specimens has been described using the KJMA model [110]. To simulate the component behavior the measured values are fitted to an equation of the form [109, 111]:

$$H = 1 - e^{-(kt)^n} \tag{3.10}$$

where H is a progressively changing material property as function of holding time (t), and aging temperature (T). As stated by this equation, this equation varies continuously from 0 to 1 as the phase transformation advances from beginning to its saturation. The exponent n is the Avrami exponent, which has been related to the nucleation and growth mechanism and the geometry of the newly growing phase [111]. The term k is a kinetic coefficient defined by the Arrhenius equation:

$$k = k_0 e^{-\frac{Q}{RT}} \tag{3.11}$$

where k_0 is the pre-exponential factor, Q is the effective activation energy for the phase transformation, and R the universal gas constant (8.314 J-mol^{-1}K^{-1}). Using $H_{\max}$ as the maximum measured microhardness and H_0 as the measured microhardness value of the unaged material [110].

$$H(t,T) = H_{\max} - \left(H_{\max} - H_0\right) e^{-(kt)^n} \tag{3.12}$$

The experimentally measured microhardness was fitted to the KJMA equation to obtain the value of n; the value of k was determined from equation (3.11) using k_0 and Q as the fitting values.

CHAPTER IV. RESULTS AND DISCUSSION

4.1. Microstructural characterization.

In the as-received condition, the microstructure of the 2507 SDSS is composed of elongated grains of austenite (γ) in a matrix of ferrite (α) as shown in Figure 4.1. It has been reported that when this material is subjected to long-term aging at 475 °C, embrittlement predisposes the material to a selective or localized corrosion attack [112]. This degradation phenomenon is attributed to the spinodal decomposition that leads to formation of α′, which then causes Cr depletion in the alloy-surrounding matrix. While it is possible to observe the precipitation of α′ using powerful tools such as TEM along with energy dispersive X-ray spectroscopy (EDS) microanalysis, the lack of evidence of phase separation is due to the very small size of the precipitates and their coherence with the matrix [113].

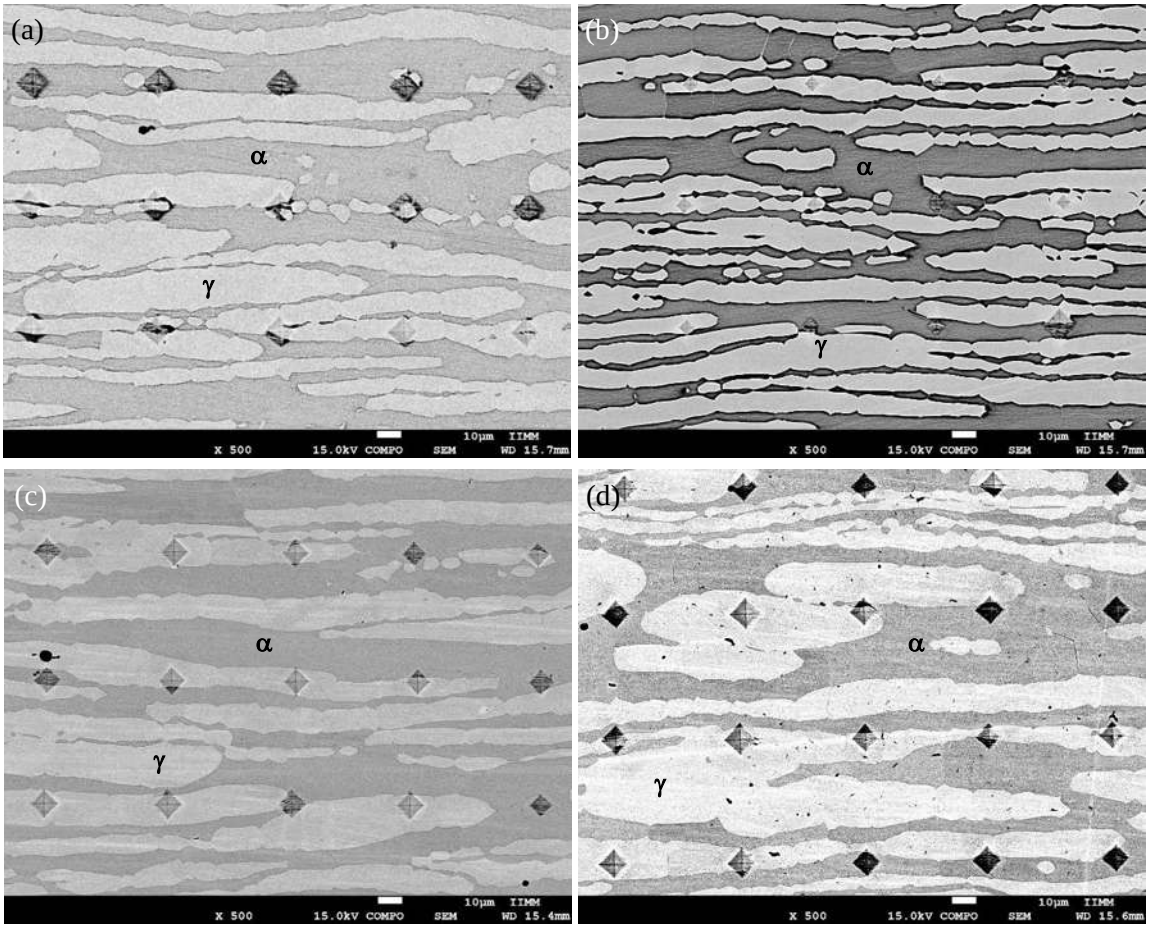

Figure 4.1. Microstructure of 2507 SDSS in a) the as-received condition and aged for: b) 10 min, c) 50 h and d) 100 h. (Note that these diamonds are indentation marks from the microhardness test).

In the SEM images of Figures 4.1(b-d), there are no perceivable changes in the microstructural characteristics of the 2507 SDSS between unaged sample and sample aged for 100 h. It is important to note that the embrittlement treatment causes detectable changes in the fraction of the phase [114, 115].

Figure 4.2 shows an SEM image at magnification of 10,000x, which shows the microstructure of the 2507 SDSS after 300 h aging treatment. In this image, the austenite phase keeps its initial characteristics while appreciable changes can be seen, in contrast, in the ferrite phase (the middle part in Figure 4.2). Small white precipitate particles are seen along with black dots revealed by the etching. The numerous precipitates in Figure 4.2 are ascribed to the G-phase precipitates, this type of precipitates have been reported by Sahu et al. [55].

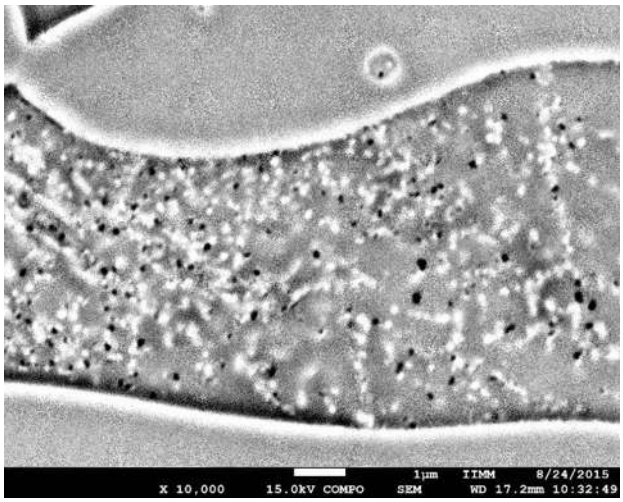

Figure 4.2. High magnification SEM micrograph of precipitated G-particles after aging for 300 h.

The microstructure of the specimens unaged and aged for 50 hours are characterized by the presence of dislocation structures consisting of numerous dislocation tangles in the ferrite indicating high dislocation activity. These can be seen in the bright-field TEM images in Figure 4.3(a-b). Figure 4.3(c) shows that the dislocations have almost vanished and the presence of mottled contrast as well as precipitates.

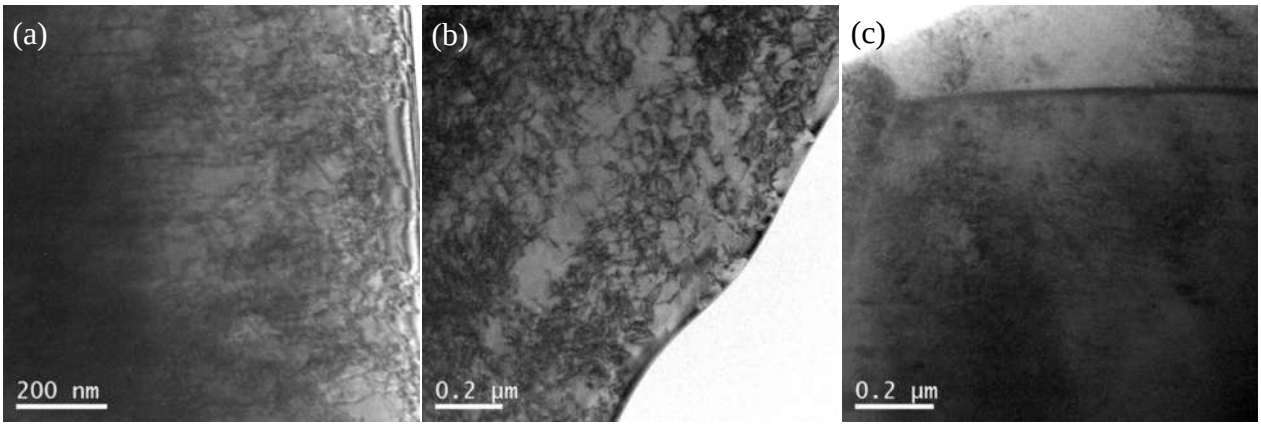

Figure 4.3. Transmission electron microscopy bright-field images showing: (a-b) complex dislocation tangle in the untreated specimen and specimen aged at 475 °C for 50 h and (c) aged for 300 h showing a mottled contrast in ferrite associated with spinodal decomposition.

The reduction in the dislocation density was correlated to changes in the level of plastic deformation induced texture by measuring the relative normalized shear wave birefringence $\Delta = (c_{sp} - c_{sn})/c_{sp}$, of aged samples, where c_{sp} and c_{sn} are shear wave velocities with polarizations parallel and normal, respectively, to the chosen reference direction, the total Δ change from untreated to 300 h holding time is about 10.14% as it is shown in the following.

4.2. Effect of aging time on longitudinal and shear wave velocity.

Figure 4.4 shows the shear wave velocity measurements with increasing holding time, as it can be seen, the velocity of the fast and slow modes increase a 10 h and slightly decrease at 50 h and continually increase after 50 h holding time. Also, it can be seen that the slow mode exhibits a bigger increment that the fast mode.

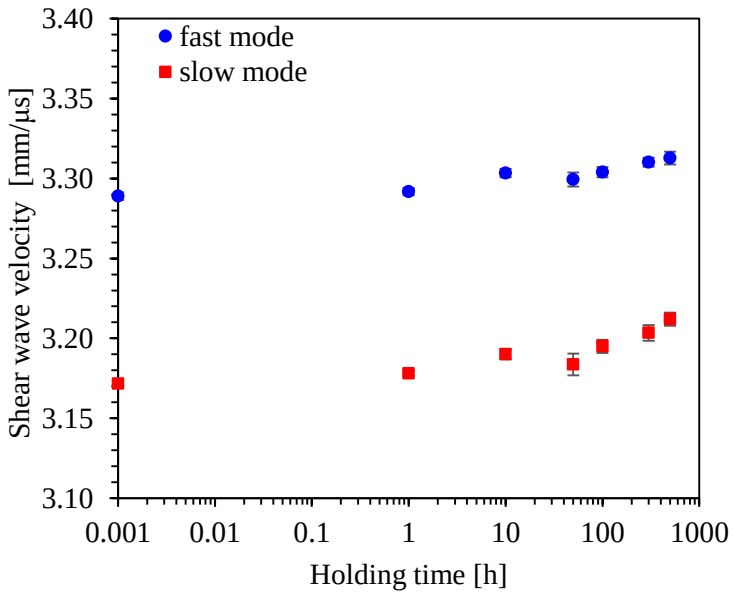

Figure 4.4. Shear wave velocity measurements as function of aging time.

Figure 4.5 shows the percent change in the shear wave birefringence were it can be seen that the shear wave birefringence gradually decreases between the untreated and 10 h holding time (0.1416% change), at 50 h it increases to have similar values to the untreated sample. The rate of change remarkably increases after 50 holding time with a total change in the shear wave birefringence of about 0.55%.

This indicates that the initial material´s texture gradually decreases as holding time increases.

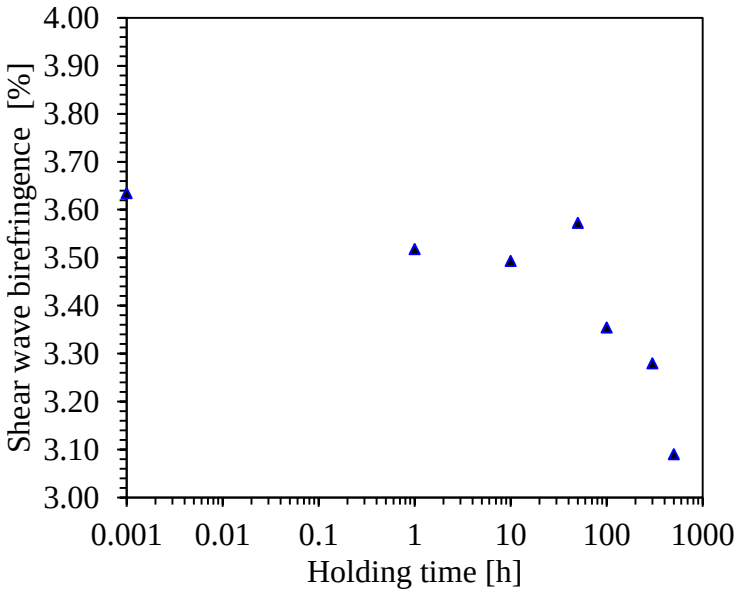

Figure 4.5. Shear wave birefringence as function of holding time.

4.3. Effect of aging time on Vickers microhardness.

The microhardness is used as an indirect method to track property changes as a function of holding time and to determine if the 475 °C embrittlement is occurring. The Figure 4.6 shows the images obtained from hardness measurements, each image shows the microhardness at 1200 individual points separated by 50 µm. As seen in Figure 4.6(a), the as-received sample exhibit a very homogeneous hardness throughout the entire area (average = 315 HV with variance of ± 25), Figure 4.6(b) shows that at 50 h holding time, a microhardness increased to about 432 (green) in some areas, with some regions with peak microhardness values ranging from 432 HV to 525 HV. As the holding time increases to 100 h, more regions show microhardness values in the range of 432 HV to 550 HV with peak values around 600 HV; finally, Figure 4.6(d) shows that at 300 h an average microhardness value of 434 HV with more regions with microhardness peak values around 615 HV.

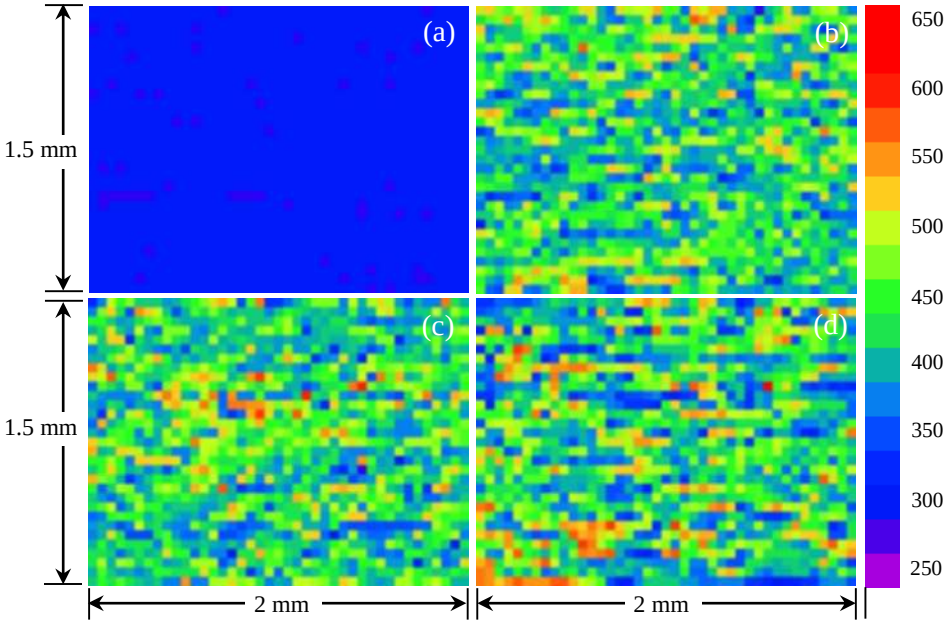

Figure 4.6. Vickers microhardness maps of 475°C embrittled 2507 SDSS. (a) as-received condition and aged for (b) 50 h, (c)100 h and (d) 300 h.

Since some areas of the hardness images of Figure 4.6 are showing values of approximately 332HV, the Vickers microhardness was measured at each individual phase. Figure 4.7, shows that the measured microhardness of austenite shows small changes throughout the different aging times, while ferrite shows that microhardness increases gradually after 50 h aging treatment; this is a clear

manifestation of the 475°C embrittlement phenomenon. These results are in agreement with those of Weng et al. for 2205 DSS [56] where austenite shows small changes as a function of holding time.

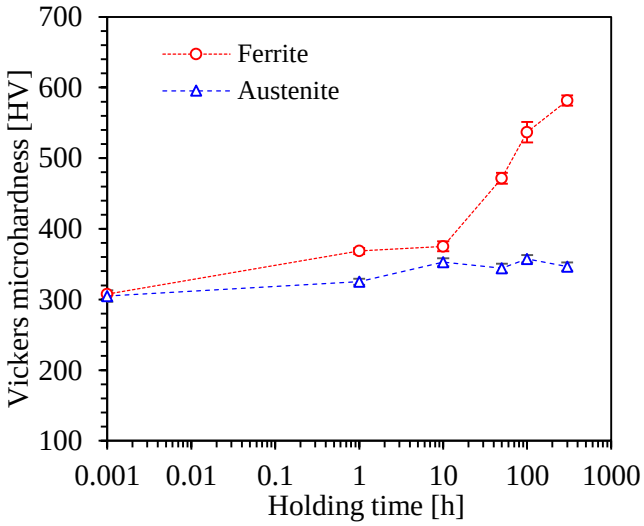

Figure 4.7. Effect of holding time on Vickers microhardness of ferrite and austenite at 475 °C.

4.4. Effect of aging time on impact energy.

Figure 4.8 shows the graph of absorbed energy determined from the Charpy impact test as a function of holding time at 475 °C with samples tested at -20 °C. It was found that even for short aging times there is a reduction on the impact energy of about 28 J for ten minutes and around 100 J for 1 hour.

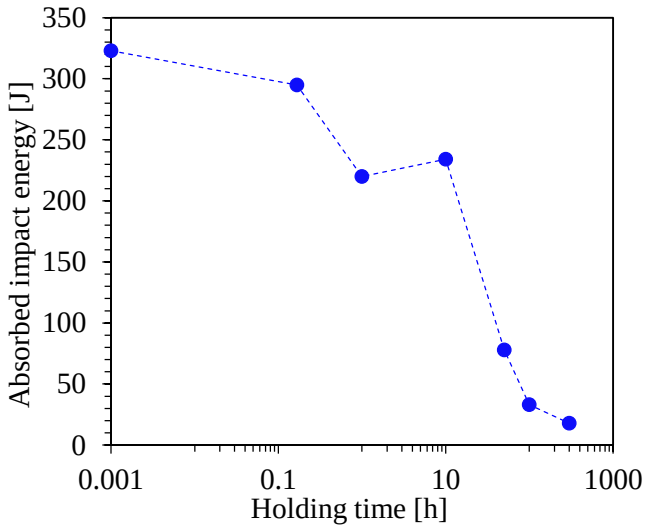

Figure 4.8. Effect of holding time on impact properties of 2507 SDSS aged at 475 °C

It is observed that the impact energy rapidly decreases to 78 J at 50 hours and oscillating at values between 18 J to 54 between 100h and 300 hours, losing significantly its ability to absorb energy. Similar results have been reported by Sahu et al. [55] who evaluated the deterioration of the impact energy of a 2205 DSS aged at 475 °C for 300 h. The authors observed that the impact energy reached a ‘‘saturation value’’ of 8 J for the aging times of 100, 200 and 300 h. The fracture features observed on Figure 4.9(a-b) illustrate dimpled fracture surfaces that are typical of microvoid coalescence in a ductile fracture. Fracture behavior changes completely for the holding times of 100 h and 300 h as seen in Figure 4.9(c-d), respectively. The presence of cleavage type fracture can be observed throughout the fracture surfaces indicating a brittle fracture. These results are supported by findings made by Chandra et al. [116] who concluded that the presence of α′ ferrite is a strong influence causing shearing of the austenite between the cleavage planes. Similar results are reported by Silva et al. [117]; they found that the presence of cleavage fracture related to the presence of α′ phase. It is clear that the formation of α′ phase has a much more considerable effect in the impact resistance of DSS.

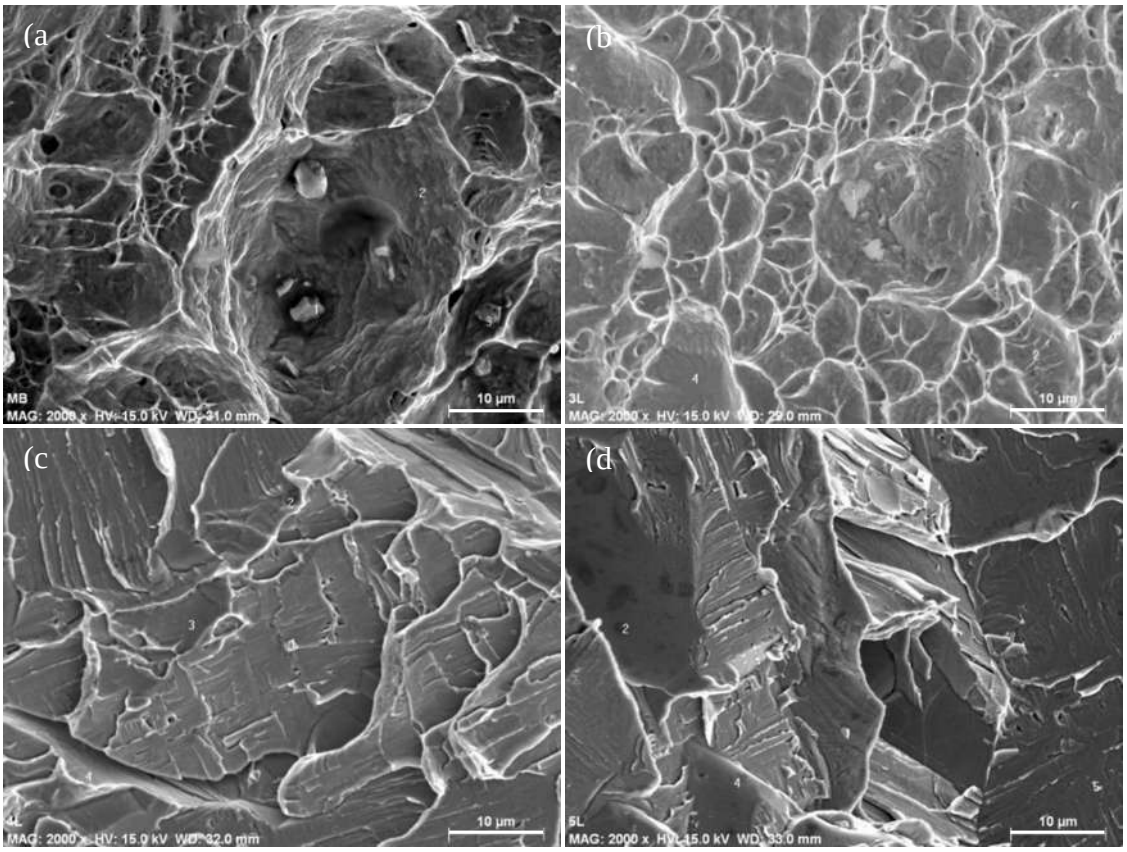

Figure 4.9. Fracture surfaces of impact specimens for (a) as-received; and aged for (b) 10 h, (c) 100 h and (d) 300 h.

4.5. Detection of localized conductivity using electric conductivity measurements.

Effects of 475 °C embrittlement on the corrosion behavior of gradually aged 2507 SDSS were investigated using a recently developed alternating current potential drop probe to measure electric conductivity as function of holding time. The results were compared to Q_r/Q_a ratio, critical pitting temperature and Vickers microhardness values and reasonable correlations were found. This research demonstrates the feasibility of using conductivity measurements as a reliable alternative to determine 475°C embrittlement and predicts the susceptibility to localized corrosion.

4.5.1. Experimental results.

The previously described low-frequency ACPD measurement setup has been used successfully for creep monitoring measurements [96]. The setup is capable of accurately measuring the potential drop at very low inspection frequency (3 Hz); this low frequency measurement is to assure an essentially quasi-static operation to avoid magnetic permeability effects typical of wide range of materials including the paramagnetic austenitic 304 stainless steel and ferromagnetic low-alloy Cr/Mo steels [95].

Figure 4.10 shows the electric conductivity variation as a function of holding time. Minor increases are observed for holding times up to 1 h. The electric conductivity shows a slight increment at 10 h. For longer holding times (50, 100 and 300 h), the electric conductivity of the DSS increases gradually to have a total change of approximately 4.68%. These variations in electric conductivity could be due to the transformation in the ferrite phase ($\alpha \rightarrow \alpha + \alpha'$).

This phase separation phenomenon occurs at a very small scale during the thermal exposure at a temperature of 475 °C. The elements Fe, Cr, and Ni, belong to the 3d-transition metals, Kawaguchi and Yamanaka [115] reported that a main effect on electrical conductivity of the transition metals comes from the scattering of the s electrons to the partially filled d band. On the other hand, within the ferrite phase, Cr depletion produces micro-regions with a higher Cr concentration affecting the corrosion resistance of the SDSS.

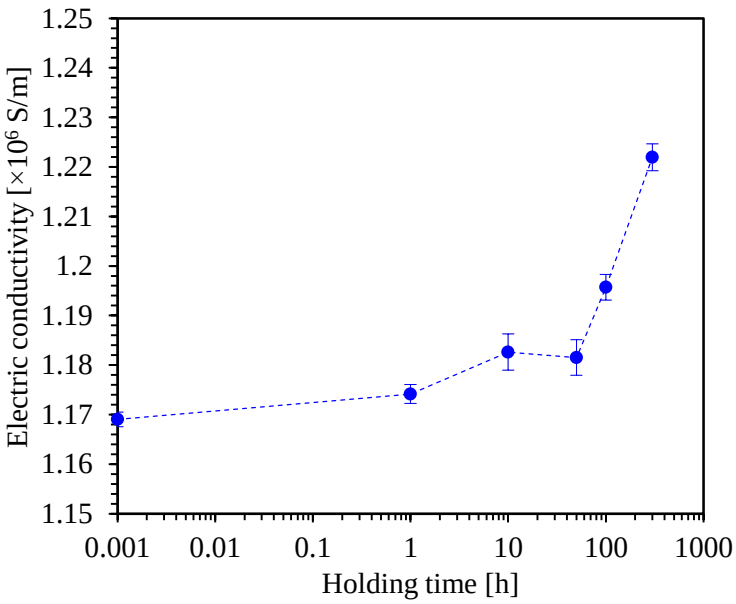

Figure 4.10. Electric conductivity as a function of the aging time for thermally embrittled 2507 SDSS at 475°C.

4.5.2. Determination of the resistance to localized corrosion.

It is known that the phase precipitation in DSSs due to welding or service at high temperature induces Cr and Mo depleted zones with the consequent decrease in their corrosion resistance [118]. It has been reported that the degree of sensitization (DOS) of DSSs increases as a function of the ageing time whereas the critical pitting temperature (CPT) shows the inverse behavior [119]. The results obtained in the present investigation are in agreement with the results reported by Ebrahimi et al. [119] for a 2205 DSS aged at 600 and 800 °C. In the present case the intention was to induce changes in mechanical properties and the resistance to localized corrosion of a 2507 SDSS subjected to 475 °C embrittlement for different periods in order to associate the degree of damage with ACPD measurements.

Figure 4.11(a) shows the DL-EPR curves obtained for 2507 SDSS samples in the as-received condition and aged at 475 °C for 50 h. From this figure, it is observed that at a potential around -0.28 V, the sample in the as-received condition presents an activation current density peak of 0.0074 A/cm^2, with no reactivation current peak formed during the reverse potentio-dynamic scan.

Also, for sample aged for 10 and 50 hours, the activation current density peak decreases gradually to values of 0.00688 and 0.0066 A/cm^2 respectively.

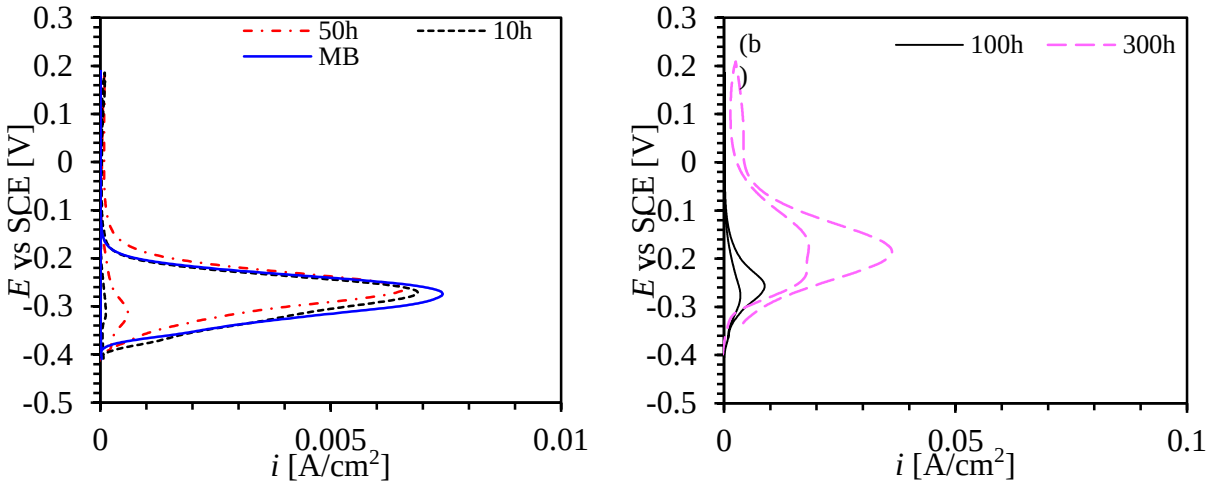

Figure 4.11. DL-EPR curves of 2507 SDSS untreated and isothermally aged at 475 °C (a) up to 50 h and (b) aged for 100 h and 300 h respectively.

In these aged samples, a gradual increase in the reactivation current from 0.00012 to 0.00058 A/cm^2 is measured during the reverse potentio-dynamic scan. Figure 4.11(b) shows that as holding time increases from 100 to 300 hours, the activation current density peak increases rapidly from 0.0086 A/cm^2 to a maximum value of 0.04. In the same way, the reactivation current shows a drastic increase from 0.01 to 0.02 A/cm^2 occurred during the reverse potentio-dynamic scan at a potential of 0.28 and 0.18 V, respectively. de Assis et al. [120] reported that the currents (I_a and I_r) increase with the presence of undesirable phases obtained by each heat treatment, as shown by the DL-EPR curves obtained for the aged 2507 SDSS at different conditions. The authors noticed that the increases of DOS are related with the increasing percentage of sigma phase as the ageing time increased inducing a higher susceptibility to localized corrosion in the aged samples. DL-EPR test performed on a 2404 DSS also suggests that the mechanism of α-α´ phase separation is the spinodal decomposition and that the degradation of corrosion resistance derived from this phenomenon [121]. Chandra [116] reported the detection of Cr-depleted zones associated to the spinodal decomposition of the α-ferrite phase by DL-EPR measurements in a solution of 0.5M H2SO4 + 0.01M KSCN for 2205 DSS aged at 400 °C for 5000 hours.

It is well established that the current peak in the reactivation loop is caused by preferential corrosion attack due to Cr depletion initiated by the precipitation of Cr-rich phases in duplex stainless steels. This is clearly observed at 50 h, where the reactivation peak appears, being an indication that the embrittlement phenomena affects the corrosion resistance of the 2507 SDSS; for longer holding times, the activation and reactivation peaks continue to increase, clearly indicating the presence of Cr rich phases. In the present case, the most influential metallurgical transformation induced by the 475 °C embrittlement that can reduce the resistance to localized corrosion of the 2507 SDSS is the spinodal decomposition of the ferrite phase ($\alpha \rightarrow \alpha + \alpha'$) since carbides, nitrides, intermetallics and tertiary phases can precipitate at temperatures higher than 600 °C. Assuming that the ratio Q_r/Q_a represents the localized attack at zones adjacent to electrochemically detrimental phases (α´ Cr rich phase) in the present investigation [120], Figure 4.12 shows that the quantity of the undesirable α´ phase increased with the ageing time which is in agreement with the behavior observed for the electric conductivity as a function of the ageing time.

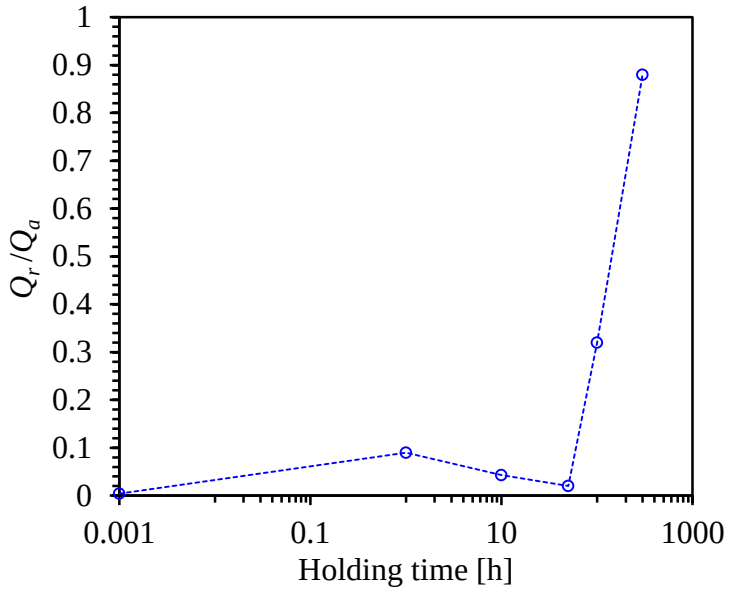

Figure 4.12. Q_r/Q_a as function of holding time.

Figure 4.13 is a sequence of SEM images showing the effects of DL-EPR test on samples aged for different periods. Figure 4.13(a) shows the image of sample aged for 10 h and slight corrosion attack is observed in the ferritic and austenitic phases. On the other hand, as time increases, as it is possible to observe in Figure 4.13(b) that at 50 h, the ferrite grains exhibit significant pitting corrosion, whereas the austenitic phase remains essentially undamaged. Figure 4.13(c) shows that for long holding times, ferrite phase begins to dissolve and at 100 h some grains clearly show this effect. The attack in these grains is more severe and ferrite phase is dramatically consumed as can be seen in Figure 4.13(d). This can be attributed to the fact that Cr depleted zones are susceptible to preferential corrosion attack. Furthermore, as it is seen in these images, the aging treatment does not have a corrosion effect on the austenitic phase.

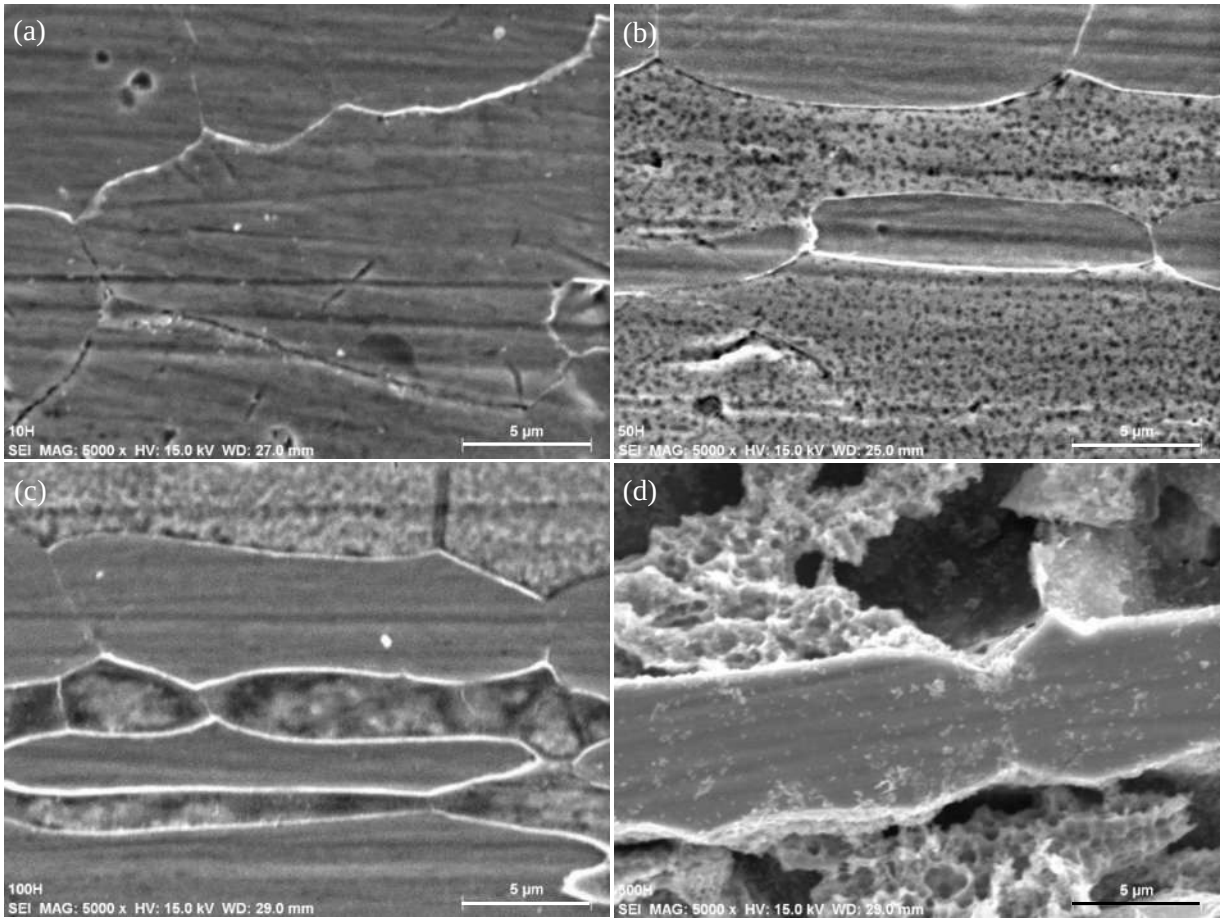

Figure 4.13. SEM micrographs showing the surface characteristics 2507 SDSS after DL-EPR tests aged at 475 °C for: (a) 10h (b) 50 h, (c) 100 h and (d) 300 h respectively.

The measurements of the CPT indicate that for short ageing periods there is almost no degradation of the resistance to pitting corrosion as can be observed in Figure 4.14. After 10 hours of ageing, the CPT presents a clear reduction compared to samples aged up to 1 h. Longer ageing time induces a drastic drop of the CPT to values lower than 15 °C for the samples aged for 300 h. Ebrahimi et al. [119] reported a decrease in the CPT on aged samples of 2205 DSS at 600 °C as the ageing time increased. Pezzato et al. [122] reported values of CPT of 88 °C for annealed samples of 2507 SDSS and values 84 and 76 °C for samples aged at 850 °C for 5 and 35 min respectively.

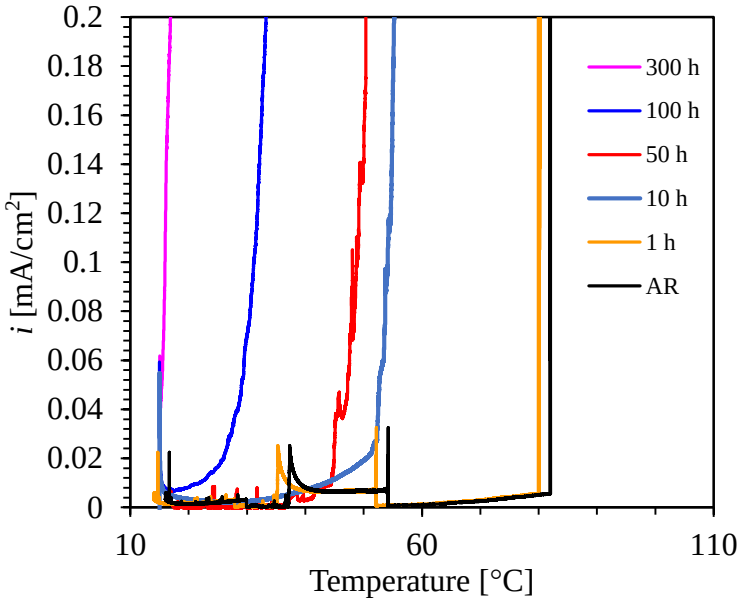

Figure 4.14. Typical curves of current density as function of temperature for 2507 SDSS after CPT test for as-received condition (AR) and aged for 1, 10, 50, 100 and 300 h respectively.

Figure 4.15 shows the CTP values at the different aging times; the highest value corresponds to the aging range of AR to 1 h, and the lowest value corresponds to the sample aged for 300 h. The trend exhibited by the CTP is quite similar to the results obtained from measured absorbed impact energy tests, and correlates with the hardening behavior exhibited by the ferrite phase where microhardness exhibited a substantial increment after 50 h holding time.

Örnek et al. [105] reported a drop of the CPT after 20 hours of 475 °C embrittlement of 2205 DSS which also decreased even more for longer ageing times. Spinodal decomposition is believed to reduce the resistance to localized corrosion for aging times longer than 10 hours, with other precipitates affecting the corrosion resistance due to the formation of Cr depleted zones.

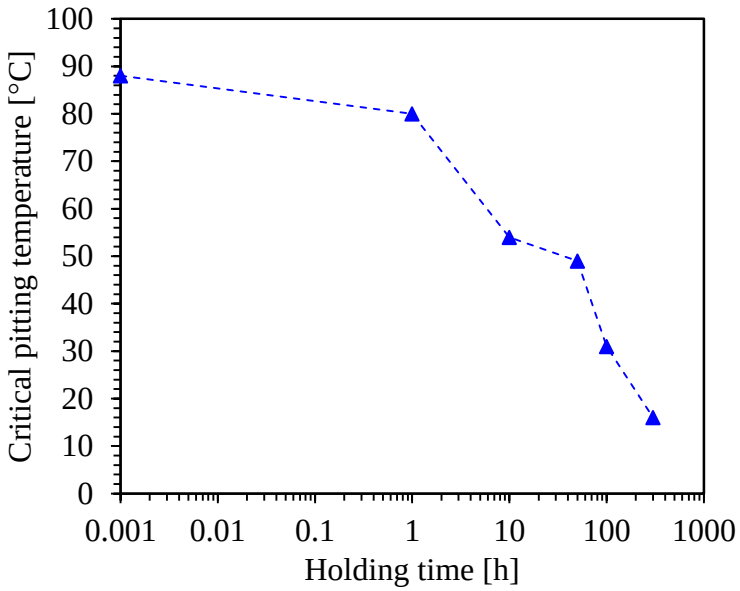

Figure 4.15. CPT values as a function of aging time.

4.5.3. Relation between microhardness CPT and electric conductivity.

The interpretations of the results from the electric conductivity, microhardness and CPT measurements is provided in Figure 4.16. The entire behavior could be divided into two stages: the initial stage (I), for holding times up to 1 h, clearly shows a small but simultaneous increase in microhardness and conductivity with a drop in CPT. The characteristics of the experimentally measured microhardness allows for the conclusion to be drawn that the microstructural changes associated with the decomposition of ferrite just begins. For stage II, with holding times ranging from 1 to 300 h a rapid increase in electric conductivity and microhardness as well as a reduction in the CPT all these probably dominated by the contribution α´precipitation.

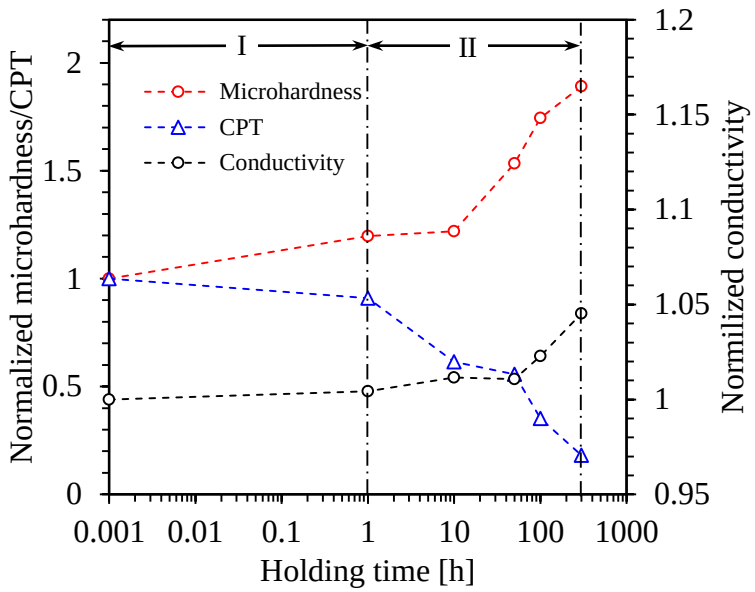

Figure 4.16. Comparison of electric conductivity, microhardness of ferrite phase and CPT results.

4.6. Effect of aging time on ultrasonic attenuation.

The high-frequency ultrasonic attenuation (> ~20 MHz) is sensitive to microstructural changes in metallic materials and its use is explored in this study to detect low-temperature embrittlement of 2507 SDSS. The ferrite phase experiences a microstructural transformation at elevated temperatures and the consequences of this transformation include reductions of corrosion resistance and fracture toughness as well as changes in the mechanical properties. Experimental results show that the measured attenuation coefficient decreases monotonically with the progress of embrittlement and c-scan images can markedly distinguish the gradual transformation. Vickers microhardness is measured to track the degree of embrittlement. Analysis performed by SEM and TEM at different stages supports the decreasing trend of the ultrasonic attenuation.

4.6.1. Changes in signal amplitude.

When an ultrasonic wave propagates through a material that exhibits a certain grain morphology and crystallographic anisotropy, the ultrasonic beam is scattered in a different direction resulting in a loss of amplitude i.e., the beam is attenuated by the local grain orientation.

The ultrasonic attenuation measurement has two purposes: the first is to study the effect of the embrittled microstructure on the attenuation coefficient as a function of frequency; and the second is to determine a frequency at which images of the attenuation coefficient can be constructed. Figure 4.17 shows the experimentally measured attenuation coefficient as a function of frequency for different holding times. Note that the lines in the figure represent the best-fit curves for each data set. The results show that the attenuation coefficient increases with frequency while it decreases with holding time. Note that the attenuation curves for 10 minutes and 10 h are not shown in this figure since they overlap with the untreated specimen and the same overlapping occurs between 100 h and 300 h indicating that the microstructural transformation does not affect the ultrasonic attenuation. It is also seen in this figure that in the low frequency range up to 15 MHz, the attenuation coefficient changes too little to detect the microstructural changes. On the other hand, at frequencies higher than 25 MHz, the attenuation coefficient shows appreciable changes to effectively separate the beginning of such microstructural changes.

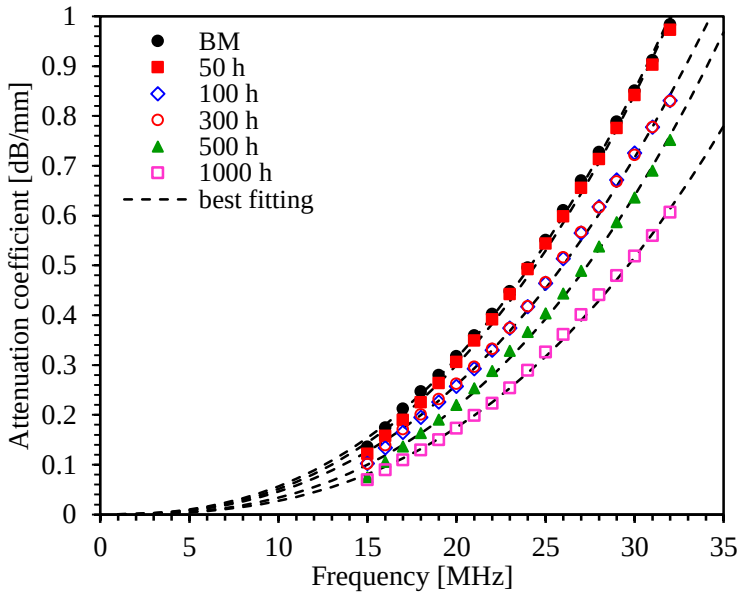

Figure 4.17. Attenuation coefficient as function of ultrasonic frequency on 2507 SDSS for untreated condition (BM) and aged for 50, 100, 300, 500 and 1000 h.

Figure 4.18 shows the attenuation coefficients as a function of holding time for three different frequencies. The attenuation coefficient slightly decreases till 50 h while it decreases more notably for the remaining time.

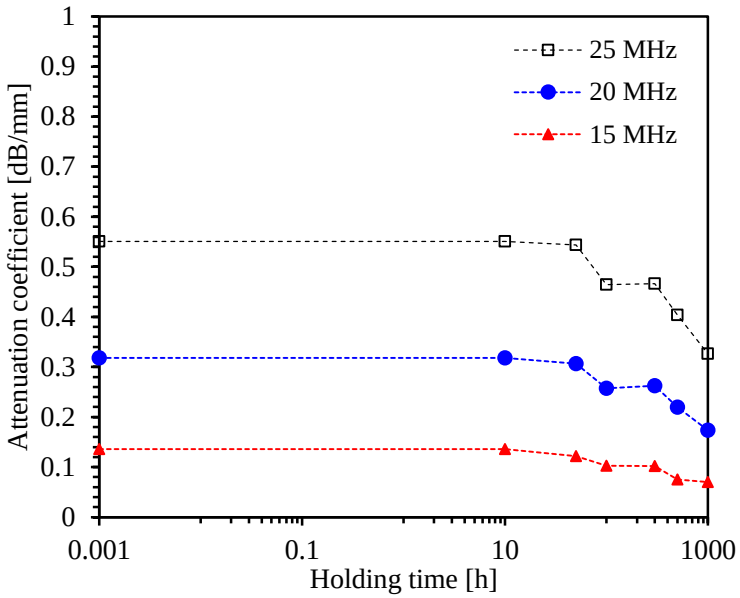

Figure 4.18. Longitudinal attenuation coefficient as function of aging time for 2507 SDSS aged at 475 °C.

While the trends are similar in these curves, the amount of changes increases with frequency. The dependency of the attenuation on frequency in Figure 4.18 presents a typical power-law in Rayleigh scattering regime, i.e. $\alpha \sim (a/\lambda)^p$, were a is the characteristic length, λ is the wavelength, and p is the exponent. This power-law behavior can be related to the phase transformation occurring in this material during thermal aging. However, it is unreasonable to interpret that the changes in attenuation are caused by the transformation of the ferrite phase since both $\alpha'$and G-phases are at nanometer scales, i.e. much smaller than the wavelength. Therefore, there should be other mechanisms that are responsible for the decreasing attenuation coefficient at longer holding times. The decrease in the attenuation coefficient must be caused by a microstructural change at a bigger scale.

Figure 4.19 shows optical images of the microstructures at magnification 1,000x in the rolling direction before and after 300 h of aging. It is observed that the ferrite grains are subdivided into new smaller grains as indicated in the image on the right side. This new grain boundary formation, as another consequence of the 475 °C embrittlement, effectively reduces the ferrite grain size (and grain volume) which will lead to the decreases in the grain scattering and the attenuation coefficient.

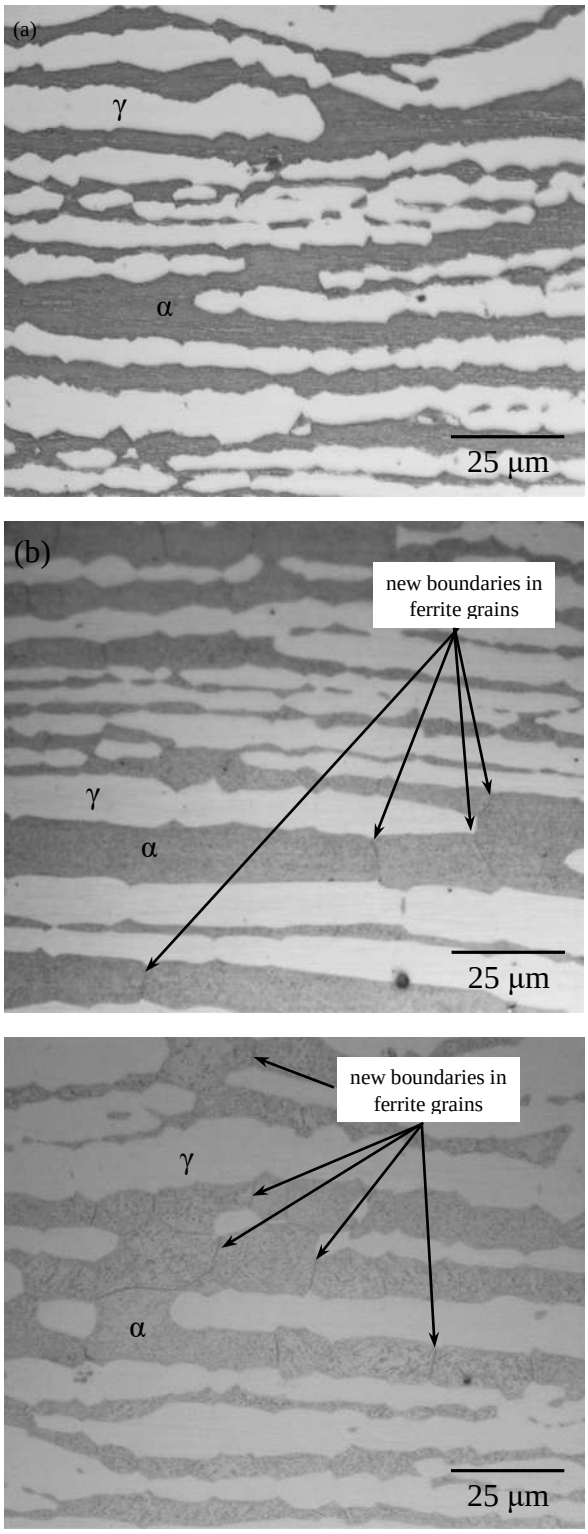

Figure 4.19. Optical micrographs at 1,000x of the 2507 SDSS microstructure in the rolling direction: (a) in the untreated condition and after aging for (b) 300 h and (b) 500 h.

This gradual transformation is better seen in the series of c-scan attenuation coefficient images as a function of holding time shown in Figure 4.20. The attenuation coefficients are measured using two immersion transducers of 6.35 mm diameter and central frequencies at 5 and 20 MHz respectively. From the c-scan images, it is clear that the attenuation coefficient obtained at 5 MHz does not show perceivable changes for all aging treatments as seen in Figure 4.20 (in the left column).

On the other hand, the images taken at 20 MHz show clearly the differences between the untreated (Figure 4.20(b)) and the specimen aged for 50 h (Figure 4.20(d)). Furthermore, the image for the untreated specimen shows regions of higher attenuation than in the specimen treated for 50 h; this change in the attenuation coefficient is related to the microstructural transformation endured by the 2507 SDSS. After 50 h treatment, there is a gradual reduction of the attenuation coefficient as holding time increases and from the images, the attenuation coefficient tends to become more homogeneous as the holding time increases, such that at 1,000 h holding time, the zones of higher attenuation have diminished in comparison to unaged and 50 h holding time samples.

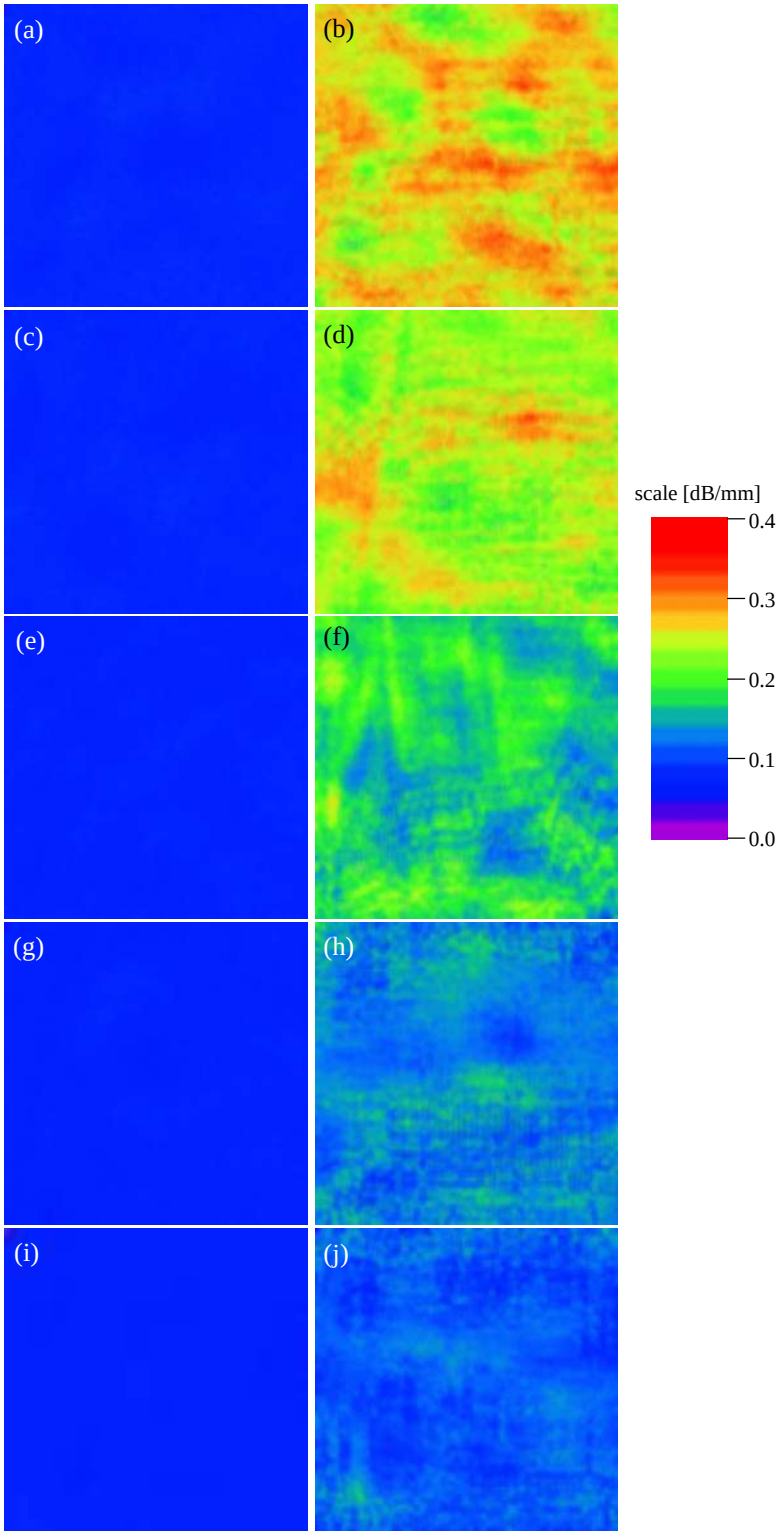

Figure 4.20. Attenuation coefficient c-scans images on 2507 SDSS obtained at 5 MHz (left) and 20 MHz (right) for: (a and b) untreated condition and specimens aged for: 50 h (c and d), 100 h (e and f), 500 h (g and h) and 1000 h (i and j).

4.7. Effect of embrittlement on hardness.

Figure 4.21(a) shows the Rockwell C hardness as a function of holding time, where the hardness gradually increases until 10 h and continues to increase, with a total change of approximately 50% at 300 h. A drawback of volumetric hardness tests is that the measured hardness is an averaged hardness over many grains of different phases, some of which might have been changed; the effects of the changes in each individual phase cannot be resolved. In the present case, the changes are due to the α′ precipitation, and it is unclear from the Rockwell C hardness whether the hardness changes are due to the 475 °C embrittlement (i.e. the α′ precipitation) or due to other effects in the other phase.

Figure 4.21(b) shows the results of five microhardness measurements obtained at five different grains of austenite and ferrite. The microhardness of both phases increase by 50 HV at 10 h. The microhardness of austenite phase then remains almost unchanged for the remaining holding times. However, the microhardness of the ferrite phase rapidly increases after 10 h of holding, and the microhardness shows a total change of 635 HV at 500 h. These results are a clear indication of the occurrence of the 475 °C embrittlement (i.e. the α′ precipitation).

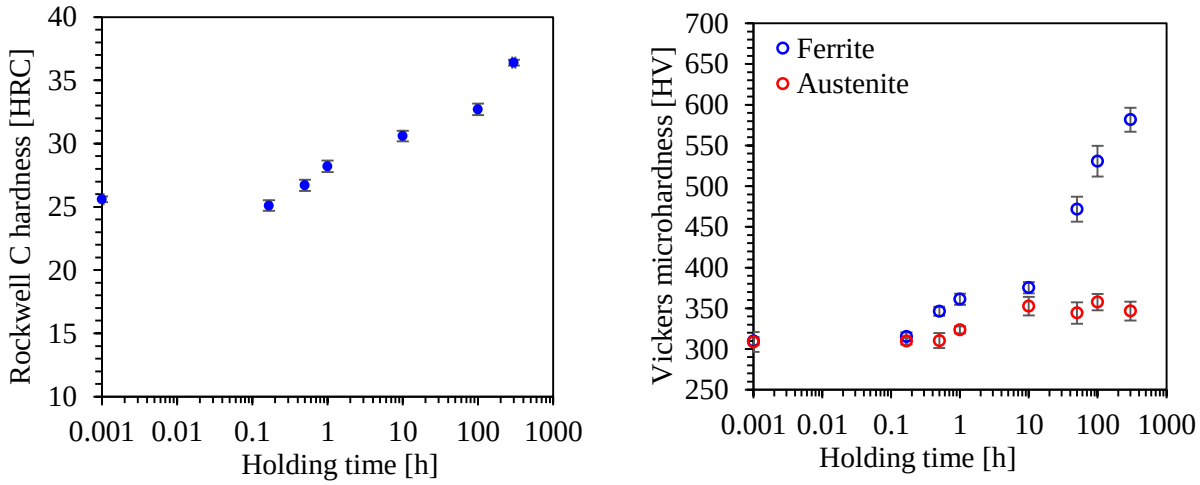

Figure 4.21. Hardness measurements as function of thermal exposure time. (a) Rockwell C hardness (b) Vickers microhardness.

4.8. Effect of aging time on nonlinear ultrasonic parameter.

The structural integrity of components that operate at elevated temperatures can be compromised by the precipitation of second phases during long-term service. In industry, the 475 °C embrittlement phenomenon due to spinodal decomposition of the ferrite phase that results in the formation of Cr-rich α′ precipitates at a relatively low temperature has been a concern because of its adverse effects on ferritic, duplex, and super duplex stainless steels; this precipitation causes a rapid decrease in the impact and corrosion resistance of these steels. Some of the precipitates have micro or nanometer dimensions, which makes them difficult to detect with conventional ultrasonic NDE methods. In contrast to the conventional linear ultrasonic NDE, nonlinear ultrasound offers a unique advantage of high sensitivity to microstructural changes such as those due to the precipitation of second phases, fatigue damage, plastic deformation, and thermal damage in metallic alloys. In this research, ultrasonic measurements were conducted to determine the nonlinearity parameter (β) of thermally embrittled 2507 SDSS specimens. The β parameters of these specimens were measured by exploiting two different nonlinear effects: the acoustoelastic effect and second harmonic generation in Rayleigh waves. Experimental results indicate that nonlinear parameters obtained from these independent experiments are consistent and sensitive to the 475 °C embrittlement process.

Figure 4.22 shows experimental results of the acoustoelastic measurements that show the changes in the relative velocities (of the two shear modes and the longitudinal mode) as functions of the applied stress after correcting for the Poisson effect. The acoustoelastic constant (K_1) in Eq. (2.7) was calculated from the linear regression (slope) of the data for each wave mode.

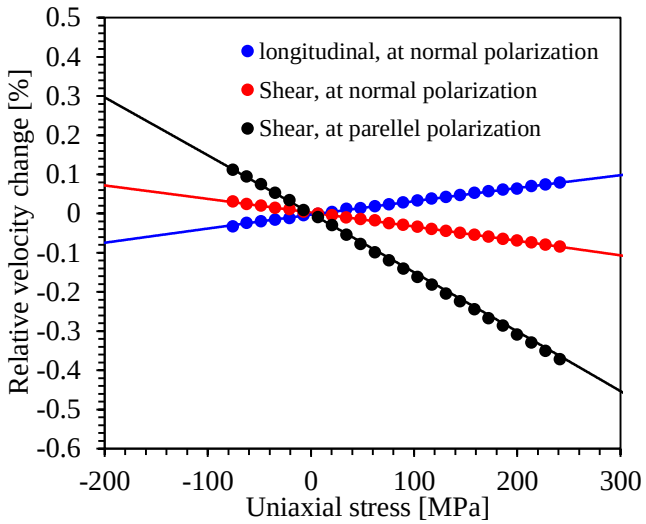

Figure 4.22. Relative shear wave and longitudinal wave velocity as a function of uniaxial stress.

Since the hardness measurements show that the embrittlement has occurred in the heat-treated SDSS specimens, changes in nonlinearity are very much likely due to this phenomenon. Figure 4.23(a) shows the normalized β_R as a function of holding time at 475 °C. The measured β_R shows a 30 % change at 10 h, drops further from the β_R for the untreated state, and then continues to decreases as holding time increases and as the specimen becomes embrittled.

Figure 4.23(b) shows the behavior of the nonlinear parameter βσ as a function of aging time. Interestingly, βσ shows small changes from untreated to 10 hours of exposure; this behavior is somewhat similar to the one exhibited by the microhardness of the ferrite phase, and the one exhibited by the nonlinear β_R obtained from Rayleigh wave measurements, where a small increase between untreated and 10 h occurs. Compared with the baseline nonlinearity (untreated specimen), βσ decreases rapidly at 50 h, and after 50 h, it slowly continues to decrease for the remaining aging times, changing from about 23.46 to 17.91 i.e., a difference of about 23.46% with respect to the specimen embrittled at 300 h.

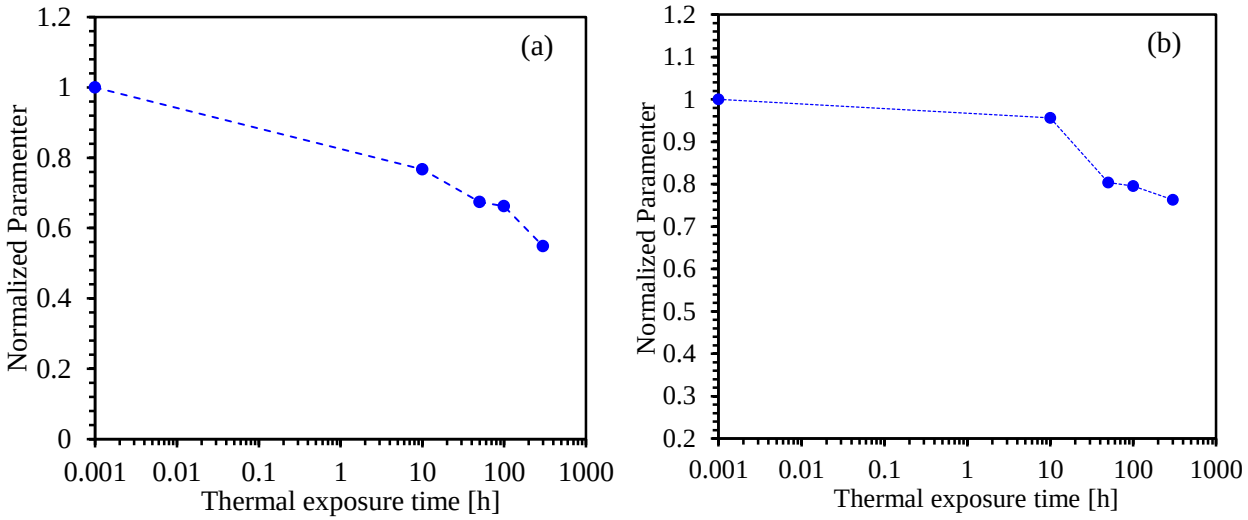

Figure 4.23. Normalized nonlinear parameters as function of thermal exposure time (a) from Rayleigh waves (β_R), (b) from acoustoelasticity (β_σ).

Figure 4.24 compares the changes of hardness, linear (average shear wave velocity) and nonlinear (β_R and β_σ) parameters. All parameters were normalized to their initial untreated values for comparison purposes. The shear wave velocity exhibits a 0.4 % change in velocity, while the nonlinear parameters obtained from nonlinear Rayleigh waves and acoustoelastic effect shows changes of about 45 % and 23.7 % respectively. These results indicate that nonlinear measurements are very consistent to each other and exceptionally appropriate for the detection of 475 °C embrittlement. The α´ precipitates are at the nanoscale, which can induce only small changes in the effective elastic properties, and thus in the shear wave velocity.

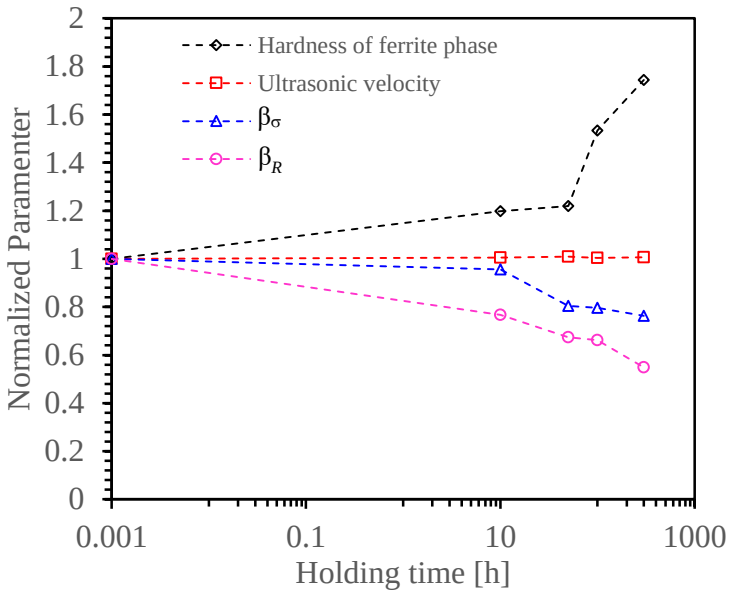

Figure 4.24. Changes of linear and nonlinear ultrasonic parameters and micro hardness as function of thermal exposure time.

4.9. Effect of aging time on thermoelectric power.

The data obtained in this study shows that the experimental setup employed is capable of accurately measuring the TEP associated with the gradual embrittlement of the SDSS. Figure 4.25 shows the TEP changes as a function of holding time. There are two distinctive regions for the changes in TEP; a region I, that shows an approximately linear increase of TEP from untreated condition until 50 h and a region II, where the TEP changes rapidly in the holding time range between 50 h and 500 h. The total change of the TEP from untreated to 500 h is approximately 140 % similar results have been reported by Kawaguchi and Yamanaka [123] for aged cast duplex stainless steel with different Cr concentrations. Therefore, since the Cr concentration of the alloy remains constant, the changes in the TEP are related to the phase separation phenomenon of ferrite ($\alpha \rightarrow \alpha + \alpha'$) that gradually occurs the changes undergone by the ferrite at a very small scale during the thermal exposure at 475 °C. Note that the elements Fe, Cr, and Ni, belong to the 3d-transition metals; the same authors [124] reported that the main effect on electrical conductivity of the transition metals comes from the scattering of the *s* electrons to the partially filled *d* band.

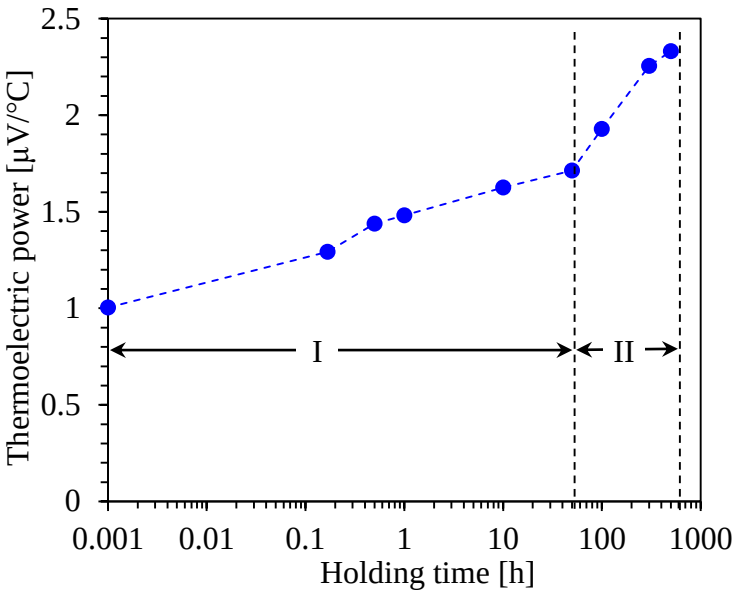

Figure 4.25. Change on the TEP of 2507 SDSS as function of holding time.

4.10. Effect of aging on tensile properties.

The results from tensile tests for 2507 SDSS specimens after aging at 475 °C for different holding times are shown in Figure 4.26. The results show that the ultimate tensile strength (UTS) does not change until 1 h holding time and gradually increases after 10 h to reach a saturation value of 1,121 MPa at 100 h. In a similar way, yield stress (YS) (measured at 0.4% offset) monotonically increases only after 1 h to a maximum value 908 MPa at 100 h and then remains unchanged at a value of 900 MPa. Figure 4.27 shows that as an effect of the embrittlement on the ductility. The percentage area reduction as a function of holding time does not change until 1 h holding time, monotonically decreases from 1 h to 50 h, and rapidly decreases after 100 h to a total change of 26.7% at 500 h holding time. A similar behavior for UTS and ductility in a 2205 DSS have been presented by Örnek et al. [125]. It is believed that the gradual spinodal decomposition and precipitation of other phases affect the dislocation movement enhancing YS and UTS, but on the contrary, decreasing the impact toughness of the SDSS.

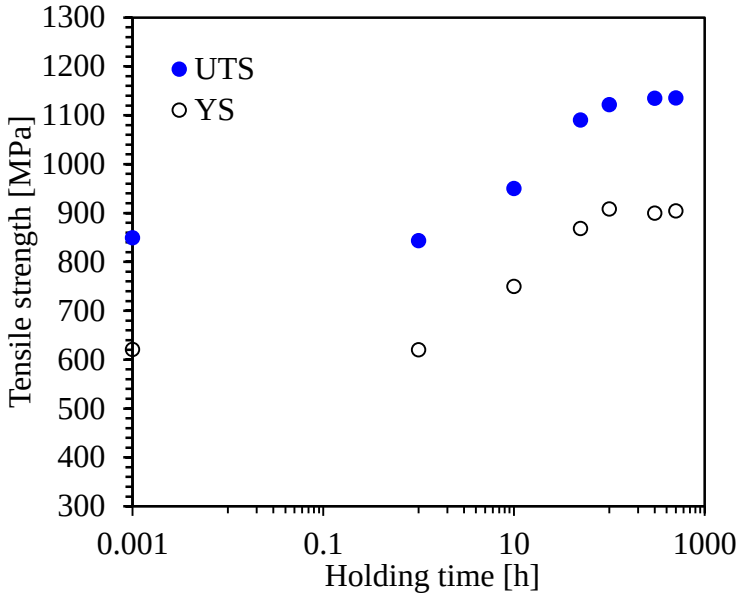

Figure 4.26. UTS and yield strength as function of holding time for aged 2507 SDSS.

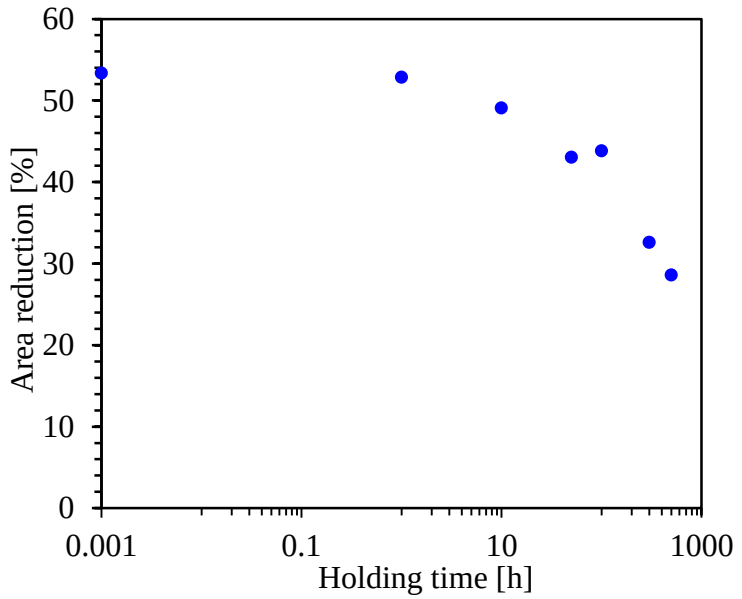

Figure 4.27. Percentage of area reduction as function of holding time for aged 2507 SDSS.

4.11. Use of the KJMA model to fit experimental results.

In order to better describe the α–α´phase transformation with aging time and its effect on the microhardness and UTS, the KJMA model in Eq. (3.11) was fitted to the measured Vickers microhardness data of the ferrite phase as well as the UTS data. The KJMA fitting result for hardness is shown in Figure 4.28, where the untreated sample exhibits the lowest value (H_0=309.7HV) in microhardness.

The KJMA parameters from fitting to experimental hardness and UTS are provided in Table 4.1.

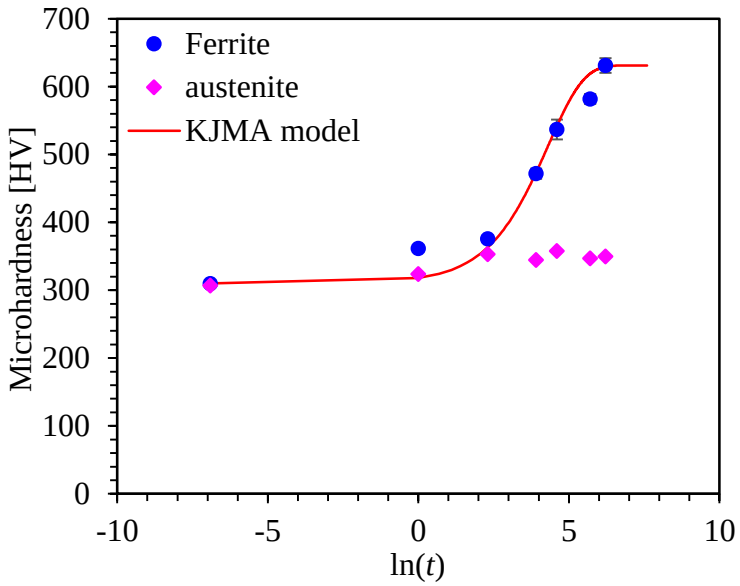

Figure 4.28. Microhardness predicted from KJMA model fitted to the mean value of measured microhardness for alloy 2507 SDSS.

The fitting parameter Q, k_0 and n for microhardness are in agreement to those found by Tucker et al. [110] for DSS. The KJMA fitting (The fitting parameters are listed in Table 4.1) for UTS is shown in Figure 4.29, which exhibits a transition behavior similar to the hardness but better complies with the saturation of properties.

Table 4.1. Fitting parameters from KJMA model for ultimate strength of aged samples at 748 K.

σ_u [MPa]	σ_0 [HV]	k_0	$k(T)$	Q [kJ-mol^{-1}]	R [Jmol^{-1}-K^{-1}]	n
1,135.5	849	18.8	0.0337	138	8.314	1.0

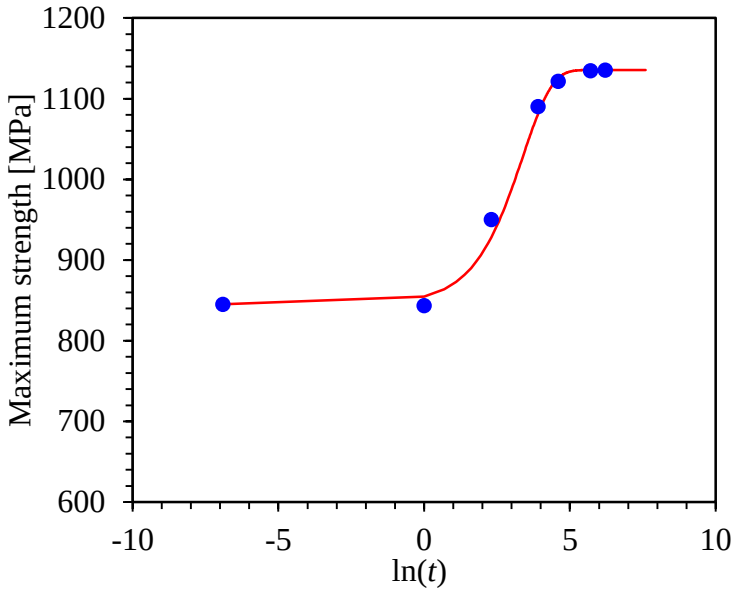

Figure 4.29. Ultimate strength predicted from KJMA model fitted to the mean value of measured ultimate strength for alloy 2507 SDSS.

4.12. Comparisons of NDE results.

Compared sensitivities of the different NDE methods that are used in this research.

All the NDE techniques that were used in this research to evaluate the 475° embrittlement of a 2507 super duplex stainless steel show a sensitivity do detect the embrittlement. It seems that the thermoelectric power shows the best sensitivity over the other techniques since it begins to detect changes at low aging times 62% change in the first 10 h holding time and shows an overall change of about 140% with respect to the untreated sample.

Linear ultrasonic velocity methods exhibit a poor sensitivity with small overall change of about 1.25% for shear wave velocity.

Attenuation methods exhibit better sensitivity at high frequencies the overall attenuation coefficient change is 0.147 dB/mm at 25MHz, the sensitivity decreases as frequency decreases, for example at 15 MHz, the overall attenuation coefficient change is 0.055 dB/mm about a 62 % drop and at 5 MHz, attenuation measurements can no detect apparent changes.

Nonlinear ultrasonic methods especially nonlinear parameter obtained by nonlinear Rayleigh waves shows a good sensitivity at low holding times 24% percent change in the first 10 h and show an overall change in the nonlinear parameter of about 46%.

Conductivity measurements was the less sensitive technique measuring a 2.26% change in the first 10 h; and an overall change of 5.3%.

CHAPTER V. CONCLUSIONS

5.1. Electric conductivity and corrosion susceptibility.

This work investigated the use of the electric conductivity measurement based on an ACPD probe with square-electrode configuration for monitoring 475 °C embrittlement of 2507 SDSS. It is shown that the electric conductivity determined from electric resistance measurements changes significantly and is well correlated with other measured data including the Q_r/Q_a ratio and ferrite phase microhardness. However, the absorbed energy from Charpy impact test indicates that the formation of α′ phase has a much more considerable effect on mechanical properties than on electric conductivity and corrosion resistance, especially during the first few hours.

Nonetheless, the measurement technique can be used for the detection and possibly for quantitative evaluation of the 475 °C embrittlement damage that is caused by thermally activated microstructural changes due to the precipitation of nanometric α′ precipitates. Consequently, the present research demonstrates the feasibility of using the ACPD probe for in-situ monitoring of 475 °C embrittlement in 2507 SDSS.

It is concluded that the ACPD probe technique can be used as a reliable method to determine the damage associated to the 475 °C embrittlement in SDSS AISI 2507 because the tendency of the electric conductivity measurements correlated well with the CPT and the Q_r/Q_a values. As the ageing time increased the Q_r/Q_a increased, the CPT decreased and the electric conductivity increased due to the microstructure changes produced by the 475 °C embrittlement.

5.2. Application of nonlinear ultrasonic measurements.

This work investigated the use of nonlinear ultrasound to monitor the 475 °C embrittlement of 2507 SDSS. The nonlinearity parameters measured by two independent nonlinear ultrasonic methods, namely nonlinear Rayleigh waves and acoustoelastic measurements, are compared to other parameters. It is shown that the nonlinear parameters change significantly and are well correlated with the microhardness changes of the ferrite phase.

Therefore, these measurement techniques can be used for the detection, and possibly for the quantitative evaluation of the 475 °C embrittlement damage that is caused by thermally activated microstructural changes due to the precipitation of nanometer-sized precipitates of α′. Even though nonlinear ultrasonic measurements are more complicated than linear ultrasonic measurements, they certainly have the advantage of larger changes with increasing 475 °C embrittlement effect.

5.3. Application of attenuation measurements.

The ultrasonic attenuation coefficient of longitudinal waves is used to investigate the microstructural changes in thermally embrittled 2507 SDSS specimens. Vickers microhardness measurements confirm that the 475 °C embrittlement phenomenon occurs primarily in the ferrite phase and after 50 h. Experimental results show that the attenuation coefficient decreases monotonically with the progress of embrittlement and the formation of new grain boundaries in the ferrite is the main cause of the changes in the longitudinal wave attenuation coefficient by reducing the grain scattering. This result indicates that the ultrasonic attenuation measurements can be useful to nondestructively detect/evaluate the microstructural transformation in these DSSs undergoing during the 475 °C embrittlement of 2507 SDSSs.

5.4. Application of thermoelectric power and KJMA model.

This work investigated the feasibility of using the thermoelectric power measurement for monitoring 475 °C embrittlement of 2507 SDSS. It is shown that the TEP is quite sensitive to the transformation $\alpha \rightarrow \alpha + \alpha'$ and it is well correlated with Vickers microhardness measurements, clearly distinguishing the ductile and brittle fracture modes. Tension tests indicates that the formation of α' phase has a considerable effect on UTS, YS and fracture behavior of the SDSS since the fracture surface exhibits two distinctive characteristics depending on the length of thermal exposure time, i.e. the formation of α' phase. The KJMA model predicts the effect of isothermal holding time on the microhardness and the KJMA parameters used to fit to experimental data are in agreement with those found in the literature. The TEP measurement technique can therefore be used for the detection and possibly for quantitative evaluation of the 475 °C embrittlement damage that is caused by thermally activated microstructural changes due to the precipitation of nanometric α′ precipitates. Consequently, the present research demonstrates the feasibility of using the TEP measurements for in-situ monitoring of 475 °C embrittlement.

5.5 Comments on NDE methods.

Discuss advantages and disadvantages of the NDE methods including the field applicability.

Thermoelectric power clearly is the most sensitive technique, its advantages are the demonstrated high sensitivity and its portability makes it a good candidate for field applications. Some disadvantages of this techniques are the need of a calibration process and the high amount of measurements needed to increase its accuracy and reproducibility.

Linear ultrasonic velocity methods although exhibit a poor sensitivity they are commonly used in the industry.

Attenuation methods could be used in field applications but they are limited by the surface condition of the sample and coupling problems.

Nonlinear ultrasonic methods especially nonlinear parameter also have a good sensibility, but equipment is expensive and its implementation for field application is limited.

Conductivity measurements though less sensitive have the advantage of low cost equipment and the possibility of continuous measurements can be implemented for field applications.

Recommendations and future work

In order to support the effect of ferrite grain splitting as the cause of the attenuation coefficient reduction it is suggested to investigate by means of EBSD that the grains resulting from such splitting show a different orientation.

References

1. Association, I.M., et al., *Practical Guidelines for the Fabrication of Duplex Stainless Steels*. 2009: BPR Publishers.
2. Reidrich, G.a.F.L., *Embrittlement of high chromium steels within temperature range of 570-1100°F. Archiv Für Das Eisenhüttenwesen.* 1941: p. p. 175-182.
3. Chandra, D.a.L.H.S., *Mössbauer effect study of the 475‡C decomposition of Fe-Cr.* Metallurgical Transactions, 1971. **2**: p. 511-519.
4. Grobner, P.J., *The 885° f (475° c) embrittlement of ferritic stainless steels.* Metallurgical Transactions, 1973. **4**(1): p. 251-260.
5. R.M. Fisher, E.J.D., K.G. Carrol, Transactions AIME, 1953. **197**: p. 690–695.
6. Williams, R.O., Trans. TMS-AIME, 1958. **212**: p. 497–502.
7. Cahn, J.W., *On spinodal decomposition.* Acta Metallurgica, 1961. **9**(9): p. 795-801.
8. Hilliard, J.E., *Spinodal decomposition*. Phase Transformations. 1970, Metals Park, Ohio: American Society for Metals.
9. Tucker, J.D., M.K. Miller, and G.A. Young, *Assessment of thermal embrittlement in duplex stainless steels 2003 and 2205 for nuclear power applications.* Acta Materialia, 2015. **87**: p. 15-24.
10. Cardarelli, F., *Materials handbook: A Concise Desktop Reference*. Springer. 2000. 95-112.
11. Cobb, H., *Steel Products Manual: Stainless Steels*. 1999: Iron & Steel Society.
12. McGuire, M.F., *Stainless Steels for Design Engineers*. 2008: ASM International.
13. *The Atlas Specialty Metals Technical Handbook of Stainless Steels*. 2008: Atlas Specialty Metals. 45.
14. Cobb, H.M. and A. International, *The History of Stainless Steel*. 2010: ASM International.
15. *Handbook of Stainless Steel*. 2013: Outokumpu Oyj. 92.
16. Nilsson, J.O., *Superduplex stainless steels.* Mater. Sci. Technol. 8, 1992. **8 (8)**: p. 685-700.
17. Sriram, R.A.T.D., *Pitting Corrosion of Duplex Stainless Steels.* Corrosion, 1989. **45(10)**: p. 804-810.
18. Okamoto, H., *Conf. Proc. Applications of Stainless Steel.* 1992. **Vol.1**: p. 360-369.
19. Lippold, J.C., Kotecki,D.J., *Welding Metallurgy and Weldability of Stainless Steels* 2005, New Jersey: John Wiley & Sons, Inc.
20. K. Hashimoto, K.A., K. Teramoto, Corrosion Science, 1979. **(19)**: p. 3-14.
21. R. W. Revie, H.H.U., *Corrosion and Corrosion Control: An Introduction to Corrosion Science and Engineering*. 2008, New Jersey: John Wiley & Sons, Inc.
22. Peckner, D., and Bernstein, I. M., *Handbook of Stainless Steels*. 1977, New York: McGraw-Hill.
23. Charles, J., *Conf Proc Duplex Stainless Steels.* France, Physical editions, 1991. **Vol. 1**: p. 3-48.
24. Copson, H.R., *Phisical Metallurgy of Stress-Corrosion Fracture,* . 1959, New York: Interscience. P. 126.
25. Floreen, S., and Hayden, H. W, *Transaction of the American Society for Metals.* 1968. **61**: p. 489-499.
26. H. Nagano, T.K., Y. Inaba, M. Harada, *Highly Corrosion Resistance Duplex Stainless.* Metaux Corrosion Industrie, 1981. **Vol. 667**: p. pp. 81-88.
27. Irvine, J.J., et al., Jornal of the Iron and Steel Institute, london, 1961. **199**: p. 153-169.
28. Y.C. Lu, R.B., CR, Clayton R.C Newman, *Electrochemical Society.* 1983: p. p.1774.

29. Gunn, R.N., ed., *Duplex Stainless Steels Microstructure, properties and applications*. 1997: Woodhead Publishing.
30. Garg, P.P.a.R., *Effect of Intermetallic Phases on Corrosion Behavior and Mechanical Properties of Duplex Stainless Steel and Super-Duplex Stainless Steel.* Advances in Science and Technology Research, 2015. **9(27)**: p. 87-105.
31. Charles, J., *Proc conf Duplex Stainless Steels '94, Glasgow, TWI.* 1994. **Vol. 1, paper KI**.
32. Nilsson, J.W.O.A., Huhtala T. , Karlsson L. , Jonsson P. , *Structural Stability of Super Duplex Stainless Weld Metals and Its Dependence on Tungsten and Copper.* Metallurgical and Materials Transactions A, 1996. **27A (8)**: p. 2196-2208.
33. Kubaschewski, O., *Iron: Binary Phase Diagrams*. 1982, New York: Springer-Verlag.
34. Bernhardsson, S., *Proceeding Conference: Duplex Stainless Steels, Beaune Bourgogne, France.* 1991.
35. Haugan, E.B., et al., *Effect of Tungsten on the Pitting and Crevice Corrosion Resistance of Type 25Cr Super Duplex Stainless Steels.* CORROSION, 2017. **73**(1): p. 53-67.
36. Schaeffler, A.L., *constitution diagram for stainless steel weld metal.* Metal progress, 1949. **56(11):680-680B**.
37. Vitek, J.M., and David, S. A., *The concept of an effective quench temperature and its use in studyng elevated temperature microstructures.* Metallurgical Transactions A, 1985. **16A(8)**: p. 1521-1523.
38. ASTM, *Standard Specification for Casting, Iron-Chromium-Nickel-Molybdenum Corrosion Resistant, Duplex (Austenitic/Ferritic) for Gemeral Application, ASTM A890/A890M-99*. 1999, West Conshohocke, PA: American Society for Testing and Materials.
39. R. Cervo, P.F., and A. Tiziani, *Annealing temperature effects on super duplex stainless steel UNS s32750 welded joints. I: Microstructure and partitioning of elements* Jornal of Materials Science, 2010. **45(16)**: p. 4369-4377.
40. Cozar R., L.J.M., Mayonobe B. and Morizot C., *Microstructure and property control in heavy section duplex and superduplex stainless steel forgings, In Duplex Stainless Steels.* 1994. **Vol. 94**: p. 13-16.
41. M., L., *Proceedings of the fourths international conference on duplex stainless steels.* Glasgow '94, 1994. **Vol. 2, paper XV**: p. 13-16.
42. R, L., ASM Trans Quart, 1967. **60**: p. 17.
43. Cahn, J.W., Trans A.I.M.E, 1968. **242**: p. 166-180.
44. Bentley, M.K.M.J., *APFIM and AEM investigation of CF8 and CF8M primary coolant pipe steels.* Materials Science and Technology, 1990. **6:3**: p. 285-292.
45. P. Auger, F.D., A. Menand, S. Bonnet, J. Bourgoin & M. Guttmann, *Atom probe and transmission electron microscopy study of aging of cast duplex stainless steels.* Materials Science and Technology, 1990. **6:3**: p. 301-313.
46. *ASTM A240/A240M-94a: Heat-resisting chromium and chromium-nickel stainless steel plate, sheet and strip for pressure vessels*. Vol. Ol.03. 1996: ASTM.
47. *NACE MR0175-97: Sulfide stress corrosion cracking resistant materials for oilfield equipment.* NACE International, 1997.
48. Sheffield, A., *Corrosion Handbook for Stainless Steels, Information 9401*. 1994.
49. Chandra, D. and L.H. Schwartz, *Mössbauer effect study of the 475‡C decomposition of Fe-Cr.* Metallurgical Transactions, 1971. **2**(2): p. 511-519.
50. Reidrich, G., Loib, F. , *Embrittlement of high chromium steels within temperature range of 570-1100°F.* Archiv Für Das Eisenhüttenwesen, 1941. **15**: p. 175-182.

51. Westraadt, J.E., et al., *A high-resolution analytical scanning transmission electron microscopy study of the early stages of spinodal decomposition in binary Fe–Cr.* Materials Characterization, 2015. **109**: p. 216-221.
52. Solomon, H.D. and L.M. Levinson, *Mössbauer effect study of '475°c embrittlement' of duplex and ferritic stainless steels.* Acta Metallurgica, 1978. **26**(3): p. 429-442.
53. Alleg, S., B. Bouzabata, and J.M. Greneche, *Kinetics study of the spinodal decomposition in the Fe–30.8Cr–12.2Co alloy by Mössbauer spectrometry.* Journal of Alloys and Compounds, 1999. **282**(1): p. 206-212.
54. Miller, M.K. and K.F. Russell, *Comparison of the rate of decomposition in Fe ·45%Cr, Fe ·45%Cr ·5%Ni and duplex stainless steels.* Applied Surface Science, 1996. **94–95**(0): p. 398-402.
55. Sahu, J.K., et al., *Effect of 475°C embrittlement on the mechanical properties of duplex stainless steel.* Materials Science and Engineering: A, 2009. **508**(1): p. 1-14.
56. Weng, K.L., H.R. Chen, and J.R. Yang, *The low-temperature aging embrittlement in a 2205 duplex stainless steel.* Materials Science and Engineering: A, 2004. **379**(1): p. 119-132.
57. Mateo, A., LLanes, L., Anglada, M. et al, *Characterization of the intermetallic G-phase in an AISI 329 duplex stainless steel.* Journal of Materials Science, 1997. **32**(17): p. 4533–4540.
58. Ruiz, A., et al., *Application of ultrasonic methods for early detection of thermal damage in 2205 duplex stainless steel.* NDT & E International, 2013. **54**: p. 19-26.
59. Toupin, R.A. and B. Bernstein, *Sound Waves in Deformed Perfectly Elastic Materials. Acoustoelastic Effect.* The Journal of the Acoustical Society of America, 1961. **33**(2): p. 216-225.
60. Nagy, P.B., *Fatigue damage assessment by nonlinear ultrasonic materials characterization.* Ultrasonics, 1998. **36**(1): p. 375-381.
61. Marino, D., et al., *Using nonlinear ultrasound to track microstructural changes due to thermal aging in modified 9%Cr ferritic martensitic steel.* NDT and E International, 2016. **79**: p. 46-52.
62. Cantrell, J.H. and W.T. Yost, *Nonlinear ultrasonic characterization of fatigue microstructures.* International Journal of fatigue, 2001. **23**: p. 487-490.
63. Wu, B., B.-s. Yan, and C.-f. He, *Nonlinear ultrasonic characterizing online fatigue damage and in situ microscopic observation.* Transactions of Nonferrous Metals Society of China, 2011. **21**(12): p. 2597-2604.
64. Doerr, C., et al., *Evaluation of sensitization in stainless steel 304 and 304L using nonlinear Rayleigh waves.* NDT & E International, 2017. **88**: p. 17-23.
65. Zeitvogel, D.T., et al., *Characterization of stress corrosion cracking in carbon steel using nonlinear Rayleigh surface waves.* NDT & E International, 2014. **62**: p. 144-152.
66. Valluri, J.S., K. Balasubramaniam, and R.V. Prakash, *Creep damage characterization using non-linear ultrasonic techniques.* Acta Materialia, 2010. **58**(6): p. 2079-2090.
67. Torello, D., et al., *Diffraction, attenuation, and source corrections for nonlinear Rayleigh wave ultrasonic measurements.* Ultrasonics, 2015. **56**: p. 417-426.
68. Nagy, P.B., P. McGowan, and L. Adler, *Acoustic Nonlinearities in Adhesive Joints*, in *Review of Progress in Quantitative Nondestructive Evaluation*, D.O. Thompson and D.E. Chimenti, Editors. 1990, Springer US: Boston, MA. p. 1685-1692.
69. Mohrbacher, H. and K. Salama, *The temperature dependence of elastic nonlinearity in metal-matrix composites.* Research in Nondestructive Evaluation, 1992. **4**(3): p. 139-150.

70. Lifshitz, E.M., A.M. Kosevich, and L.P. Pitaevskii, *CHAPTER III - ELASTIC WAVES*, in *Theory of Elasticity (Third Edition)*, E.M. Lifshitz, A.M. Kosevich, and L.P. Pitaevskii, Editors. 1986, Butterworth-Heinemann: Oxford. p. 87-107.
71. Murnaghan, F.D., *Finite Deformations of an Elastic Solid.* American Journal of Mathematics, 1937. **59**(2): p. 235-260.
72. Hughes, D.S. and J.L. Kelly, *Second-Order Elastic Deformation of Solids.* Physical Review, 1953. **92**(5): p. 1145-1149.
73. Lifshitz, L.D.L.a.E.M., *Theory of Elasticity*. Second ed. Vol. 7. 1959: Pergamon Press. 177.
74. Cantrell, J.H., *Fundamentals and applications of nonlinear ultrasonic nondestructive evaluation*, in *Ultrasonic nondestructive evaluation*. 2003, CRC Press. p. 377-448.
75. Rogers, P.H. and A.L.V. Buren, *An exact expression for the Lommel-diffraction correction integral.* The Journal of the Acoustical Society of America, 1974. **55**(4): p. 724-728.
76. Stanke, F.E. and G.S. Kino, *A unified theory for elastic wave propagation in polycrystalline materials.* The Journal of the Acoustical Society of America, 1984. **75**(3): p. 665-681.
77. Ahmed, S., R.B. Thompson, and P.D. Panetta, *Ultrasonic Attenuation as Influenced by Elongated Grains.* AIP Conference Proceedings, 2003. **657**(1): p. 109-116.
78. Ploix, M.-A., et al., *Measurement of ultrasonic scattering attenuation in austenitic stainless steel welds: Realistic input data for NDT numerical modeling.* Ultrasonics, 2014. **54**(7): p. 1729-1736.
79. Kube, C.M., *Attenuation of laser generated ultrasound in steel at high temperatures; comparison of theory and experimental measurements.* Ultrasonics, 2016. **70**: p. 238-240.
80. Javadi, Y. and M.A. Najafabadi, *Comparison between contact and immersion ultrasonic method to evaluate welding residual stresses of dissimilar joints.* Materials & Design, 2013. **47**: p. 473-482.
81. Saniie, J., T. Wang, and N.M. Bilgutay, *Statistical evaluation of backscattered ultrasonic grain signals.* The Journal of the Acoustical Society of America, 1988. **84**(1): p. 400-408.
82. Feuilly, N., et al., *RELATION BETWEEN ULTRASONIC BACKSCATTERING AND MICROSTRUCTURE FOR POLYCRYSTALLINE MATERIALS.* AIP Conference Proceedings, 2009. **1096**(1): p. 1216-1223.
83. Haldipur, P., et al., *Ultrasonic attenuation measurements in jet-engine nickel alloys.* AIP Conference Proceedings, 2001. **557**(1): p. 1338-1345.
84. Badidi Bouda, A., S. Lebaili, and A. Benchaala, *Grain size influence on ultrasonic velocities and attenuation.* NDT & E International, 2003. **36**(1): p. 1-5.
85. Seldis, T. and C. Pecorari, *Scattering-induced attenuation of an ultrasonic beam in austenitic steel.* The Journal of the Acoustical Society of America, 2000. **108**(2): p. 580-587.
86. Nagy, P.B. and L. Adler, *Scattering Induced Attenuation of Ultrasonic Backscattering*, in *Review of Progress in Quantitative Nondestructive Evaluation: Volume 7B*, D.O. Thompson and D.E. Chimenti, Editors. 1988, Springer US: Boston, MA. p. 1263-1271.
87. Ruiz, A., et al., *Microstructural and ultrasonic characterization of 2101 lean duplex stainless steel welded joint.* Applied Acoustics, 2017. **117**: p. 12-19.
88. Nicola, B., *Four-point potential drop measurements for materials characterization.* Measurement Science and Technology, 2011. **22**(1): p. 012001.
89. John, R.B., et al., *Alternating current potential-drop measurement of the depth of case hardening in steel rods.* Measurement Science and Technology, 2008. **19**(7): p. 075204.
90. Takeo, F., et al., *Arrangement of Probes for Measuring Case Depth by Means of Four-Point Probes*. Vol. 270-273. 2004. 82-88.

91. Lara, N.O., et al., *Nondestructive assessing of the aging effects in 2205 duplex stainless steel using thermoelectric power.* NDT & E International, 2011. **44**(5): p. 463-468.
92. Venkatsubramanian, T.V. and B.A. Unvala, *An AC potential drop system for monitoring crack length.* Journal of Physics E: Scientific Instruments, 1984. **17**(9): p. 765.
93. Michael, D.H., et al., *The measurement of surface cracks in metals by using a. c. electric fields.* Proceedings of the Royal Society of London. A. Mathematical and Physical Sciences, 1982. **381**(1780): p. 139-157.
94. Sposito, G., P. Cawley, and P.B. Nagy, *An approximate model for three-dimensional alternating current potential drop analyses using a commercial finite element code.* NDT & E International, 2010. **43**(2): p. 134-140.
95. Madhi, E. and P.B. Nagy, *Sensitivity analysis of a directional potential drop sensor for creep monitoring.* NDT & E International, 2011. **44**(8): p. 708-717.
96. Prajapati, S., P.B. Nagy, and P. Cawley, *Potential drop detection of creep damage in the vicinity of welds.* NDT & E International, 2012. **47**: p. 56-65.
97. Hwang, I.S., *A multi-frequency AC potential drop technique for the detection of small cracks.* Measurement Science and Technology, 1992. **3**(1): p. 62.
98. Lasseigne, A.N., et al., *Microstructural assessment of nitrogen-strengthened austenitic stainless-steel welds using thermoelectric power.* Metallurgical and Materials Transactions A, 2005. **36**(11): p. 3031-3039.
99. Carreon, Nagy, and Blodgett, *Thermoelectric Nondestructive Evaluation of Residual Stress in Shot-Peened Metals.* Research in Nondestructive Evaluation, 2002. **14**(2): p. 59-80.
100. Hu, J. and P.B. Nagy, *On the role of interface imperfections in thermoelectric nondestructive materials characterization.* Applied Physics Letters, 1998. **73**(4): p. 467-469.
101. Kleber, X., *Detection of surface and subsurface heterogeneities by the hot tip thermoelectric power method.* NDT & E International, 2008. **41**(5): p. 364-370.
102. Houzé, M., et al., *Study of molybdenum precipitation in steels using thermoelectric power measurement.* Scripta Materialia, 2004. **51**(12): p. 1171-1176.
103. Ruiz, A., et al., *Utilization of ultrasonic measurements for determining the variations in microstructure of thermally degraded 2205 duplex stainless steel.* Journal of Nondestructive Evaluation, 2009. **28**(3-4): p. 131.
104. Thiele, S., et al., *Air-coupled detection of nonlinear Rayleigh surface waves to assess material nonlinearity.* Ultrasonics, 2014. **54**(6): p. 1470-1475.
105. Örnek, C., et al., *Effect of "475 C embrittlement" on the corrosion behaviour of grade 2205 duplex stainless steel investigated using local probing techniques.*
106. Vol'nov, I.N., *The use of Kolmogorov's kinetic equation for the description of crystallization of alloys.* Metal Science and Heat Treatment, 2000. **42**(6): p. 207-210.
107. Kolmogorov, A.N., *On the statistical theory of the crystallization of metals.* Bull. Acad. Sci. USSR, Math. Ser, 1937. **1**: p. 355-359.
108. Avrami, M., *Kinetics of phase change. II transformation-time relations for random distribution of nuclei.* The Journal of Chemical Physics, 1940. **8**(2): p. 212-224.
109. Avrami, M., *Kinetics of phase change. I General theory.* The Journal of Chemical Physics, 1939. **7**(12): p. 1103-1112.
110. Tucker, J.D., M.K. Miller, and G.A. Young, *Assessment of thermal embrittlement in duplex stainless steels 2003 and 2205 for nuclear power applications.* Acta Materialia, 2015. **87**(Supplement C): p. 15-24.

111. William, J. and R. Mehl, *Reaction kinetics in processes of nucleation and growth.* Transactions of the Metallurgical Society of AIME, 1939. **135**: p. 416-442.
112. Iacoviello, F., F. Casari, and S. Gialanella, *Effect of "475 C embrittlement" on duplex stainless steels localized corrosion resistance.* Corrosion Science, 2005. **47**(4): p. 909-922.
113. Pinkas, M., et al., *Sensitivity of thermo-electric power measurements to α–α' phase separation in Cr-rich oxide dispersion strengthened steels.* Journal of Materials Science, 2015. **50**(13): p. 4629-4635.
114. Silva, R., et al., *Effect of thermal aging at 475°C on the properties of lean duplex stainless steel 2101.* Materials Characterization, 2016. **114**: p. 211-217.
115. Kawaguchi, S., et al., *Microstructural changes and fracture behavior of CF8M duplex stainless steels after long-term aging.* Nuclear Engineering and Design, 1997. **174**(3): p. 273-285.
116. Chandra, K., et al., *Low temperature embrittlement of duplex stainless steel: Correlation between mechanical and electrochemical behavior.* Materials Science and Engineering: A, 2010. **527**(16): p. 3904-3912.
117. Silva, R., et al., *Thermal aging at 475°C of newly developed lean duplex stainless steel 2404: Mechanical properties and corrosion behavior.* Corrosion Science, 2017. **116**: p. 66-73.
118. Lopez, N., et al., *Application of double loop electrochemical potentiodynamic reactivation test to austenitic and duplex stainless steels.* Materials Science and Engineering: A, 1997. **229**(1): p. 123-128.
119. Ebrahimi, N., et al., *Correlation between critical pitting temperature and degree of sensitisation on alloy 2205 duplex stainless steel.* Corrosion Science, 2011. **53**(2): p. 637-644.
120. de Assis, K.S., et al., *Assessment of electrochemical methods used on corrosion of superduplex stainless steel.* Corrosion Science, 2012. **59**: p. 71-80.
121. Silva, R., et al., *Thermal aging at 475 °C of newly developed lean duplex stainless steel 2404: Mechanical properties and corrosion behavior.* Corrosion Science, 2017. **116**: p. 66-73.
122. Pezzato, L., et al., *Effect of the Heat Treatment on the Corrosion Resistance of Duplex Stainless Steels.* Journal of Materials Engineering and Performance, 2018. **27**(8): p. 3859-3868.
123. Kawaguchi, Y. and S. Yamanaka, *Mechanism of the change in thermoelectric power of cast duplex stainless steel due to thermal aging.* Journal of Alloys and Compounds, 2002. **336**(1): p. 301-314.
124. Kawaguchi, Y. and S. Yamanaka, *Applications of Thermoelectric Power Measurement to Deterioration Diagnosis of Nuclear Material and Its Principle.* Journal of Nondestructive Evaluation, 2004. **23**(2): p. 65-76.
125. Örnek, C., et al., *Characterization of 475 C embrittlement of duplex stainless steel microstructure via scanning kelvin probe force microscopy and magnetic force microscopy.* Journal of The Electrochemical Society, 2017. **164**(6): p. C207-C217.